Intrinsic Point Defects in Zinc Oxide: Modeling of Structural, Electronic, Thermodynamic and Kinetic Properties

Vom Fachbereich

Material- und Geowissenschaften

der Technischen Universität Darmstadt

zur Erlangung des Grades Doktor-Ingenieur

genehmigte Dissertation

vorgelegt von

Paul Erhart

Referent: Prof. Karsten Albe

Korreferent: Prof. Heinz von Seggern

Tag der Einreichung: 18. Mai 2006

Tag der mündlichen Prüfung: 5. Juli 2006

Darmstadt, 2006

D17

Contents

List of Figures

List of Tables

List of Abbreviations

ABINIT	computer code for DFT calculations (Sec. A.3)
ABOP	analytic bond-order potential (Chapter 7)
bcc	body-centered cubic
BLYP	Becke, Lee, Yang, and Parr exchange-correlation functional (Sec. 3.2)
B3LYP	Becke 3-Parameter (Exchange), Lee, Yang, and Parr exchange-correlation functional (Sec. 3.2)
CBM	conduction band minimum
CI-NEB	climbing image nudged elastic band (Sec. 6.3.1)
DFT	density functional theory (Chapter 3)
dia	diamond
DOS	density of states
EAM	embedded atom method (Chapter 7)
EBE	extrinsic bond energy
fcc	face-centered cubic
f.u.	formula unit
GGA	generalized gradient approximation (Sec. 3.2)
GGA+U	GGA with semi-empirical self-interaction corrections (see Sec. 3.2 and Sec. 5.3.1)
GGSA	spin-polarized GGA
GULP	general utility lattice program (Sec. A.3)
hcp	hexagonal-close packed
HF	Hartree-Fock

IBE	intrinsic bond energy
KMC	kinetic Monte-Carlo
LAPW	linearized augmented-plane waves
LCAO	linear combination of atomic orbitals
LC	Lewis-Catlow shell-model potential
LDA	local density approximation (Sec. 3.2)
LDA+U	LDA with semi-empirical self-interaction corrections (see Sec. 3.2 and Sec. 5.3.1)
MC	Monte-Carlo
MD	molecular dynamics (Sec. A.1)
MEAM	modified embedded atom method (Chapter 7)
MEP	minimum energy path (Sec. 6.3.1)
MO	molecular orbitals
NEB	nudged-elastic band (Sec. 6.3.1)
O_i	oxygen interstitial
PAW	projector augmented wave(s)
PES	potential energy surface
PP	pseudopotential
PW91	Perdew-Wang parameterization of the GGA exchange-correlation functional (Sec. 3.2)
PWPP	plane wave-pseudopotential (Chapter 3)
PW	plane wave(s) (Chapter 3)
QM	quantum mechanical
sc	simple cubic
SIC	self-interaction corrections
SIRC	self-interaction and electronic relaxation corrections (Sec. 5.2)
TB	tight-binding
VASP	Vienna ab-initio simulation package (Sec. A.3)
VBM	valence band maximum
V_O	oxygen vacancy

V_{Zn}	zinc vacancy
XC	exchange-correlation (Sec. 3.2)
Zn_i	zinc interstitial

Abstract

The present dissertation deals with the modeling of zinc oxide on the atomic scale employing both quantum mechanical as well as atomistic methods.

The first part describes quantum mechanical calculations based on density functional theory of intrinsic point defects in ZnO. To begin with, the geometric and electronic structure of vacancies and oxygen interstitials is explored. In equilibrium oxygen interstitials are found to adopt dumbbell and split interstitial configurations in positive and negative charge states, respectively. Semi-empirical self-interaction corrections allow to improve the agreement between the experimental and the calculated band structure significantly; errors due to the limited size of the supercells can be corrected by employing finite-size scaling. The effect of both band structure corrections and finite-size scaling on defect formation enthalpies and transition levels is explored. Finally, transition paths and barriers for the migration of zinc as well as oxygen vacancies and interstitials are determined. The results allow to interpret diffusion experiments and provide a consistent basis for developing models for device simulation.

In the second part an interatomic potential for zinc oxide is derived. To this end, the Pontifix computer code is developed which allows to fit analytic bond-order potentials. The code is subsequently employed to obtain interatomic potentials for Zn–O, Zn–Zn, and O–O interactions. To demonstrate the applicability of the potentials, simulations on defect production by ion irradiation are carried out.

Part I.

Introduction

1. Motivation

Zinc oxide is a transparent semiconductor with a direct band gap of 3.4 eV. It can be degenerately doped n-type and free electron concentrations in excess of 10^{21} cm^{-3} are achievable [7]. It has long been believed that p-type doping of zinc oxide is impossible due to compensating intrinsic defects, in recent years p-type doping has, however, been reported by several groups (see Ref. [8] and references therein). The ambipolar dopability and the high exciton binding energy render ZnO an interesting material for transparent electronics and blue light emitting devices [9]. More recently, ZnO nanostructures such as rods, wires, belts, and rings have attracted a lot of attention since they open the way for developments of new devices [10, 11].

In order to improve the understanding of the physical and chemical properties of zinc oxide, computer simulations can be a valuable tool complementing and aiding the interpretation of experiments. Quantum-mechanical methods such as Hartree-Fock (HF) or density functional theory (DFT) have been extensively used to investigate e.g., surfaces [12, 13], high-pressure phase transitions [14, 15, 16], elastic properties [16], phonon dispersion [17], and point defects (see e.g., Refs. [18, 19, 20]). While such methods are highly transferable and allow for accurate and reliable calculations, they are severely limited in terms of length and time scales. On the other hand, by averaging out the electronic degrees of freedom and by considering interactions between individual atoms instead, analytic potentials achieve a superior computational efficiency and thereby create the possibility to study much more extended systems on time scales up to microseconds. In the present dissertation, both quantum mechanical methods and analytic potentials are employed.

Although a number of theoretical studies addressed the nature and the thermodynamics of intrinsic point defects in zinc oxide [18, 19, 20, 21, 22, 23], the understanding is still incomplete. In particular, the role of oxygen interstitials has been insufficiently analyzed.

For a Fermi level close to the valence band maximum the redox potential is sufficiently positive to allow the oxidation of oxygen. This can be achieved for example by placing O_2^{2-} ions on regular lattice sites equivalent to the formation of interstitial-like defects. In the first part of this dissertation density functional theory calculations are described which have been performed to investigate the existence and the properties of such defects. In addition, the ground state configurations of vacancies and oxygen interstitials are identified and characterized, both structurally and electronically. While previous studies have focused on oxygen interstitials in high-symmetry configurations, in the present work it is shown that dumbbell-like configurations have significantly lower formation enthalpies (Chapter 4).

DFT calculations rely on approximations for the exchange-correlation functional (see Sec. 3.2). Conventional choices such as the local density (LDA) [24] or generalized gradient approximations (GGA) [25] often provide an insufficient description of strongly localized electrons – such as the *d*-electrons in many transition metal compounds – and typically underestimate their binding energy [26]. In zinc oxide this leads to a significant overestimation of the covalency of the Zn–O bond and enhances the underestimation of the band gap intrinsic to DFT. Because of computational constraints DFT calculations are limited with respect to the system size. Periodic boundary conditions are used to remove surface effects but lead to interactions between periodic images, which are not always properly accounted for. Moreover, defect formation volumes, which describe the pressure dependence of the formation enthalpies, have not been calculated for zinc oxide so far.

As part of the present dissertation extensive DFT calculations address the aforementioned issues. In order to account for the band structure and the role of the Zn- 3*d* electrons, a semi-empirical correction scheme known as the LDA+U (or equivalently GGA+U) method [26] is employed. The errors due to the supercell size limitations are corrected by applying an extensive finite size scaling scheme and by explicitly taking into account the volume dependence of the formation enthalpies. Thereby, accurate values for the formation enthalpies and formation volumes are obtained which allows to deduce the equilibrium transition levels and their pressure dependence. The reliability of the data is assessed by comparison with GGA calculations and by extrapolation to the experimental band gap, which permits to interpret the results on a semi-quantitative basis (Chapter 5).

In order to optimize materials properties, it is typically necessary to process the material under non-equilibrium conditions. In such cases the behavior of the material is no longer exclusively governed by thermodynamics but kinetic effects become important. In semi-

conductors the (electronic) properties are largely determined by the (point) defects present in the material. Accordingly, point defect mobilities play an important role in optimizing and tuning the fabrication process. In zinc oxide, point defects mobilities furthermore pertain directly to the degradation behavior of varistor devices [27, 28, 29, 30] and are likely to contribute to the remarkable radiation hardness [31].

Unfortunately, in the past experimental measurements of self-diffusion in zinc oxide have not been able to provide a consistent set of data which renders it impossible to reliably interpret the results. In view of this situation a theoretical investigation is highly desirable in order to obtain an atomistic picture of the diffusion process and to be able to separate the contributions to the activation barrier. In Chapter 6 it is demonstrated how by combining quantum mechanical calculations with thermodynamic principles (Einstein relation) one can deduce point defect migration paths, identify mobile species, and derive diffusion coefficients. This approach is employed to study the migration of zinc and oxygen vacancies as well as interstitials. In combination with the formation enthalpies determined in Chapter 5 the dependence of the self-diffusivities on Fermi level and chemical potentials is derived which allows the (re-)interpretation of diffusion experiments (Chapter 6).

While DFT calculations are highly transferable and provide a wealth of detailed information, they are also computationally very expensive. In fact, many interesting problems in chemistry, condensed matter, and materials science occur on length and time scales which largely exceed the range of quantum mechanical calculations. On the other hand, analytic potentials deliver the computational efficiency required to deal with such problems (Chapter 7). They achieve this goal by sacrificing the details of the electronic structure and consider effective interactions between individual atoms instead. Obviously, some details are lost by such a coarse-graining procedure, however, a physically motivated and judiciously adapted model is nevertheless capable of describing materials behavior over a wide range of situations. One such model is the analytic bond-order potential (ABOP) scheme developed by Abell, Tersoff and others [32, 33]. In the second part of this dissertation, a computer code is developed which provides a generalized framework for fitting analytic bond-order potentials (Chapter 8). It is subsequently applied to derive parameter sets for Zn–O, Zn–Zn, and O–O interactions (Chapter 9). A representative application of the potential is the simulation of defect production in zinc oxide by ion irradiation.

2. Modeling of materials

This chapter provides a concise overview of techniques utilized in atomic scale modeling and discusses possibilities for bridging length and time scales by combining different approaches.

2.1. Simulation techniques in atomic scale modeling

A number of methods are available for studying materials on the atomic scale. Molecular static simulations are used to optimize structures in the zero temperature limit. They rely on numerical minimization algorithms such as conjugated gradients techniques. Molecular dynamics (MD) simulations allow to study the dynamics of a system at finite temperatures. This type of simulations is useful e.g., for studying ion-solid interactions or mechanical deformation mechanisms. Monte-Carlo (MC) methods, which represent a very efficient way to sample phase space, provide access to thermodynamic variables and equilibrium properties. If the transition paths and barriers are known, kinetic Monte-Carlo (KMC) techniques allow to study the dynamic evolution of a system on time scales of seconds, minutes or even hours (strongly system-dependent).

Any of these techniques requires a model which allows to calculate the total energy and/or the forces for arbitrary configurations. From the view point of quantum mechanics, the cohesion of a material arises from the interaction of the electrons in the field of the nuclei. This many-body problem is formally described by the Schrödinger equation

$$\hat{H}\Psi = \epsilon_i \Psi \tag{2.1}$$

where Ψ and ϵ_i denote the wave function and the eigenenergies, respectively. The Hamilton operator $\hat{H}$

$$\hat{H} = \hat{T}_e + \hat{T}_n + \hat{V}_{ee} + \underbrace{\hat{V}_{nn} + \hat{V}_{ne}}_{\hat{V}_{ext}} \tag{2.2}$$

comprises the contributions due to the kinetic energy of electrons ($\hat{T}_e$) and nuclei ($\hat{T}_n$) as well as terms arising from electron-electron ($\hat{V}_{ee}$), nucleus-nucleus ($\hat{V}_{nn}$), and electron-nucleus ($\hat{V}_{ne}$) interactions.

So-called *ab-initio* methods seek to find solutions for the many-body problem described by equations (2.1) and (2.2). In the field of theoretical chemistry, techniques such as second order Møller-Plesset perturbation theory, configuration interaction, or coupled cluster methods have been extensively used in the study of small molecules (see e.g., [34, 35]). An alternative approach known as quantum Monte-Carlo (QMC) and pioneered by Ceperley and Alder relies on Monte-Carlo methods to find solutions of the Schrödinger equation [36]; it has been applied for instance in the study of small silicon clusters [37, 38]. More recently, thanks to the continuous increase in computer power, it has even become feasible to employ quantum Monte-Carlo calculations to investigate the electronic structure and the energetics of defects in silicon [39] and carbon [40].

Unfortunately, pure *ab-initio* methods are severely restricted in terms of length and time scales. In order to circumvent these limitations a large variety of methods has been developed which represent different ways to simplify the original many-particle problem and which cover different levels of accuracy and efficiency. At the lower end of this scale, with a minimal number of simplifications, Hartree-Fock (HF) and density functional theory (DFT) methods [41] are well established and widely used, because they provide a very favorable compromise between reliability and accuracy on one hand, and computational efficiency on the other. Still, system sizes are restricted to at most a few thousand (valence) electrons and the maximum time scale in dynamical simulations does not exceed a few picoseconds. Tight-binding (TB) methods [42] are based on the linear combination of atomic orbitals (LCAO) theory. By successively including or neglecting higher order moments of the electron density the accuracy and the efficiency of the method can be weighted against each other. While TB techniques extend the length and time scales for simulations in comparison with HF or DFT, they are still not efficient enough to address many of the most challenging problems in materials science, chemistry, and condensed matter physics

which often involve thousands or millions of atoms and time scales in the regime of nano or microseconds. In order to treat such problems in a computationally efficient manner, while maintaining atomic resolution, analytic potential models that deliver realistic energies and interatomic forces are an indispensable tool for bridging the gap between quantum mechanical methods and mesoscopic continuum models. Instead of treating the electronic structure explicitly, these models consider cohesion between atoms or ions. The application and analysis of one particular type of these potential schemes is part of the present work. A detailed discussion of this subject will be given in chapters 8 and 9.

At the next level of approximation the atomic structure is mapped onto a lattice and the interactions are described e.g., by means of Ising-like models or cluster expansion methods which rely on effective parameters. Macroscopic length and time scales are accessible via continuum methods which owe their efficiency essentially to a neglect of the atomic structure of the material.

2.2. Bridging length and time scales

As described in the previous section, there exists a trade-off between accuracy and transferability on one side and computational efficiency on the other. Therefore, a given technique can rarely be used alone but must be combined and linked with other methods in order to obtain a reliable as well as efficient description of the system under consideration. In the past, a number of schemes have been developed to achieve this goal: For instance, Jacobson and coworkers [43] as well as Voter and coworkers [44, 45] coupled MD with KMC simulations to extend the timescale. The quasicontinuum method pioneered by Tadmor, Ortiz, and Philips [46, 47, 48] introduces a systematic coarse graining between the atomic and the continuum scale. Csanyi *et al.* devised a "learn-on-the-fly" MD algorithm in order to optimize the transferability and accuracy of the force field [49] by combining analytic potentials with first-principles methods.

In some cases it is possible to link quantities which are derived on the atomic scale directly with macroscopic observables. In the present work diffusion constants (D, macroscopically accessible) are derived based on the knowledge of the migration barriers (ΔG_i^m) and the

attempt frequencies ($\Gamma_{0,i}$, defined on the atomic scale) using the relations (see Chapter 6 for details)

$$\Gamma_i = \Gamma_{0,i} \exp\left[-\Delta G_i^m / k_B T\right] \tag{2.3}$$

and

$$D = \frac{1}{2} \sum_i \zeta_i \Gamma_i^d |\boldsymbol{\lambda}_i|^2. \tag{2.4}$$

The migration barriers can be obtained by refined molecular static techniques (see Sec. 6.3.1) and the attempt frequencies are related to the vibrational (elastic) properties of the system.

Part II.

Quantum mechanical modeling of intrinsic point defects

3. Density functional theory

In this chapter the fundamental concepts and equations of density functional theory are reviewed. The most important exchange-correlation functionals are briefly introduced. Finally, the implementation of density functional theory in the plane wave-pseudopotential approach is outlined.

3.1. General aspects

Density functional theory (DFT) has proven to be a very powerful tool for studying electronic and structural materials properties. Basically, the method requires the coordinates and atom types as input parameters. Compared to pure *ab-initio* methods DFT is significantly more efficient because it maps the many-body problem described in Sec. 2.1 onto a set of effective one-particle equations. As the downside of this procedure an *a-priori* unknown exchange-correlation functional appears in the equations.

DFT relies on two theorems: Firstly, the total energy can be expressed as a functional of the electron density and secondly, the electron density which minimizes the energy is the ground state electron density of the system (variational principle) [50]. The Hamilton operator for the electronic system in a solid is given by equation (2.2). Defining the functional

$$F[n] = \min_{\Psi \to n} \left\langle \Psi | \hat{T}_e + \hat{V}_{ee} | \Psi \right\rangle \tag{3.1}$$

of the electron density

$$n = \int \mathrm{d}\boldsymbol{r} \Psi^* \Psi \tag{3.2}$$

with the minimum taken over all wave functions Ψ, the basic theorems are expressed as

$$E[n] = \int \mathrm{d}\boldsymbol{r} \hat{V}_{ext}(\boldsymbol{r}) n(\boldsymbol{r}) + F[n] \geq E_0 \tag{3.3}$$

and

$$\int \mathrm{d}\boldsymbol{r}\hat{V}_{ext}(\boldsymbol{r})n_0(\boldsymbol{r}) + F[n_0] = E_0 \tag{3.4}$$

where the index 0 denotes the ground state. Furthermore it can be shown [51] that the electron density which satisfies these equations is obtained by solving the one-particle Schrödinger equations

$$\left[\hat{T}_e + \hat{V}_{ext} + \int \mathrm{d}\boldsymbol{r'}\frac{n(\boldsymbol{r'})}{|\boldsymbol{r}-\boldsymbol{r'}|} + \hat{V}_{xc}\right]\psi_i = \epsilon_i\psi_i. \tag{3.5}$$

Here, $\hat{V}_{xc}$ denotes the exchange-correlation functional and the total electron density is

$$n = \sum_i^N |\psi_i|^2 \tag{3.6}$$

where N is the number of electrons.

3.2. Exchange-correlation functional

For the exchange-correlation (XC) functional ($\hat{V}_{xc}$ in equation (3.5)) different approximations have been established in the past. The most simple one is the local density approximation (LDA), in which the XC energy for the charge density $n(\boldsymbol{r})$ at point $\boldsymbol{r}$ is taken as the XC energy of a uniform electron gas of the same density [24]. The LDA typically overestimates the strengths of chemical bonds yielding too large cohesive energies and too small bond lengths. The generalized gradient approximation (GGA) considers the XC energy as a function of both the charge density and its gradient. Compared to the LDA, it tends to soften bonds often* leading to a better description of bond energies and lengths. Hybrid-functionals such as B3LYP [52, 53] combine the exact exchange functional from Hartree-Fock theory with the exchange part of a DFT XC-functional. They provide an improved description of several properties but due to their functional form are incompatible with periodic boundary conditions.

An alternative approach originating from the study of transition metal oxides such as NiO was pioneered by Anisimov and coworkers [26, 54, 55, 56]. The so-called LDA+U

*While the GGA is often considered superior to the LDA, there are cases in which the LDA performs better e.g., ferroelectric titanates.

or GGA+U method introduces semi-empirical corrections to account for the artificial self-interaction intrinsic to the unmodified LDA and GGA functionals. A GGA+U scheme is employed in Chapter 5 where a more detailed description of this method is given (Sec. 5.3.1).

3.3. Plane wave basis sets and pseudopotentials

Owing to the periodicity of crystals, DFT calculations of the solid state can be greatly simplified by using periodic boundary conditions and plane wave basis sets [57]. Bloch's theorem [58] states

$$\psi_{n,\boldsymbol{k}} = u_n \exp(i\boldsymbol{k} \cdot \boldsymbol{r}) \tag{3.7}$$

where u_n are functions with the same periodicity as the supercell and $\boldsymbol{k}$ is a vector within the Brillouin zone. Thus, the total wave function is given by

$$\psi_n = \sum_{\boldsymbol{k}} \psi_{n,\boldsymbol{k}}. \tag{3.8}$$

Expanding equation (3.7) into a plane wave basis set and combining it with equation (3.8) yields

$$\psi_{n,\boldsymbol{k}} = \sum_{\boldsymbol{G}} c_{n,\boldsymbol{k}+\boldsymbol{G}} \exp\left[i(\boldsymbol{k}+\boldsymbol{G}) \cdot \boldsymbol{r}\right] \tag{3.9}$$

where $\boldsymbol{G}$ are vectors proportional to the inverse lattice vectors of the supercell and $c_{n,\boldsymbol{k}+\boldsymbol{G}}$ are the expansion coefficients. In these equations two important parameters have been implicitly introduced, which control the numerical convergence of a DFT calculation when a plane wave basis set is being used. In principle, the sum over $\boldsymbol{G}$ extends to infinity; in actual implementations of the method it needs, however, to be cut off at some vector $\boldsymbol{G}_{cut}$, which is typically expressed in terms of the plane wave cutoff energy $E_{cut} = \hbar^2 \boldsymbol{G}_{cut}^2 / 2m_e$ (m_e denotes the electron mass). Secondly, the sum over $\boldsymbol{k}$ should extend over the entire Brillouin zone, while in practice it is replaced by a sum over special k-points [59]. The first step in any DFT calculation is, therefore, to determine a cutoff energy and a k-point mesh which provide numerically well-converged results.

The core electrons usually do not significantly contribute to the bonding. Furthermore, in order to guarantee orthogonality of states with the same orbital momentum (e.g., 1s and

$2s$, $2p$ and $3p$) very large plane wave basis sets are required. For the sake of computational efficiency it is, therefore, desirable to replace the core electrons by a pseudopotential (PP). In this work norm-conserving [60] and ultrasoft [61] PPs were employed as well as the projector augmented wave (PAW) method [62].

All DFT codes used in the present work (see Sec. A.3 for an overview) are implementations of the plane wave-pseudopotential (PWPP) approach.

4. Structure and stability of vacancies and oxygen interstitials*

In the present chapter a comparative study of the structure and stability of oxygen defects in ZnO is presented. By means of first-principles calculations based on local density functional theory vacancies as well as different interstitial configurations of oxygen in various charge states have been investigated. The results reveal that dumbbell-like structures are thermodynamically the most stable interstitial configurations for neutral and positive charge states due to the formation of a strong covalent oxygen–oxygen bond. For negative charge states the system prefers a split-interstitial configuration with two oxygen atoms in almost symmetric positions with respect to the associated perfect lattice site. The calculated defect formation energies imply that interstitial oxygen atoms may provide both donor- and acceptor-like defects.

4.1. Introduction

Zinc oxide can be degenerately doped n-type and free electron concentrations in excess of $10^{21}\,\mathrm{cm}^{-3}$ are achievable [7]. In recent years p-type doping has been reported by several groups (see Ref. [8] and references therein). As a result of self-compensation, however, for large band gap materials very often only a single conductivity type can be obtained (see e.g. Refs. [63, 64]). In that case raising the dopant level will not lead to the generation of free carriers but to the generation of compensating defects.

In order to achieve p-type conductivity the Fermi level needs to be close to the valence band. Photoelectron spectroscopy reveals that the valence band in ZnO lies about 7 eV

*Parts of the present chapter have been published in Ref. [6].

below the vacuum level [65]. If a value of 4.5 eV is taken as reference for the standard hydrogen electrode on an absolute energy scale [66], a Fermi level close to the valence band maximum of ZnO corresponds to a redox potential of $\gtrsim 2.5$ eV. Chemically, such large redox potentials can cause the oxidation of oxygen and thus change the formal oxidation state from O^{-II} to O^{-I} or even further to O^0. The oxidation of oxygen in ZnO can be written in Kröger-Vink notation as

$$O_O^\times + \frac{1}{2}O_2 \rightarrow (O_2)_O^\times$$

suggesting that O_2^{2-} ions occupy O^{2-} lattice sites as in zinc peroxide (ZnO_2). The existence of such interstitial structures has not been discussed in literature, although Lee *et al.*[21] investigated a dumbbell-configuration in the context of N acceptors in ZnO. Other theoretical studies [18, 19, 20, 67] on intrinsic point defects in ZnO only considered interstitial oxygen as a potential acceptor and assumed highly symmetric octahedral and tetrahedral sites.

Therefore, a comprehensive study of peroxo-like interstitials in comparison to high-symmetry configurations and vacancies in charge states between 2+ and 2− has been carried out. The results reveal that interstitial oxygen atoms are most stable in dumbbell and split-interstitial configurations and may act both as donor- and acceptor-like defects.

4.2. Methodology

4.2.1. Computational method

Density functional theory (DFT) calculations within the local-density approximation (LDA) in the Teter-Pade parameterization [68] were performed using the plane wave-pseudopotential code ABINIT [69, 70]. Norm-conserving pseudopotentials due to Troullier and Martins [60] were used, which included the $3d$-electrons of zinc as part of the valence. The plane wave basis set cutoff energy was set to 35 Hartree to achieve convergence of total energies better than 0.05 eV. Orthogonal supercells containing 64 atoms were employed and the Brillouin zone of the supercell was sampled using 16 k-points distributed on a shifted Monkhorst-Pack grid [59]. All calculations are performed at the same supercell size. This neglect of volume relaxation constitutes the leading contribution to the intrinsic error in the calculated formation enthalpies which can be estimated to be less than 0.1 eV.

The crystallographic parameters for ideal wurtzite zinc oxide were determined as $a = 3.200\,\text{Å}$ and $c/a = 1.613$ with an internal relaxation of $u = 0.379$. Within the known restrictions of the LDA these numbers compare well with the experimental values[†] of $a = 3.242\,\text{Å}$, $c/a = 1.600$ and $u = 0.382$. The formation enthalpy of wurtzite zinc oxide was computed as $-4.15\,\text{eV/f.u.}$ in reasonable agreement with previous calculations and the experimental value of $-3.56\,\text{eV/f.u.}$. The band gap at the Γ-point is 0.81 eV, which is considerably below the experimental value of 3.4 eV, but consistent with previous DFT calculations. (If only the special k-points used in the supercell calculations are considered, which do not include the Γ-point, the band gap is 1.31 eV). The discrepancy is due to the well known band gap error of density functional theory. The consequences of this shortcoming will be addressed in section Sec. 4.3.1 and in Chapter 5.

Furthermore the ground state structures of pure oxygen and zinc have been analyzed, since their cohesive energies enter the calculation of the formation enthalpy of zinc oxide as well as the defect formation enthalpies (see equation (4.8) below). In case of zinc the calculated cohesive energy of $-1.801\,\text{eV/atom}$ shows the expected overbinding (compare Sec. 3.2) if compared to the experimental value of $-1.359\,\text{eV/atom}$, while the lattice constants $a = 2.582\,\text{Å}$ ($2.660\,\text{Å}$) and $c = 4.791\,\text{Å}$ ($4.863\,\text{Å}$) agree nicely with the experimental numbers (given in brackets). The oxygen dimer has a calculated bond length of $1.241\,\text{Å}$ ($1.208\,\text{Å}$) and a dimer energy of 5.85 eV (5.17 eV).

4.2.2. Formation enthalpies

Qian *et al.* derived the dependence of surface energies on the chemical environment [76]. This approach has been later generalized to the case of point defects by Zhang and Northrup [77]. In the following, the formalism is described and the equations for the case of a stoichiometric binary compound are introduced.

In thermodynamic equilibrium under conditions of constant temperature and pressure the state of a system is determined by the Gibbs free energy

$$G = E + TS - pV = H + TS \tag{4.1}$$

where E and H denote the internal energy and the enthalpy, T and S are the temperature and the entropy, and p and V represent pressure and volume. In order to derive formation

[†]The experimental data cited in this section was obtained from Refs. [71, 72, 73, 74, 75].

entropies of point defects very large supercells (on the order of a few hundred atoms) are needed, because the entropy converges slowly with supercell size [78]. Since, for the supercells accessible within the present computational framework, the reliability of calculated entropies would be limited, entropic contributions were neglected. Since the temperature dependent terms tend to cancel for differences between the free enthalpies of condensed phases, this is a valid approximation. In the present chapter the pressure-volume is, furthermore, assumed to be zero which is an excellent approximation for moderate pressures while for the calculation of formation volumes in Chapter 5 this contribution is explicitly included.

The chemical potential is defined as the derivative of G with respect to the number of particles of type i

$$\mu_i = \frac{\partial G}{\partial n_i} \tag{4.2}$$

and in equilibrium is the same for all phases which are in contact. The chemical potentials are subject to certain constraints [‡]: Firstly, μ_i cannot be more negative than the chemical potential of the most stable elemental (reference) phase, μ_i^{bulk} (e.g., hcp-Zn or dimeric oxygen), $\mu_i \geq \mu_i^{\text{bulk}}$. The limit $\mu_i = \mu_i^{\text{bulk}}$ corresponds to the case when the system under consideration is in immediate contact with the reference phase. Secondly, the chemical potentials of the constituents are limited by the formation of mixed phases which in the case of a binary compound $\mathrm{A}_a\mathrm{B}_b$ leads to the constraint

$$a\mu_{\mathrm{A}} + b\mu_{\mathrm{B}} = \mu_{\mathrm{A}_a\mathrm{B}_b}^{\text{bulk}} = a\mu_{\mathrm{A}}^{\text{bulk}} + b\mu_{\mathrm{B}}^{\text{bulk}} + \Delta H^f \tag{4.3}$$

where the equation introduces the formation enthalpy ΔH^f. The constraints can be conveniently summarized as

$$\mu_i^{\text{bulk}} + \Delta H^f \geq \mu_i \geq \mu_i^{\text{bulk}}. \tag{4.4}$$

The equilibrium state of a neutral system is determined by the minimum of the following function

$$G_{def}(n_i) - \sum_i n_i\mu_i \approx H_{def}(n_i) - \sum_i n_i\mu_i \tag{4.5}$$

where G_{def} and H_{def} refer to the system containing the defect. For charged defects one must furthermore include the electro-chemical potential of the electrons, $\mu_e = E_{\text{VBM}} + E_F$.

[‡]In the present work, cohesive energies are always negative. This is in contrast to Ref. [76].

It represents the energy required to transfer an electron from the Fermi level, E_F, to the vacuum, where E_F is measured from the valence band maximum, E_{VBM}. In summary, the formation enthalpy of a defect in charge state q is given by

$$\Delta H_D = H_{def} - \sum_i n_i \mu_i - q(E_{\mathrm{VBM}} + E_F) \tag{4.6}$$

For a stoichiometric binary system by defining [77]

$$\Delta\mu = (\mu_{\mathrm{Zn}} - \mu_{\mathrm{O}}) - (\mu_{\mathrm{Zn}}^{\mathrm{bulk}} - \mu_{\mathrm{O}}^{\mathrm{bulk}}) \tag{4.7}$$

equation (4.6) can be rewritten as

$$\begin{aligned} \Delta H_D = H_{def} &- \frac{1}{2}(n_{\mathrm{Zn}} + n_{\mathrm{O}})\mu_{\mathrm{ZnO}}^{\mathrm{bulk}} \\ &- \frac{1}{2}(n_{\mathrm{Zn}} - n_{\mathrm{O}})(\mu_{\mathrm{Zn}}^{\mathrm{bulk}} - \mu_{\mathrm{O}}^{\mathrm{bulk}}) \\ &- q(E_{\mathrm{VBM}} + \mu_e) - \frac{1}{2}(n_{\mathrm{Zn}} - n_{\mathrm{O}})\Delta\mu. \end{aligned} \tag{4.8}$$

The last but one term describes the variation of the formation enthalpy of charged defects with the Fermi level which is limited by $0 \leq E_F \leq E_G$, where E_G is the (calculated) band gap. The last term describes the variation with the chemical potentials which according to equations (4.3) and (4.7) is constrained by the formation enthalpy of wurtzite zinc oxide [20] $\Delta\mu \leq |\Delta H^f|$; zinc- and oxygen-rich conditions correspond to $\Delta\mu = -\Delta H^f$ and $\Delta\mu = \Delta H^f$, respectively. In the zero temperature limit the reference chemical potentials equal the cohesive energies of molecular oxygen, hcp-zinc, and wurtzite zinc oxide. For the following computations the calculated values from Sec. 4.2.1 were used. It should be noted, however, that the findings are essentially not affected by this particular choice.

4.2.3. Configurations

In order to identify the most stable structure for the oxygen interstitial defect, a number of initial configurations have been generated. The atomic positions were relaxed using conjugated gradients minimization until the maximum residual force was less than 4 pN (2.5 meV/Å). For the oxygen interstitials ($\mathrm{O_i}$) charge states between 2− and 2+ were considered. Three distinct configurations corresponding to local minima on the total-energy surface were identified (see Fig. 4.2). In the following the octahedral interstitial ($\mathrm{O_{i,oct}}$), the dumbbell configuration ($\mathrm{O_{i,db}}$) and the rotated dumbbell configuration ($\mathrm{O_{i,rot-db}}$) will

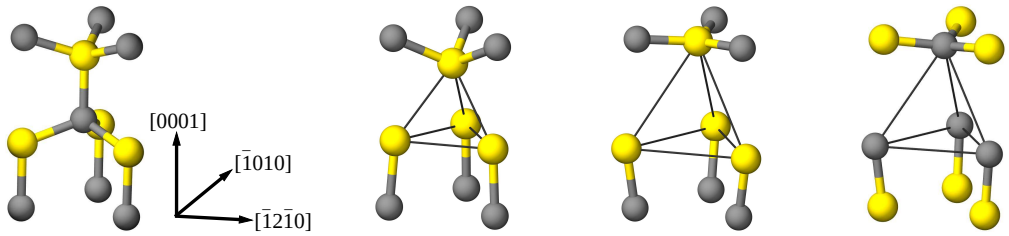

(a) ideal (b) $V_O^{\times}$ (c) $V_O^{\cdot\cdot}$ (d) V''_{Zn}

Figure 4.1.: *(a) Ideal wurtzite structure, (b) neutral oxygen vacancy ($V_O^{\times}$), (c) charged oxygen vacancy ($V_O^{\cdot\cdot}$), and (d) doubly negatively charged zinc vacancy (V''_{Zn}). Yellow and grey spheres represent zinc and oxygen atoms, respectively.*

the distinguished, the particular properties of which are described in detail in Sec. 4.3.2. Only the highly symmetric octahedral structure [18, 19, 20] has been explicitly considered before. Lee *et al.* described a structure similar to the dumbbell interstitial but did not consider all relevant charge states [21]. The rotated dumbbell (and its split-interstitial variant described below) have not been reported in the literature so far. It will be shown below and in Chapter 6 that this defect is, however, of fundamental importance for the understanding of the electronic and structural behavior as well as the migration of oxygen interstitials.

For consistency, oxygen and zinc vacancies were also included (see Fig. 4.1). Since previous first-principles studies [18, 19, 20] have shown the oxygen vacancy (V_O) to be a negative-U center with the $q = +1$ state being unstable, only the neutral and the doubly charged oxygen vacancy were considered. The zinc vacancy (V_{Zn}) was studied in charge states $2-$, $1-$ and 0.

4.2.4. Charge analysis

As a means to obtain a simple semi-quantitative measure for comparing different charge states, partial charges for all atoms in the defective cells were calculated using the Bader atom-in-molecule method. This scheme identifies extrema and saddle points in the three-dimensional electron density. Based on this information space is partitioned in polyhedra each of which is usually associated with one atom which is assigned the charge confined in the polyhedron volume [79]. For this analysis codes included in the ABINIT package were employed.

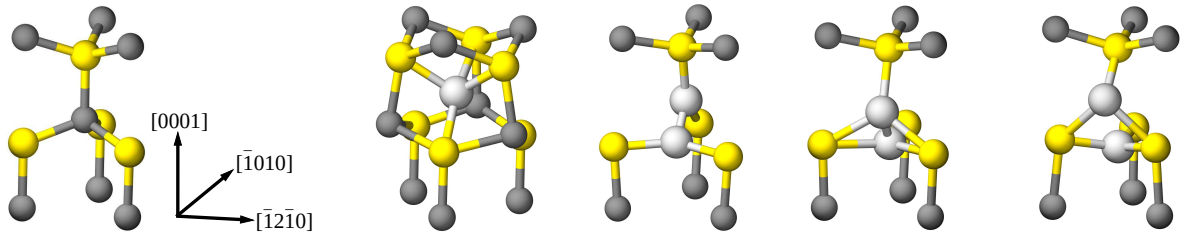

(a) ideal (b) $O_{i,oct}$ (c) $O_{i,db}$ (d) $O^{\times}_{i,rot-db}$ (e) $O^{''}_{i,rot-db}$

Figure 4.2.: *Overview of possible oxygen interstitial configurations. The yellow and dark grey spheres are the zinc and regular oxygen atoms, respectively. The interstitial oxygen atom(s) are colored in light grey. The (b) octahedral ($O_{i,oct}$) and (c) dumbbell ($O_{i,db}$) configurations are shown in the neutral charge state. In both cases the changes with varying defect charge are continuous and rather small. In contrast, the rotated dumbbell interstitial displays a distinct geometry change as the charge state varies. The geometry which occurs for (d) the neutral charge state ($O^{\times}_{i,rot-db}$) is also representative for the positive charge states; on the other hand, (e) the doubly positive configuration ($O^{''}_{i,rot-db}$) is prototypical for the negative charge states.*

Since the assignment of electron charges to atomic sites is not unique, the absolute values for the partial charges have limited quantitative significance. Therefore, in the following only relative partial charges are discussed; they have been obtained by normalizing the partial charges of the atoms in the defective system with the partial charge of an atom of the same type in an ideal cell which carries a total charge equivalent to the total charge of the supercell containing the defect.

4.3. Results

Three different configurations for the oxygen interstitial as well as the two types of vacancies were studied in detail. Firstly, the thermodynamics of these defects will be discussed. Secondly, the geometric and electronic properties which render each configuration distinct are described. Finally, a comprehensive picture of the relation between electronic structure, formation enthalpies and charge states is developed.

4.3.1. Thermodynamics

The Fermi level dependence of the formation enthalpies of native point defects is shown Fig. 4.3 for oxygen- and zinc-rich conditions. The band gap calculated at the Γ-point is

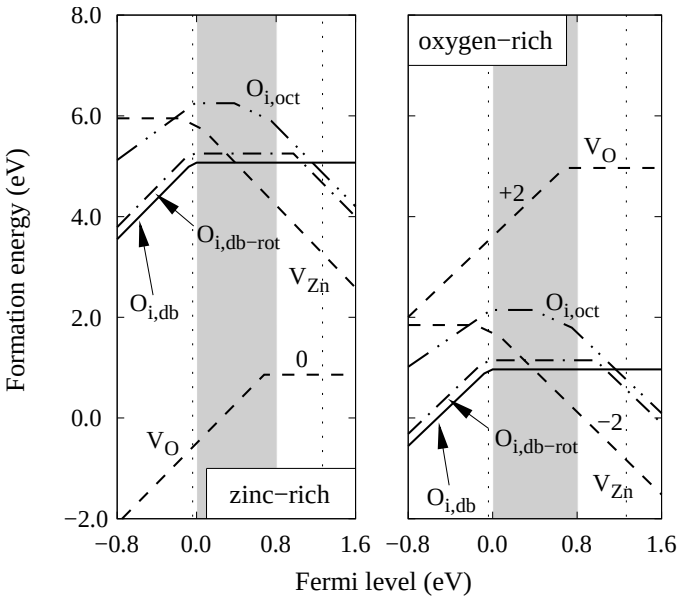

Figure 4.3: *Variation of the formation enthalpies of several point defects in zinc oxide with the Fermi level under zinc (left) and oxygen-rich (right) conditions. The numbers in the plot indicate the defect charge state; parallel lines imply equal charge states. The grey-shaded area indicates the band gap calculated at the* Γ*-point. The vertical dotted lines show the band gap which is obtained if only the special* k*-points used in the supercell calculations are considered.*

illustrated by the grey-shaded area. The vertical dotted lines indicate the band gap which is obtained if only the special k-points used in the supercell calculations are considered. Formation enthalpies for a zinc-rich environment and p-type conducting conditions ($\mu_e = 0\,\text{eV}$, VBM) are given in Tab. 4.1 together with results of previous calculations.

Under zinc-rich conditions the oxygen vacancy is the most stable defect for all Fermi levels. It shows a transition from the double positively charged state ($V_O^{\cdot\cdot}$) to the neutral configuration ($V_O^{\times}$) in the vicinity of the conduction band minimum (CBM).

For oxygen-rich conditions and Fermi levels in the upper half of the band gap, the doubly negatively charged zinc vacancy (V_{Zn}'') is the dominant defect type. When the Fermi level lies, however, in the lower half of the band gap the calculations suggest that oxygen interstitials in dumbbell configurations are the dominating point defect type and due to their low formation enthalpies should be present in significant amounts. The 2+/1+ and 2+/0 transition levels for the two dumbbell defects lie at the VBM (Fig. 4.3). Furthermore, if the band gap calculated using the special k-points (vertical dotted lines in Fig. 4.3; compare Sec. 4.2.1) is considered, the 0/2− transition level for the rotated dumbbell interstitial lies within the band gap just below the CBM.

In the following sections the implications of these findings will be discussed in more detail by analyzing both electronic structure and geometry. However, before doing so some reasoning is required to which extent the results are affected by the underestimation of the band gap. In the present chapter resort is made to a qualitative discussion following the

lines of previous works (see Ref. [80] and the Appendix of Ref. [19]). A more elaborate scheme based on an improved description of the band structure is presented in Chapter 5.

The formation enthalpy corrections for donors in the 2+ charge state are typically large and *negative*; they are smaller for donors in the 1+ and neutral charge states and sometimes even positive. In case of acceptors corrections to the formation enthalpies are usually large and *positive* and of similar magnitude for different charge states. Thus, the corrections increase the asymmetry in the formation enthalpies of donor and acceptor-like defects. These considerations have the following implications on the data presented in Fig. 4.3:

Upon correction of the band gap the formation enthalpies for the 2+ charge states of the oxygen interstitials (O_i) as well as the oxygen vacancy (V_O) are expected to be significantly lowered; whether the formation enthalpy of the 1+ states are lowered or raised is unsure. On the other hand the formation enthalpies for the neutral and negatively charged defects will rise. If the Fermi level is at the VBM, the formation enthalpies for the oxygen interstitials (O_i) vary only slightly as the charge state changes from 0 to 2+. Based on the foregoing considerations, one can, therefore, expect the 2+/0 or 2+/1+ oxygen interstitial transition levels to lie in the band gap near the VBM. The oxygen interstitial would, thus, effectively act as a donor. In general, the changes which are expected for the formation enthalpies upon band gap correction support and emphasize the importance of oxygen interstitials under oxygen-rich conditions.

4.3.2. Geometry and electronic structure

Vacancies

The oxygen vacancy is the most important intrinsic defect in zinc oxide under zinc-rich conditions. It displays a transition from the neutral state ($V_O^{\times}$) to the doubly positively charged state ($V_O^{\cdot\cdot}$) below the CBM. For the neutral oxygen vacancy ($V_O^{\times}$) the calculations reveal an *inward* relaxation of the surrounding zinc atoms of approximately 11% which form an almost perfect tetrahedron encapsulating the vacant site. On the other hand, a strong *outward* relaxation of about 19% is found for the charged vacancy ($V_O^{\cdot\cdot}$). Similar to the case of the neutral vacancy the atomic displacements are almost symmetric with respect to the vacant lattice site. The configurations are shown in Fig. 4.1. In both cases, the first nearest neighbor shells exhibit significant relaxation, while the relaxation of second and farther neighbors is almost negligible. This observation is supported by the

Table 4.1.: *Formation enthalpies of some intrinsic point defects in bulk zinc oxide for zinc-rich and p-type conducting conditions ($\mu_e = 0$ eV, VBM). Ref. [19]: DFT, LDA, norm-conserving PPs, Ref. [18]: DFT, LDA, ultrasoft PPs, Ref. [20]: DFT, GGA, ultrasoft PPs.*

Defect	**Charge**	**This work**	**Ref. [19]**		**Ref. [18]**	**Ref. [20]**[a]
			uncorr.	corr.		
V_O	0	0.9	1.5	2.4	0.0	
	+2	−0.5	−0.5	−3.0	−0.3	−0.9
V_{Zn}	0	6.0	5.8	10.6	5.5	≥ 5.1
	−1	5.8	5.7	10.1	5.8	5.0
	−2	5.9	5.8	10.1	6.6	5.1
$O_{i,rot-db}$	−2	7.2				[8.2][b]
	−1	6.6			[7.5][b]	[≥ 7.1][b]
	0	5.2			[6.5][b]	[6.0][b]
	+1	5.3			[6.5][b]	
	+2	5.4				
$O_{i,oct}$	−2	7.4	7.4[c]	9.7	7.8	7.8
	−1	6.7	6.4[c]	10.4	6.8	6.9
	0	6.2	6.2[c]	12.1	6.4	6.4
	+1	6.3			6.4	
	+2	6.3				
$O_{i,db}$	−2	9.7				
	−1	7.4				
	0	5.1				
	+1	5.1				
	+2	5.2				

[a]The data given here was derived from Fig. 1 in the original reference, since no explicit values are given.
[b]References [18] and [20] report formation enthalpies for a "tetrahedral interstitial" configuration but no details on the geometry of the relaxed configuration are given.
[c]The geometry of the oxygen interstitial in Ref. [19] is not specified.

Shell	**1st Zn** (4)	**1st O** (6)	**2nd Zn** (1)	**3rd Zn** (9)
ideal	1.952 Å	3.188 Å	3.206 Å	3.750 Å
$q = 0$	1.732 Å	3.132 Å	3.231 Å	3.740 Å
	−11.3%	−1.7%	+0.8%	−0.3%
$q = +2$	2.332 Å	3.191 Å	3.291 Å	3.679 Å
	+19.4%	+0.1%	+2.7%	+0.5%

Table 4.2: *Relaxation of first and second nearest neighbors around the oxygen vacancy. The number of atoms in the respective shell is given in brackets.*

charge analysis, which shows that the cell charge is rather well localized and practically exclusively accommodated by the atoms in first nearest neighbor shell. The changes in bond lengths are summarized in Tab. 4.2, which lists the absolute neighbor shell distances and the changes relative to the ideal bulk values. Two shells were regarded as distinct if they could be unambiguously distinguished in the ideal as well as the defective configurations. For both charge states the relaxation occurs in the same direction for almost all shells with the only exception being the single zinc atom in the 2nd neighbor shell for the neutral vacancy.

Fig. 4.4 compares the electron densities for the two charge states of the oxygen vacancy. The plots also reflect the geometry changes described in more detail above. In the case of the neutral vacancy, the inward relaxation of the zinc ions acts such as to compensate the charge deficiency due to the absent oxygen atom. This observation suggests that this vacancy type behaves in fact electronically almost neutral (i.e., similar to the ideal case) in the sense that the surrounding zinc atoms exhibit a purely "geometrical" relaxation. On the other hand, for the charged vacancy the nearest zinc atoms exhibit a strong outward relaxation and a pronounced charge depletion occurs in the immediate vicinity of the vacancy site. The positive charge (absence of electrons) is rather well localized at the vacancy site and the zinc ions behave accordingly: they carry a positive net charge and therefore sense a repulsive Coulombic force due to the also positively charged vacancy. The difference between the electronic structure of the two types of oxygen vacancies is particular obvious in the lower panel of Fig. 4.4 which shows the projection of the electron density in the (0001) oxygen layer onto the $(2\bar{1}\bar{1}0)$ plane. The Bader analysis of atomic charges (Sec. 4.2.4) provides a clear picture of the charge relaxation in the vicinity of the defect. The defect charge is predominantly accommodated by the first neighbor shell of

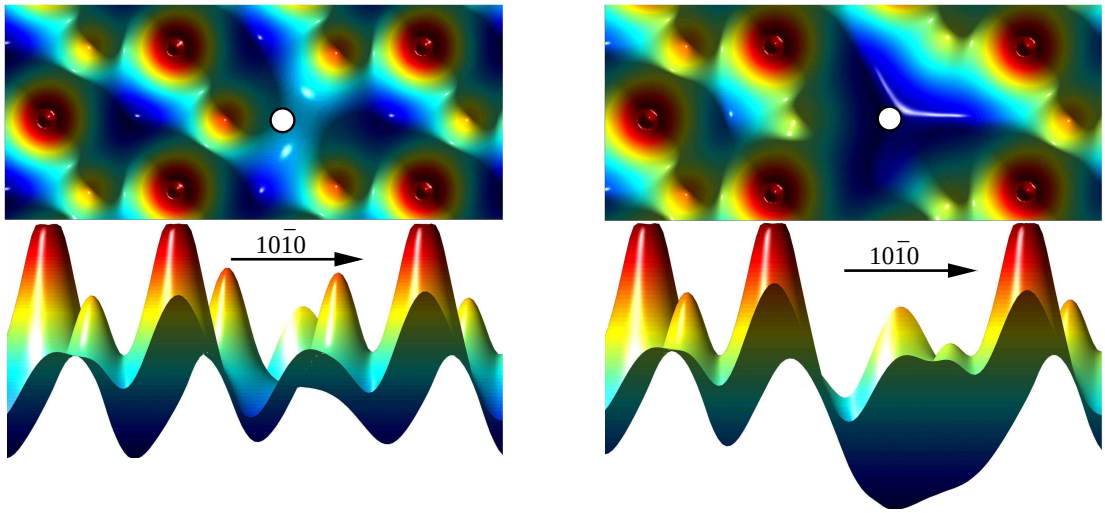

(a) neutral oxygen vacancy ($V_O^{\times}$) (b) doubly positively charged vacancy ($V_O^{\cdot\cdot}$)

Figure 4.4.: *Electron density in the (0001) oxygen layer which contains the vacancy for (a) the neutral vacancy ($V_O^{\times}$) and (b) the charged vacancy ($V_O^{\cdot\cdot}$). The white circle marks the vacant site. The upper and lower panels of each figure show the top and side views of the density surface, respectively. The zinc atoms can be well identified as the smaller hillocks in the density maps due to the penetration of the oxygen layer by the zinc valence electron density. A logarithmic representation has been chosen in order to enhance the important features of the electron density.*

zinc atoms and to a much lesser extent by the second neighbor shell of oxygen atoms. Thus, the charge imposed on the supercell is fairly well localized at the defect site.

The doubly negative zinc vacancy (V''_{Zn}) is energetically favored under oxygen-rich conditions and for Fermi levels in the upper half of the band gap (Fig. 4.1(d)). In contrast to the oxygen vacancy, the geometric structure of the zinc vacancy is practically independent of the charge state. The calculations show a symmetric outward relaxation of the first neighbor shell by about 14% while relaxations of farther neighbors are negligible.

Dumbbell interstitial

The geometric structure as well as the charge density of the neutral dumbbell interstitial ($O^{\times}_{i,db}$, equivalent to $(O_2)^{\times}_O$) is shown in Fig. 4.5. The dumbbell interstitial is characterized by two oxygen atoms which form a homonuclear bond and jointly occupy a regular oxygen lattice site. In addition, each of the two oxygen atoms forms two O–Zn bonds. The accumulation of charge along the O–O bond is indicative for a covalent bond. This oxygen

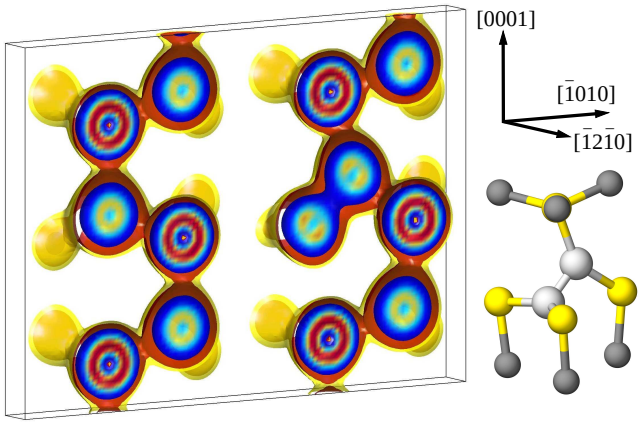

Figure 4.5: *Geometry and electron density of dumbbell interstitial configuration ($O_{i,db}$) in the neutral charge state. The electron density iso-surface plot shows a cut parallel to the ($\bar{1}2\bar{1}0$) plane. The illustration demonstrates the strong covalent bond between the two oxygen atoms of the dumbbell. Yellow and grey spheres represent zinc and oxygen atoms, respectively. The light grey spheres are the oxygen atoms which form the dumbbell.*

interstitial defect conceptually resembles the well known dumbbell interstitial defect in silicon (see e.g., Ref. [81] and references therein) and some of its features remind of the nitrogen interstitial configuration in gallium nitride [82].

The dumbbell geometry changes only marginally as the charge state varies between 2− and 2+. The bond lies in the ($\bar{1}2\bar{1}0$)-plane and is tilted with respect to the c-axis by an angle between 45° and 51°. The presence of the defect causes outward displacements of the neighboring zinc atoms between −1.0% ($q = +2$) and −2.4% ($q = 0$) if compared to the average nearest neighbor distance of the ideal structure. The largest relative displacement occurs for the uppermost zinc atom (~ 0.3 Å) which approaches the upper oxygen plane. A similar displacement forces the lower oxygen atom of the dumbbell into the lower zinc plane. The separation of the two oxygen atoms, whose positions are nearly symmetric with respect to the ideal lattice site, varies between 1.423 Å ($q = +2$) and 1.485 Å ($q = -2$), which is 15 and 20% larger than the calculated bond length in the O_2 molecule (1.241 Å).

The electronic structure of this defect can be rationalized in terms of a simplified molecular orbitals (MO) model (Fig. 4.6). The almost planar bonding configuration suggests the formation of sp^2-hybrid orbitals at both oxygen sites. Two out of the three sp^2-orbitals at each oxygen site are involved in the formation of σ-bonds to the neighboring zinc atoms. Each oxygen atom contributes effectively 3/2 electrons to each of these bonds. The remaining singly occupied sp^2-hybrids form the O–O bond. The resulting bonding $sp^2\sigma$-orbital is fully occupied while the anti-bonding $sp^2\sigma^*$-orbital remains empty. The p-orbitals (one on each of the two atoms, labeled p_x and p_y in Fig. 4.6) are not hybridized and maintain an atom-like character, since they are orthogonal to each other (Figs. 4.5 and 4.2(c)). In

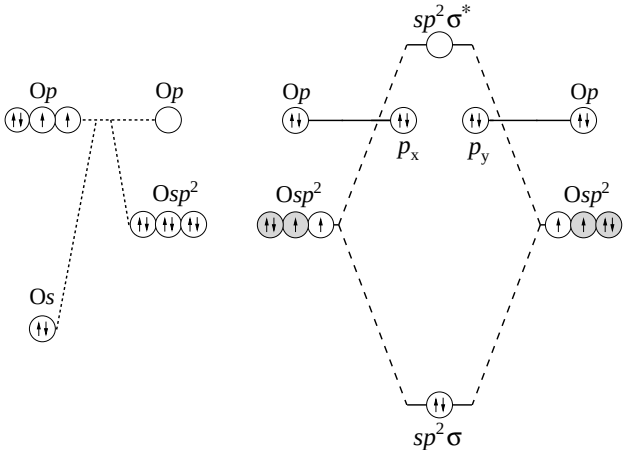

Figure 4.6: *Formal hybridization of oxygen atoms prior to formation of the O–O bond (left). Simplified MO-scheme of the electronic structure of the oxygen dumbbell configuration (right). The electron population corresponds to the neutral charge state. The grey shaded orbitals and the electrons therein are being used for the formation of O–Zn bonds.*

the case of the neutral dumbbell both of these (non-bonding) orbitals are fully occupied. In the following, the MO-scheme will turn out to be helpful for interpreting the geometric and electronic structure changes with charge state.

Fig. 4.7 shows the results of the Bader analysis of atomic charges. Between the defect charge states 0 and 2+ the net charges decrease continuously. This corresponds to a continued oxidation of the two oxygen atoms starting from a formal oxidation number −I towards a formal oxidation number 0, although this limit is eventually not reached. Over the same range the formation enthalpy stays practically constant (for a Fermi level close to the VBM, Tab. 4.1) which according to the MO-scheme occurs because the electrons in the unhybridized, atom-like p-orbitals can be removed at little energetic cost. The slight decrease of the bond length can be related to a diminishing repulsion between the electron clouds surrounding on the atoms.

In contrast, if the system is negatively charged the formation enthalpy of the oxygen dumbbell (again for a Fermi level close to the VBM) increases significantly while the net charges remain constant. The negative surplus charge is smeared evenly over the cell. Compensation of the negative surplus charges by the homonuclear oxygen bond is impossible as it would imply population of the yet unoccupied anti-bonding σ^*-orbital and thus breakage of the bond. Since surplus electrons cannot be compensated in this geometry, the oxygen dumbbell interstitial ($O_{i,db}$) cannot act as an acceptor.

Rotated dumbbell interstitial

The geometry of the rotated dumbbell ($O_{i,rot-db}$) is shown for the neutral charge state in Fig. 4.2(d) and for the doubly negative charge state in Fig. 4.2(e). For the neutral and

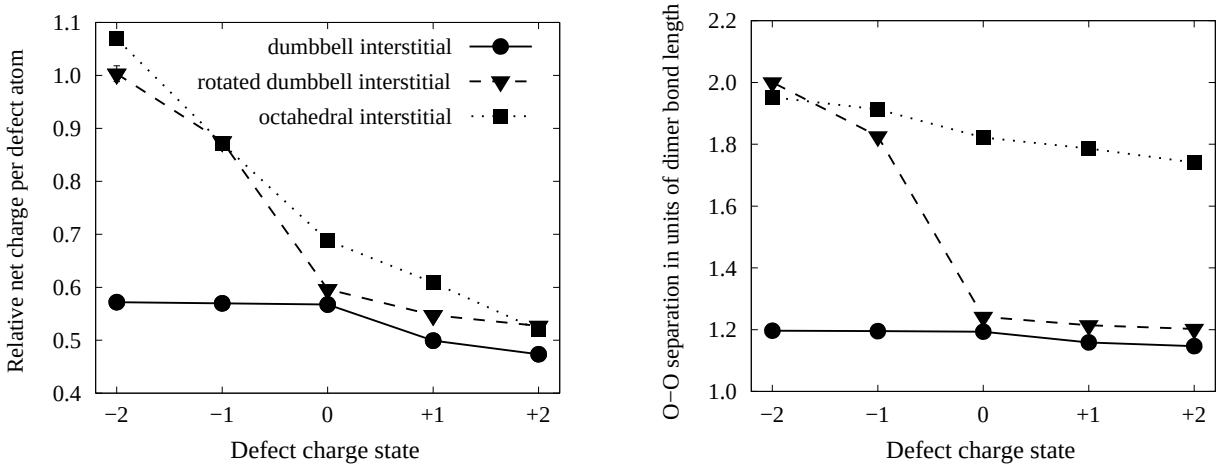

Figure 4.7.: *Relative net charge of oxygen atoms which are directly involved in interstitial configurations for different nominal charge states of the defect (left). Variation of O–O separation as a function of the charge states of the defect (right). In case of the octahedral interstitial, the O–O distances of the three nearest oxygen atoms of the second neighbor shell with respect to the central defect atom were evaluated.*

positive charge states the rotated dumbbell defect is characterized by a strong oxygen–oxygen bond akin to the regular dumbbell interstitial ($O_{i,db}$) discussed in the foregoing section. The bond is also confined to the $(\overline{1}2\overline{1}0)$-plane and tilted with respect to the c-axis by an angle between 38° and 41° depending on charge state. In fact, the two dumbbell geometries can approximately be matched by applying a sixfold mirror axis (6_m). The length of the oxygen–oxygen bond occurring for neutral and positive charge states is 20 to 24% larger than the bond length in the oxygen dimer and thus similar to the O–O separation in the regular dumbbell structure. In contrast to the dumbbell interstitial, however, each oxygen atom is bonded to three zinc atoms.

A very different behavior is found for negative charge states. The rotated dumbbell interstitial transforms into a *split-interstitial*. The two oxygen atoms maintain their mutually symmetric positions but are no longer bonded (Fig. 4.7) The split-interstitial configuration can therefore be regarded as two interstitial oxygen atoms associated with one oxygen vacancy.

Defect geometry and charge distribution underscore the similarity of the regular and rotated dumbbell in neutral and positive charge states (Fig. 4.7). As before, inspection of the net charges reveals an almost perfect localization of the defect charge on the two oxygen

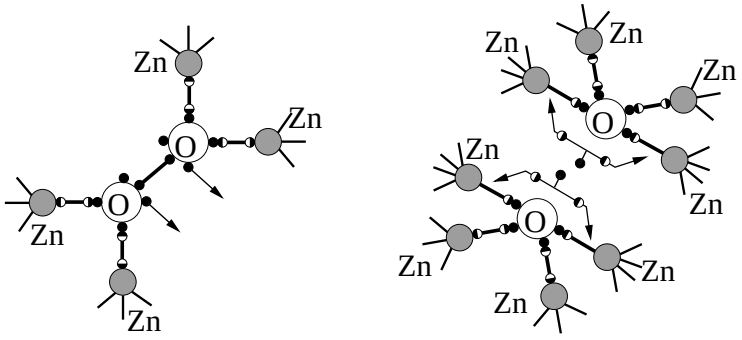

Figure 4.8.: *Interpretation of the structural changes with charge state of the rotated dumbbell oxygen interstitial ($O_{i,rot-db}$) in terms of a simple electron counting scheme. Neutral and positive charge states (left): electrons can be withdrawn with little effort (picture also valid for dumbbell interstitial). Negative charge states (right): O–Zn bonds are preferred because they can accommodate more electrons than O–O bonds (not applicable to dumbbell interstitial). Large white circles: oxygen atoms; medium sized grey circles: zinc neighbor; small (half) filled circles represent ("half") electrons.*

atoms forming the core of the defect. Going from charge state 1− to the neutral charge state the formation of the homonuclear oxygen bond is accompanied by a discontinuous decrease of the net charges by more than 30%.

For negative charge states, the surplus electrons are localized on the two oxygen atoms forming the split-configuration. This behavior is very distinct from the case of the dumbbell interstitial ($O_{i,db}$) for which delocalization of the extra charge is observed in case of negatively charged cells. In fact, for the doubly negative charge state the defective oxygen atoms have achieved the same net charge state as oxygen atoms on regular lattice sites and thus have a nominal oxidation number of −II. For these charge states, as illustrated in Fig. 4.7 the rotated dumbbell interstitial ($O_{i,rot-db}$) strongly resembles the octahedral interstitial if net charge and O–O separation are considered. Unlike the case of the dumbbell interstitial, in both the octahedral as well as the rotated dumbbell configuration O–O bonds are absent in negative charge states.

The changes with charges state observed for the rotated dumbbell interstitial ($O_{i,rot-db}$) can be interpreted in terms of a simple electron counting scheme as demonstrated in Fig. 4.8. In neutral and positive charge states the system can achieve a saturated bonding configuration (two electrons per bond) by forming a homonuclear oxygen bond. Electrons can be withdrawn at little energetic cost from atom-like oxygen orbitals in analogy to the MO-scheme for the dumbbell interstitial ($O_{i,db}$) shown in Fig. 4.6. In negative charge states

O–Zn bonds are energetically preferred. Since each zinc atom contributes only "half" an electron to each of its four bonds, excess electrons can be rather easily accommodated.

In conclusion, the oxygen atoms are able to adopt the formal oxidation state −II in the negative charge state limit and they approach the oxidation state 0 in the positive charge limit. Thereby, they realize the peroxo-like defect proposed in the introduction.

4.4. Discussion

The present calculations indicate that in neutral and positive charge states the energetically preferred mechanism for accommodation of surplus oxygen is the formation of a homonuclear oxygen bond. In such a configuration all bonds are saturated and electrons can be easily removed from non-bonding orbitals. Positive charge states of the dumbbell configurations have, therefore, low formation enthalpies and can act as traps for holes in p-type doped samples. If the system is negatively charged, it strives to form additional (initially unsaturated) O–Zn bonds which are compensated by the surplus electrons. Therefore, the split-interstitial and octahedral interstitial configurations are favorable for negative charge states.

In the regular dumbbell configuration ($O_{i,db}$) for negative charge states, the two oxygen atoms are constrained to the dumbbell structure and are not able to adopt an energetically more favorable configuration. The opposite seems to apply for the octahedral interstitial ($O_{i,oct}$) in positive charge states; the surplus oxygen atom strives to form homonuclear oxygen bonds, but it is encapsulated in a cage of zinc atoms, which it cannot leave without activation. Hence, in both cases energetic barriers exist, which are associated with large defect formation enthalpies for the respective unfavorable charge states.

The rotated dumbbell interstitial ($O_{i,rot-db}$) incorporates the energetic advantage of oxygen–oxygen bonding for positive charge states, while for negative charge states the geometry allows breakage of the oxygen–oxygen bond in favor of the formation of oxygen–zinc bonds. The resulting split-interstitial configuration for negative charge states involves the formation of four oxygen–zinc bonds for each atom of the oxygen pair. The defect energies reveal that the gain in energy due to the formation of three additional oxygen–zinc bonds by the two oxygen atoms in the split-interstitial configuration overcompensates the energetic cost for leaving the original oxygen site unoccupied as the formation enthalpy

of the rotated dumbbell interstitial ($O_{i,rot-db}$) is lower than the formation enthalpy of the octahedral defect ($O_{i,oct}$).

4.5. Conclusions

In summary, DFT calculations have been performed on the stability and the structure of oxygen interstitials and vacancies. The oxygen vacancy is the most stable defect for zinc-rich conditions. Under oxygen-rich conditions the zinc vacancy is energetically preferred for Fermi levels in the upper half of the band gap, while for Fermi levels in the lower half of the band gap oxygen interstitials in dumbbell configurations are the dominant defect types. These defects are characterized by a covalent oxygen–oxygen bond under neutral and positive charging. In the introduction a peroxo-like defect has been proposed and the possibility has been formulated that the oxygen atoms forming the defect are oxidized as the Fermi level is pushed towards the VBM. This proposition is realized by the two dumbbell configurations ($O_{i,db}$ and $O_{i,rot-db}$). In the neutral charge state the pair of oxygen atoms electronically resembles a single oxygen atom in an unperturbed crystal, nominally equivalent to $(O_2)_O^\times$. In this state both oxygen atoms are in the formal oxidation state $-$I. As the defect is charged increasingly positive the decreasing net charges of the atoms indicate further oxidation and the two dumbbell atoms approach a formal oxidation number of zero. The rotated dumbbell is a particular interesting case as the oxygen pair cannot only be oxidized (like the dumbbell interstitial), but is also able to assume a configuration in which the defect atoms carry a net charge equivalent to the ideal bulk value (oxidation state $-$II). This is achieved by breakage of the oxygen–oxygen bond in favor of the formation of several additional oxygen–zinc bonds. While the oxygen dumbbell configuration ($O_{i,db}$) is a candidate for compensation of p-type doping under oxygen-rich conditions, the rotated dumbbell oxygen interstitial defect ($O_{i,rot-db}$) might also act as a compensating defect for n-type doping.

5. Role of band structure, volume relaxation and finite size effects*

Density functional theory (DFT) calculations of intrinsic point defect properties in zinc oxide were performed in order to remedy the influence of finite size effects and the improper description of the band structure. The generalized gradient approximation (GGA) with semi-empirical self-interaction corrections (GGA+U) was applied to correct for the overestimation of covalency intrinsic to GGA-DFT calculations. Elastic as well as electrostatic image interactions were accounted for by application of extensive finite-size scaling and compensating charge corrections. Size-corrected formation enthalpies and volumes as well as their charge state dependence have been deduced. The present results partly confirm earlier calculations from the literature and from Chapter 4 of the present work, but reveal a larger number of transition levels: (1) For both, the zinc interstitial as well as the oxygen vacancy, transition levels are close to the conduction band minimum. (2) The zinc vacancy shows a transition rather close to the valence band maximum and another one near the middle of the calculated band gap. (3) For the oxygen interstitials, transition levels occur both near the valence band maximum and the conduction band minimum.

5.1. Introduction

In the foregoing chapter, density functional theory (DFT) calculations on the structure and stability of intrinsic point defects in ZnO have been presented. The major uncertainty in these calculations as well as other theoretical studies [18, 19, 20, 21, 67, 83, 84] is the

*Parts of the present chapter have been published in Ref. [4].

underestimation of the band gap (theory: 0.7–0.9 eV, experiment: 3.4 eV) and the improper description of the band structure. All of these calculations were based on the local density (LDA) or generalized gradient approximation (GGA).

The underestimation of the band gap is an intrinsic shortcoming of the DFT method in general (see e.g., Refs. [85, 86]). The improper description of the band structure is of particular importance in the case of zinc oxide because self–interactions intrinsic to the LDA and GGA exchange–correlation functionals cause an energy level shift of the Zn-3*d* states. As a result, the calculations not only yield a band gap error of more than 2 eV but also overestimate the covalency of the Zn–O bond. A direct comparison between data calculated within LDA or GGA-DFT and experiment is, therefore, severely hampered. In the past, this problem has been addressed in various ways: Zhang *et al.* proposed an empirical correction scheme based on a Taylor expansion of the formation enthalpies in the plane wave cutoff energy [19, 80]. Since a profound physical motivation for this scheme is lacking, the results can only be interpreted semi-quantitatively. Kohan *et al.* discussed corrections based on the electronic structure of the defect configurations [18], while other studies (including the Chapter 4) resorted to a qualitative discussion [20].

If no correction is applied the calculated formation enthalpies reported by different authors are comparable (see Tab. 4.1 below), whereas the various correction schemes lead to very different results. This can be illustrated for the case of the oxygen vacancy. According to the data of Kohan *et al.* the 2+/0 transition for this defect should be located in the vicinity of the valence band maximum (VBM) [18], while the corrected data by Zhang *et al.* predict the same transition to occur just below the conduction band minimum (CBM) [19]. Since it is difficult to assess the reliability of these predictions, quantitatively more reliable calculations are required.

Recently, some defect calculations were carried out using the semi-empirical LDA+U scheme [26], which allows to adjust the position of d-electron levels by implementing self-interaction corrections into the LDA or GGA exchange-correlation potentials. Hitherto, this scheme has been employed to study point defects in $CuInSe_2$ where the Cu-3*d* electrons play a similar role as the Zn-3*d* electrons in ZnO [87], and in calculations of optical transition levels of the oxygen vacancy in ZnO [22, 23]. For this reason, the method is an excellent candidate for a reassessment of the thermodynamics of point defects in zinc oxide. Another issue, which has hardly been addressed in studies of point defects in zinc oxide so far, is the role of volume relaxation and finite size effects. It is, however, well

known, that formation enthalpies can converge slowly with supercell size [88], especially if charged defects are considered [89].

The purpose of the present chapter is twofold. Firstly, formation enthalpies for the intrinsic point defects in zinc oxide are to be determined correctly taking into account the role of the Zn-3d electrons. Furthermore, the effect of supercell size and volume relaxation is studied by employing finite size scaling. Defect formation volumes are derived which have not been calculated for ZnO up to now. In summary, by taking into account the band structure as well as finite size effects, a consistent set of point defect properties is derived, which will allow for a more quantitative interpretation of experimental data.

In the following section, some observations on the band structure of zinc oxide based on experimental as well as theoretical studies are summarized. This overview allows to motivate the computational approach which is described in Sec. 5.3. The results are compiled in Sec. 5.4. An interpretation and a comparison with literature are given in Sec. 5.5.

5.2. Band structure of zinc oxide

Experimentally the electronic structure of zinc oxide has been investigated in some detail (see Ref. [90] and references therein). Typically, the density of states reveals two primary bands between 0 and $-10\,\mathrm{eV}$ (measured from the VBM). The upper band is primarily derived from O-2p and Zn-4s orbitals, while the lower band arises almost solely from Zn-3d electrons with a maximum between -7 and $-8\,\mathrm{eV}$ [91, 92]. From X-ray photoelectron spectra the admixture of Zn-3d states in the O-2p band has been determined to be about 9% indicating a small covalent contribution to bonding [93]. The band dispersion has been investigated via angle-resolved photoelectron spectroscopy along a few high-symmetry directions [94, 95]. The measurements reveal a strong dispersion of the upper valence bands and a small dispersion of the Zn-3d levels. Zinc oxide displays a direct band gap of about $3.4\,\mathrm{eV}$ at the Γ-point.

In general, DFT calculations yield too small band gaps compared to experiment. The effect is further enhanced in ZnO due to the underestimation of the repulsion between the Zn-3d and conduction band levels [92]. This leads to a significant hybridization of the O-2p and Zn-3d levels [92], and eventually to an overestimation of covalency [96]. Schröer *et al.* [97] performed an analysis of the wavefunctions obtained from self-consistent pseudopotential calculations and determined a contribution of 20 to 30% of the Zn-3d

orbitals to the levels in the upper valence band (to be compared with the experimental estimate of 9% covalency cited above [93]). For zinc oxide the band gap calculated with LDA or GGA is about 0.7–0.9 eV, which is just about 25% of the experimental value (3.4 eV) [18, 19, 20, 92, 97] (also compare previous chapter).

The insufficient description of strongly localized electrons (such as those occupying the Zn-3*d* states in ZnO) and the underestimation of their binding energies is a generic problem of DFT within the LDA or GGA, and at least partially a result of unphysical self-interactions [98]. In fact, it has been found that calculations based on the Hartree-Fock or the GW approximation give much more tightly bound *d*-electrons and significantly larger band gaps [92, 99]. An alternative approach is the explicit correction of self-interaction [100]. Vogel *et al.* have developed this idea further and devised a scheme, which allows to incorporate self-interaction corrections (SIC) and electronic relaxation corrections (SIRC) already during the construction of pseudopotentials (PP) [98]. Thereby, they were able to reproduce the experimental band gap as well as the position of the 3*d* levels in several II-VI compounds with remarkable precision. In fact, the thus obtained band structure for ZnO compares better with experiment than calculations within the Hartree-Fock and GW approximations [92, 99]. SIC-PPs have also been used by Zhang *et al.* in the calculation of the formation enthalpies of a few neutral point defects in zinc oxide [19]. Unfortunately, as they point out, the SIC scheme cannot be transferred unambiguously to charged defect calculations and is therefore not applicable in the present situation.

5.3. Methodology

5.3.1. Calibration of GGA+U method

The problems related to tightly bound electrons within LDA and GGA-DFT have motivated the development of the so-called LDA+U (or equivalently GGA+U) method [26, 54, 55, 56]. In this scheme self-interaction corrections are included heuristically by considering the (orbital dependent) on-site repulsion between electrons. The scheme has been quite successful in describing the electronic properties of several transition metal oxides for which conventional LDA and GGA calculations fail to reproduce the experimentally observed ground states [26, 54, 55, 56]. The method has also been employed for studying ferromagnetism in ZnO codoped with transition metals [101] and for calculating absorption

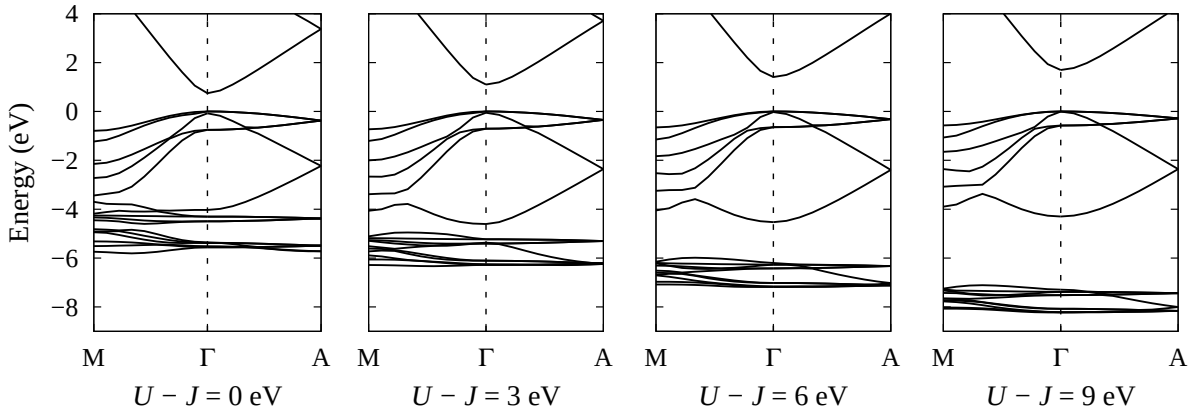

Figure 5.1.: *Band structures obtained from density functional theory calculations within the generalized gradient approximation using self-interaction corrections (GGA+U). The formulation of Dudarev et al. [54] was applied with different values of $\bar{U} - \bar{J}$. Calculations performed for lattice constants relaxed at $\bar{U} - \bar{J} = 0$ eV.*

spectra of nanostructured ZnO [102]. The work by Zhao *et al.* [87] is of particular interest in the present context as it illustrates the applicability of the LDA+U approach to the study of point defects. These authors employed the LDA+U method to adjust the position of the Cu-3d levels in $CuInSe_2$ by tuning the self-interaction parameter U. More recently, the LDA+U method has also been employed in the study of the optical transitions of the oxygen vacancy in zinc oxide [23, 22]. In the present work a similar scheme is applied in order to obtain a realistic representation of the Zn-3d electrons in zinc oxide.

To begin with, the GGA+U method needs to be calibrated and benchmarked. In the present work the formulation by Dudarev *et al.* [54] has been adopted. In this approach, the only free parameter is the difference $\bar{U} - \bar{J}$ between the matrix elements of the screened Coulomb electron-electron interaction. The on-site interaction correction was applied for the Zn-3d electrons only and the position of the Zn-3d bands was tuned by adjusting the difference $\bar{U} - \bar{J}$. The calculations were carried out within density functional theory (DFT) as implemented in the Vienna ab-initio simulation package (VASP) [103] using the projector-augmented wave (PAW) method [62, 104]. The parameterization by Perdew and Wang (PW91) [25] was used for the exchange–correlation functional. A non-shifted Γ-point centered $4 \times 4 \times 4$ k-point mesh was used for Brillouin zone sampling. In all calculations, the plane wave energy cutoff was set to 500 eV giving a technical error due to discretization of the Brillouin zone integrals and incomplete basis set of less than 1 meV.

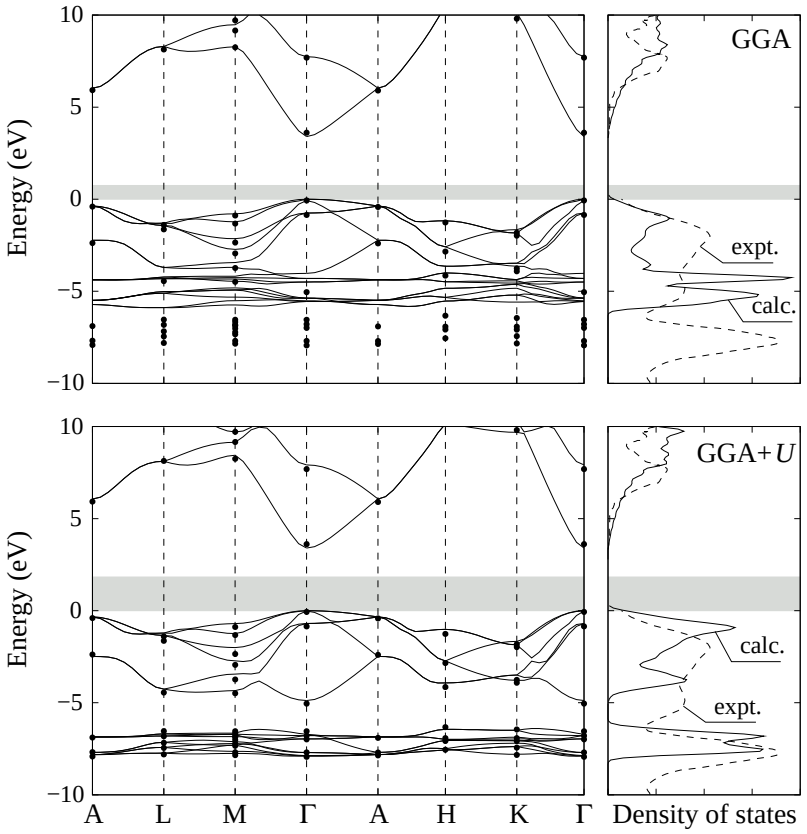

Figure 5.2: *Band structures obtained from density functional theory calculations within the generalized gradient approximation (GGA) (top) and using the GGA+U method with $\bar{U} - \bar{J} = 7.5\,eV$ (bottom). The conduction band states have been rigidly shifted to the experimental band gap. The small black circles represent data from self-interaction and relaxation corrected (SIRC) pseudopotential calculations (Ref. [98]). In the plots on the right the solid and dashed lines show the calculated and experimental (Ref. [90]) density of states, respectively. The grey stripe indicates the calculated band gap.*

The equilibrium configuration of the unit cell was determined by calculating the energy-volume curve of the system with full relaxation of internal positions. The structures were optimized until the forces were converged to better than 5 meV/Å. As experimental data on band dispersion is sparse (see Sec. 5.2), the calculations were benchmarked using the band structure calculated by Vogel *et al.* for which they employed SIRC pseudopotentials and which reproduces the experimental band gap as well as the position of the Zn-3d levels [98].

Values for $\bar{U} - \bar{J}$ between 0 and 10 eV were considered. As $\bar{U} - \bar{J}$ is raised the Zn-3d states are shifted downwards and the band gap increases as illustrated in Fig. 5.1. At the same time the equilibrium volume decreases while the bulk modulus varies only slightly. Eventually, a value of $\bar{U} - \bar{J} = 7.5\,\text{eV}$ was chosen, for which the valence band energy levels as well as the position of the Zn-3d levels are in very good agreement with the SIRC calculations as well as experiment. The band gap calculated using the GGA+U scheme is

1.83 eV, which constitutes a significant improvement over GGA. With otherwise identical parameters the latter yields a band gap of 0.75 eV.

A comparison of GGA, GGA+U, and SIRC band structure calculations is shown in Fig. 5.2. (For better visualization, the conduction band has been rigidly shifted upwards by the remaining band gap error). The right hand panel compares the calculated density of states (DOS) with experimental data measured via photoelectron spectroscopy [90]. (Since the excitation probabilities for s, p, and d electrons change with $h\nu$, the experimental DOS varies strongly with the energy of the incoming photons [91]. In order to simplify comparison some of the bands have been rescaled).

The GGA calculations (equivalent to $\bar{U} - \bar{J} = 0\,\text{eV}$) underestimate the binding energies of the Zn-3d states leading to a drastic overestimation of the hybridization between the O-2p and Zn-3d levels. Compared to experiment and the SIRC calculations, the GGA+U calculation yields a slightly smaller dispersion of the upper valence band and a yet smaller difference in the position of the Zn-3d band[†]. It also reproduces the double feature in the Zn-3d bands reported by Zwicker and Jacobi [94] as well as Girard *et al.* [95]. Overall, the agreement of the GGA+U band structure and density of states with SIRC calculations as well as experiments is very good.

5.3.2. Defect calculations

For the defect calculations hexagonal supercells with 32 to 108 atoms were used equivalent to $2 \times 2 \times 2$ to $3 \times 3 \times 3$, primitive unit cells. In these calculations a non-shifted Γ-point centered $2 \times 2 \times 2$ k-point mesh was employed. All calculations were performed within GGA as well as GGA+U in order to quantify the energy corrections.

Firstly, the atomic positions were relaxed with all cell parameters fixed at the ideal bulk values (Sec. 5.4.1) until the forces were converged to better than 5 meV/Å. Then the energy-volume curves for the supercells were computed with fixed atomic coordinates. The minimum of the curve provided the relaxed volume of the defective cell, V_{def}, which allowed to calculate the formation volume according to (see e.g. Refs. [105, 106, 107])

$$\Delta V_D = V_{def} - \frac{N_{def}}{N_{id}} V_{id}. \tag{5.1}$$

[†]With respect to numerical accuracy in particular regarding the Zn-3d levels, it must be acknowledged that the experimental data displays some variation as values in the range between −7 and −8 eV have been reported [90, 94, 95].

Here, V_{id} and N_{id} denote the volume and the number of atoms in the ideal reference system, and N_{def} denotes the number of atoms in the defective cell. The data were then subjected to finite-size scaling in a similar manner as the formation enthalpies. The formation volume determines the pressure dependence of the formation enthalpy ($\Delta V_D = \partial \Delta G_D / \partial p$).

Earlier DFT calculations within LDA and GGA consistently gave very high formation enthalpies for antisite defects [18, 19, 20] and there is no reason to assume that their formation enthalpies would be significantly lowered within GGA+U. After all, the following point defects were considered: the oxygen vacancy (V_O), the octahedral oxygen interstitial ($O_{i,oct}$), the dumbbell oxygen interstitial ($O_{i,db}$), the rotated dumbbell interstitial ($O_{i,rot-db}$), the zinc vacancy (V_{Zn}) and the octahedral zinc interstitial ($Zn_{i,oct}$). With the exception of the latter the geometric structures of these defects have been described in the preceding chapter. The variation of the formation enthalpies with chemical potential and Fermi level was calculated using equation (4.8).

Knowledge of the formation enthalpies of the fully relaxed defects also allows to derive the thermal (equilibrium) transition level between charge states q_1 and q_2 for a given defect according to

$$\epsilon = -\frac{\Delta H_D(q_1) - \Delta H_D(q_2)}{q_1 - q_2} \tag{5.2}$$

where $\Delta H_D(q_1)$ and $\Delta H_D(q_2)$ denote the formation enthalpies at the valence band maximum for charge states q_1 and q_2, respectively.

5.4. Results

5.4.1. Ground state properties

Crystallographic parameters for w-ZnO calculated by the GGA+U method are $a = 3.196$ Å, $c/a = 1.606$, and $u = 0.381$ which compare very well with the experimental values[‡] $a = 3.24$ Å, $c/a = 1.600$, and $u = 0.382$. From fitting the energy-volume data to the Birch-Murnaghan equation of state [108] a bulk modulus of 136 GPa was determined in good agreement with the experimental value of 143 GPa. The calculation gave a formation enthalpy of $\Delta H^f = -3.46$ eV/f.u. which compares very well with the experimental value

[‡]The experimental data cited in this section was obtained from Refs. [71, 73, 72, 74, 75].

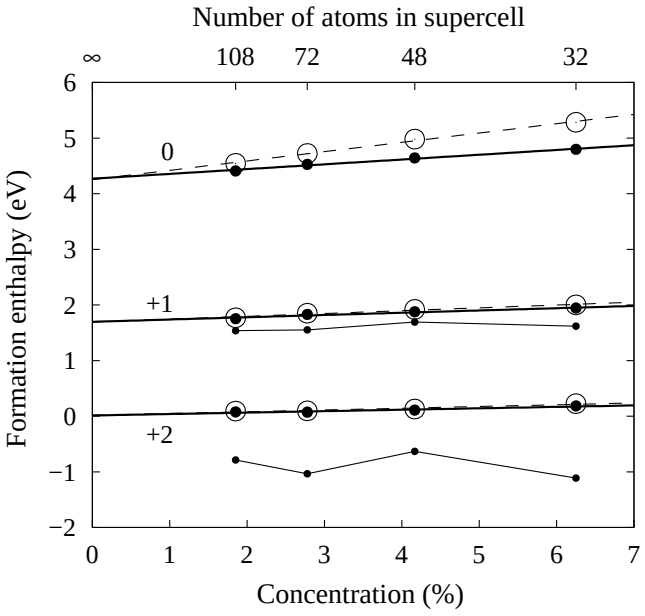

Figure 5.3: *Scaling behavior of formation enthalpies with concentration (equivalent to the inverse cell volume) exemplified for the case of the zinc interstitial ($Zn_{i,oct}$). For the charged defects the small circles show the data before monopole-monopole corrections are applied (Ref. [109]). Large filled circles correspond to formation enthalpies after volume relaxation while large open circles show the data obtained at fixed volume. The data presented here have been computed using the GGA+U method.*

of $\Delta H^f = -3.58\,\mathrm{eV/f.u.}$ The GGA calculations gave $a = 3.283\,\text{Å}$, $c/a = 1.611$, $u = 0.378$, $B = 149\,\mathrm{GPa}$, and $\Delta H^f = -3.55\,\mathrm{eV/f.u.}$.

Furthermore, the cohesive energies of pure oxygen and zinc were determined, since they enter the calculation of the formation energy of zinc oxide as well as the defect formation enthalpies. For hcp-zinc a cohesive energy of $E_c = -1.115\,\mathrm{eV/atom}$, and lattice constants of $a = 2.641\,\text{Å}$ and $c/a = 1.930$ (experimental values: $E_c = -1.359\,\mathrm{eV/atom}$, $a = 2.660\,\text{Å}$, $c/a = 1.828$) were obtained; for the oxygen dimer the calculation yielded a dimer energy of $D_0 = 8.80\,\mathrm{eV}$ and a bond length of $r_0 = 1.238\,\text{Å}$ (experimental values: $D_0 = 5.166\,\mathrm{eV}$ and $r_0 = 1.208\,\text{Å}$).

5.4.2. Finite size scaling

Strain interactions typically scale as $\mathcal{O}(V^{-1}) = \mathcal{O}(N^{-1}) = \mathcal{O}(c)$, where V is the supercell volume, N is the number of atoms, and c is the defect concentration in the supercell. In order to obtain the formation enthalpies at infinite dilution, results obtained from calculations with supercells comprising 32, 48, 72, and 108 atoms were extrapolated. For neutral defects the data can well be fitted by a straight line as shown in Fig. 5.3. The formation enthalpy at infinite dilution is given by the abscissa of the linear fit.

For charged defects, Makov and Payne have shown that additional energy contributions have to be included in order to correct for image charge interactions [109]. They derived

the correction in the form of a multipole expansion. The first term in this expansion corresponds to monopole-monopole interactions; it scales as $\mathcal{O}(V^{-1/3})$ and was explicitly taken into account in the present chapter. The magnitude of this correction is visualized in Fig. 5.3.

Since dipole-dipole and monopole-quadrupole interactions scale as $\mathcal{O}(V^{-1}) = \mathcal{O}(N^{-1}) = \mathcal{O}(c)$ [109] and thus show the same scaling behavior as the interactions of the strain fields, they are implicitly considered through the finite size scaling procedure. Fig. 5.3 shows that indeed after correction of the monopole-monopole term the data for the zinc interstitial are well described by a linear fit.

5.4.3. Formation enthalpies

Formation enthalpies calculated by the GGA+U method are given in Tab. 5.1. This compilation of data also includes the results of the GGA calculations and the data of previous DFT studies. For most defects and charge states the extrapolation errors are very small confirming the reliability of the procedure employed. In these cases the multipole-expansion-based correction scheme works excellent [109]. Larger errors arise for oxygen dumbbell interstitials in charge states 2± and for the octahedral oxygen interstitial in charge state 2+. For the dumbbell defects ($O_{i,db}$, $O_{i,rot-db}$) the defect core comprises two atoms (compare previous chapter and Ref. [6]) which renders them distinct from the other defects considered here. Higher order moments in the multipole expansion would be required in order to fully capture these features. For the octahedral interstitial ($O_{i,oct}$) in charge state 2+ analysis of the electron density shows significant charge delocalization which cannot be described by a *finite* multipole expansion [109].

If the difference between the present GGA and GGA+U results are compared with the corrections calculated by Zhang *et al.* [19], agreement of the general trends is found. The differences between the present GGA and GGA+U data are smaller than the predictions of the correction scheme of Zhang *et al.* [19], which is, however, consistent with the band gap underestimation still present in the GGA+U calculations. For the neutral oxygen vacancy and the neutral zinc interstitial (where comparison is possible) the trends agree with SIC-PP calculations [19]. The present results yield further support for the qualitative argumentation put forth by Zhang and coworkers regarding the trends expected upon band

Table 5.1.: *Calculated formation enthalpies for point defects in bulk zinc oxide for zinc-rich and p-type conducting conditions ($\mu_e = 0$ eV, VBM); the second column under GGA and GGA+U gives the error of the extrapolation to infinite dilution. Ch. 4: DFT, LDA, norm-conserving PPs; Ref. [18]: DFT, LDA, ultrasoft PPs; Ref. [19]: DFT, LDA, norm-conserving PPs; Ref. [20]: DFT, GGA, ultrasoft PPs.*

Defect	**Charge**	**This chapter**				**Ch. 4**	**Ref. [18]**	**Ref. [19]**		**Ref. [20]**[a]
		GGA		GGA+U				uncorr.	corr.	
$Zn_{i,oct}$	0	2.50	0.03	4.25	0.03		1.7	3.4	6.2	1.2
	+1	0.98	0.02	1.69	0.03		1.3	1.5	2.1	≥ 0.4
	+2	0.33	0.07	0.02	0.03		0.9	−0.2	−2.3	−0.6
V_O	0	1.00	0.06	1.71	0.04	0.9	0.0	1.5	2.4	
	+1	0.26	0.03	0.71	0.03		0.2	0.8	1.5	
	+2	−0.48	0.02	−0.73	0.03	−0.5	−0.3	−0.5	−3.0	−0.9
$O_{i,db}$	0	4.61	0.05	4.70	0.07	5.1				
	+1	4.76	0.07	4.59	0.02	5.1				
	+2	5.36	0.33	5.08	0.27	5.2				
$O_{i,rot-db}$	−2	7.70	0.40	8.79	0.17	7.2				[8.2][b]
	−1	6.51	0.28	7.08	0.04	6.6	[7.5][b]			[≥ 7.1][b]
	0	4.87	0.03	4.96	0.04	5.2	[6.5][b]			[6.0][b]
	+1	5.07	0.07	4.91	0.05	5.3	[6.5][b]			
	+2	5.67	0.72	5.41	0.29	5.4				
$O_{i,oct}$	−2	7.84	0.13	8.97	0.07	7.4	7.8	[7.4][c]	[9.7][c]	7.8
	−1	6.65	0.05	7.33	0.03	6.7	6.8	[6.4][c]	[10.4][c]	6.9
	0	6.20	0.03	6.60	0.03	6.2	6.4	[6.2][c]	[12.1][c]	6.4
	+1	6.36	0.11	6.60	0.10	6.3	6.4			
	+2	6.95	0.37	7.09	0.34	6.3				
V_{Zn}	−2	6.32	0.11	7.06	0.05	5.9	6.6	5.8	10.1	5.1
	−1	5.57	0.08	5.96	0.05	5.8	5.8	5.7	10.1	5.0
	0	5.35	0.04	5.60	0.01	6.0	6.0	5.8	10.6	≥ 5.1

[a] The data given here was derived from Fig. 1 in the original reference, since no explicit values are given.
[b] References [18] and [20] report formation enthalpies for a "tetrahedral interstitial" configuration but no details on the geometry of the relaxed configuration are given.
[c] The geometry of the oxygen interstitial is not specified in Ref. [19].

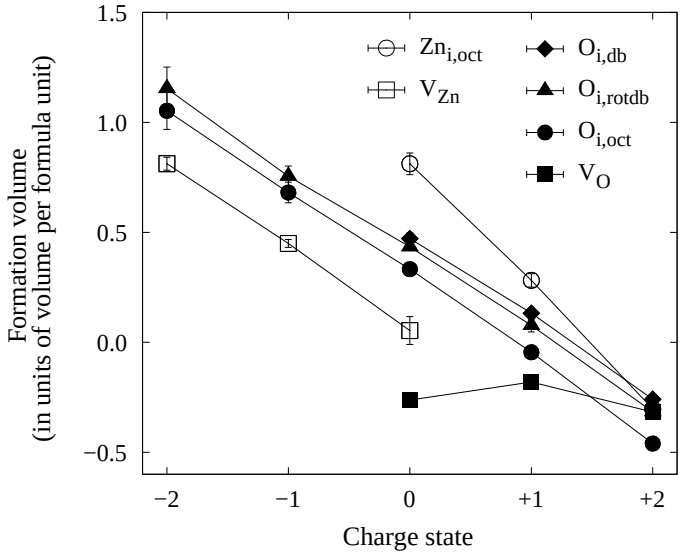

Figure 5.4: *Variation of defect formation volumes with charge state. Open and closed circles indicate defects on the zinc and oxygen-sublattices, respectively.*

gap correction [80]. The formation enthalpy correction is negative for positively charged defects, positive for neutral and yet more positive for negatively charged defects.

5.4.4. Geometries

For almost all defects the dependence of the atomic displacements on the supercell size is quite small giving evidence for the strain fields being rather short-ranged. For the vacancies and the octahedral interstitials the relaxations maintain the threefold symmetry axis of the lattice. For V_{Zn}, $O_{i,oct}$ and $Zn_{i,oct}$ the displacements change continuously with addition or subtraction of electrons. The observations regarding the charge-state dependent relaxation behavior of the oxygen vacancy described in the foregoing chapter are confirmed. For the neutral and positively charged oxygen dumbbell the oxygen-oxygen bond length is found to be between 15% ($q = +2$) and 23% ($q = 0$) longer than the calculated dimer bond length, which is again in full agreement with the earlier calculations (Sec. 4.3.2).

5.4.5. Formation volumes

The defect formation volumes obtained via equation (5.1) and subjected to finite-size scaling are given in Tab. 5.2 and plotted as a function of charge state in Fig. 5.4. With the exception of the oxygen vacancy all defects display the same trend. As electrons are added to the system the formation volume rises linearly. The slope for the oxygen interstitials as well as the zinc vacancy is roughly $-0.37\,\Omega_{\mathrm{f.u.}}/\mathrm{e}$ while for the zinc interstitial it amounts

Defect	Charge state				
	$q=-2$	$q=-1$	$q=0$	$q=+1$	$q=+2$
$Zn_{i,oct}$			0.81	0.28	−0.30
			(0.05)	(0.03)	(0.04)
V_O			−0.26	−0.18	−0.32
			(0.01)	(0.01)	(0.01)
$O_{i,db}$			0.47	0.13	−0.26
			(0.03)	(< 0.01)	(< 0.01)
$O_{i,rot-db}$	1.15	0.76	0.43	0.08	−0.32
	(0.10)	(0.05)	(0.01)	(0.03)	(0.01)
$O_{i,oct}$	1.05	0.68	0.33	−0.05	−0.46
	(0.08)	(0.05)	(0.01)	(0.01)	(0.01)
V_{Zn}	0.81	0.45	0.05		
	(0.03)	(0.02)	(0.06)		

Table 5.2: *Point defect formation volumes calculated within GGA+U in units of volume per formula unit ($V_D^f/\Omega_{f.u.}$). The errors of the extrapolation to infinite dilution are given in brackets.*

to about $-0.56\,\Omega_{f.u.}/e$ ($\Omega_{f.u.}$ denotes the volume per formula unit). In the case of V_{Zn}, $O_{i,db}$, $O_{i,rot-db}$, and $O_{i,oct}$ electrons are added and removed predominantly from oxygen-like orbitals, while for $Zn_{i,oct}$ zinc-like orbitals compensate most of the defect charge. In a simple picture the two different slopes are manifestations of the different spatial extents of the O and Zn-derived orbitals.

The oxygen vacancy behaves atypical because the local relaxation is different for the neutral and positive charge states. As explained in detail in Sec. 4.3.2 and Refs. [22, 23, 6], Zn atoms surrounding the vacancy site in neutral charge state relax *outward*, while they show an *inward* relaxation for positive charge states. The result is a non-linear charge state dependence of the formation volume.

5.5. Discussion

To begin with, the results of the GGA+U calculations are discussed. From the data in Tab. 4.1 the Fermi level dependence of the formation enthalpies (Fig. 4.3) and the stability map (Fig. 5.6) can be derived. In agreement with the calculations presented in the foregoing chapter three defects are found to be the most abundant: Under zinc-rich conditions the oxygen vacancy is the most likely defect for all Fermi levels; under oxygen-rich conditions

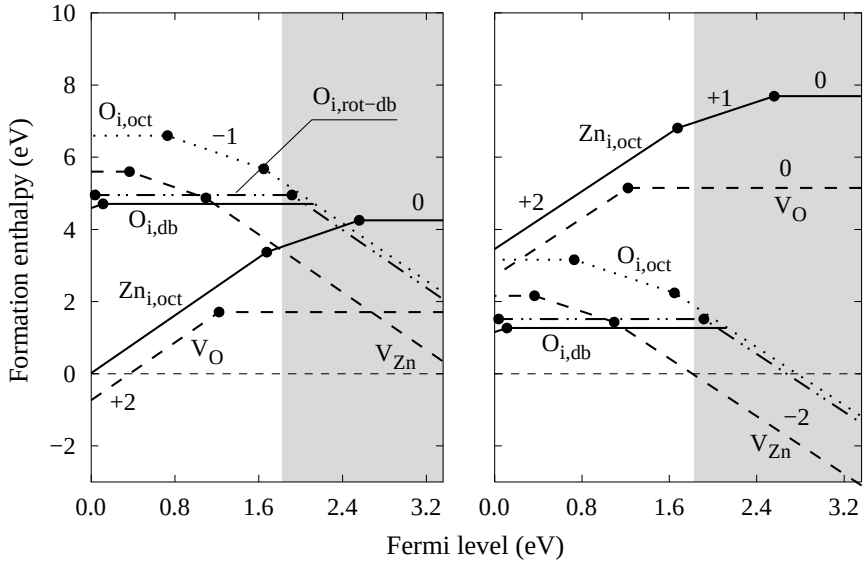

Figure 5.5.: *Variation of defect formation enthalpies with Fermi level under zinc (left) and oxygen-rich (right) conditions as obtained from GGA+U calculations. The grey shaded area indicates the difference between the calculated and the experimental band gap. The numbers in the plot indicate the defect charge state; parallel lines imply equal charge states. Open and closed circles correspond to defects on the zinc and oxygen sublattices, respectively.*

the zinc vacancy and oxygen interstitials are the dominant defect types. Earlier studies have consistently found the oxygen vacancy to be energetically slightly more favorable than the zinc interstitial. The present data imply that upon inclusion of volume relaxation this difference becomes yet larger ($\sim 0.7\,\mathrm{eV}$ at the valence band maximum). For the zinc interstitial as well as for the oxygen vacancy (equilibrium[§]) transition levels close to the calculated CBM are found.

The *oxygen vacancy* (V_O) shows a $2+/0$ transition 0.61 eV below the calculated CBM. This is in qualitative agreement with Zhang *et al.* [19] and Oba *et al.* [20] but contradicts the result by Kohan *et al.* who predicted the $2+/0$ transition of the oxygen vacancy in the vicinity of the VBM [18]. The deep level character (strong localization of defect electrons) correlates with the significant charge dependent structural changes described in Sec. 5.4.5 and Refs. [23, 22]).

[§]Janotti and Van de Walle [23] as well as Lany and Zunger [22] determined optical transition levels by employing the Franck-Condon principle.

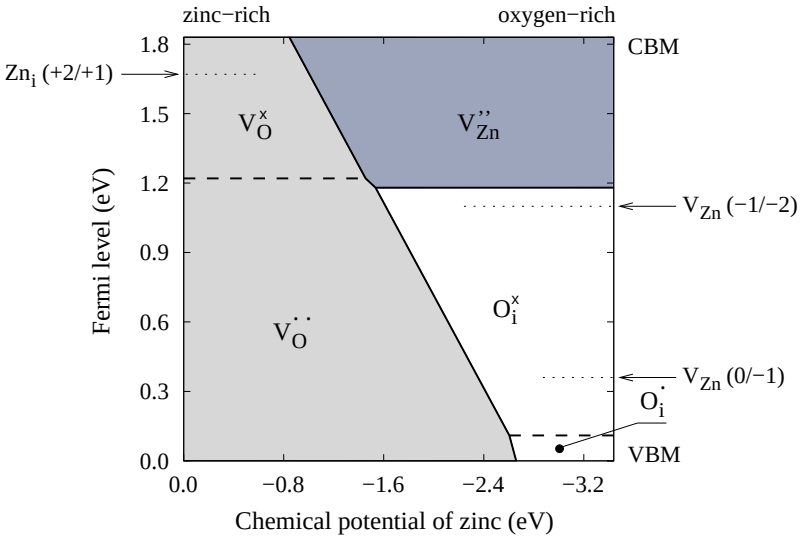

Figure 5.6: *Variation of dominant defect as a function of chemical potential and Fermi level as obtained from GGA+U calculations. In regions where the most stable defect is neutral, the transitions for the most stable charged defect are indicated by arrows and dotted lines.*

For the *zinc interstitial* (Zn_i) the present calculations locate the 2+/1+ transition level 0.15 eV below the CBM. In this case, the data by Kohan *et al.* show the same charge transition, while Zhang *et al.* and Oba *et al.* [19, 20] predict the 2+ charge state to be stable over the entire band gap. The structure of the zinc interstitial is similar in all charge states, indicative for a shallow defect level and in agreement with experimental observations [110].

For oxygen-rich conditions, oxygen dumbbell defects ($O_{i,db}$, $O_{i,rot-db}$) have the lowest formation enthalpies of all intrinsic point defects over the widest range of the (calculated) band gap confirming the results of the previous chapter (also compare Refs. [21, 6]). The GGA+U data clearly prove the existence of a $1 + /0$ transition level close to the VBM ($O_{i,db}$: 0.34 eV, $O_{i,rot-db}$: 0.02 eV above VBM). For the rotated dumbbell interstitial, the $0/2-$ transition lies at the CBM indicating very shallow acceptor behavior. The present data provides strong indication for ambipolar behavior as anticipated in Chapter 4.

The *zinc vacancy* (V_{Zn}) represents a good example for the importance of finite size sampling: supercell calculations with less than 108 atoms consistently predict the neutral charge state to be unstable with respect to the negative charge states. If supercell effects are, however, properly taken into account, it turns out that the formation enthalpy of the neutral zinc vacancy at the VBM is indeed lower than for the negative charge states. This results in two transitions. The first one ($0/1-$) lies very close to the VBM, the second one ($1 - /2-$) occurs near the middle of the calculated band gap.

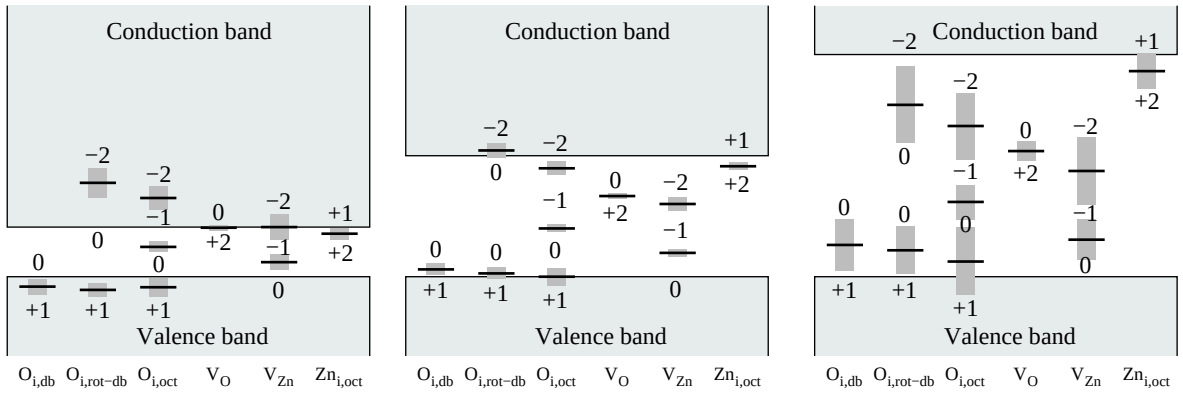

(a) GGA (b) GGA+U (c) extrapolation

Figure 5.7.: *Transition levels in the band gap calculated within GGA, GGA+U and using the extrapolation formula (5.3). The dark grey shaded areas indicate the error bars resulting from the errors given in Tab. 4.1.*

The zinc vacancy has the lowest formation enthalpy of all intrinsic point defects under oxygen-rich conditions for Fermi levels in the upper half of the band gap. Under these conditions, it is therefore the dominant acceptor confirming the experimental results of Tuomisto and coworkers [111]. By using positron annihilation spectroscopy in combination with isochronal annealing cycles on electron irradiated n-type samples, they furthermore obtained evidence for a second acceptor and suggested oxygen interstitials as likely candidates. From the present calculations this defect is identified as the rotated dumbbell interstitial ($\mathrm{O_{i,rot-db}}$).

Now the question is addressed to which extent the band gap underestimation within GGA+U affects the results. Although the band gap is significantly larger with GGA+U than with GGA, it is still smaller than the experimental value. In the past a variety of methods has been applied in order to correct for the DFT band gap error (see e.g., Refs. [18, 19, 22, 23, 112]; also compare Sec. 5.2). As pointed out by Lany and Zunger [22] these schemes lead to somewhat different results. In the present context, the extrapolation formula suggested by Janotti and Van de Walle [23] was applied. The transition level, ϵ^{ext}, corresponding to the experimental band gap, E_G^{exp}, is obtained from the transition levels calculated within GGA (ϵ^{GGA}) and GGA+U ($\epsilon^{\mathrm{GGA}+U}$) according to

$$\epsilon^{ext} = \frac{E_G^{exp} - E_G^{\mathrm{GGA}+U}}{E_G^{\mathrm{GGA}+U} - E_G^{\mathrm{GGA}}} \left(\epsilon^{\mathrm{GGA}+U} - \epsilon^{\mathrm{GGA}}\right) + \epsilon^{\mathrm{GGA}+U} \tag{5.3}$$

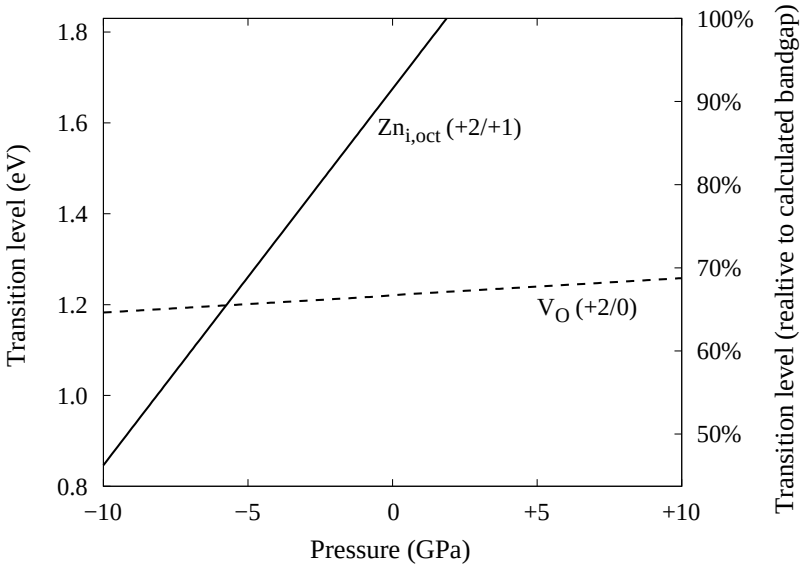

Figure 5.8: *Variation of equilibrium defect transition levels with isostatic pressure for the oxygen vacancy (2+/0) and the zinc interstitial (2+/1+).*

where E_G^{GGA} and $E_G^{\mathrm{GGA}+U}$ denote the GGA and GGA+U band gaps, respectively[¶]. The results of this extrapolation are shown in Fig. 5.7 in comparison with the GGA and GGA+U data. It is apparent that the extrapolated transition levels are very sensitive to the accuracy of the GGA and GGA+U data. Nonetheless, the qualitative classification of the defect levels as well as their hierarchy, which has been established above based on the GGA+U results, is preserved in the extrapolated data.

The formation volumes derived in Sec. 5.4.5 describe the first-order (linear) effect of pressure on the defect formation enthalpies. In combination with equation (5.2) they also allow to deduce the effect of isostatic pressure on the transition levels as exemplified for the oxygen vacancy and the zinc interstitial in Fig. 5.8. While the zinc interstitial transition level (2+/1+) shows a strong dependence on pressure, the oxygen vacancy 2+/0 level is hardly affected by pressure. The latter behavior is related to the changes in the relaxation behavior of the vacancy with charge state described above. The significant difference between the pressure dependence of the (equilibrium) transition levels for the two dominant donor defects ($\mathrm{V_O}$, $\mathrm{Zn_i}$) suggests that the controversy with regard to the

[¶]The underlying idea of the extrapolation scheme used by Janotti and Van de Walle [23] resembles the strategy suggested by Zhang *et al.* [80]: The calculated band gap is varied by changing some parameter of the calculation (Zhang *et al.* use the plane-wave cutoff energy, Janotti and Van de Walle use LDA and LDA+U). Finally, the formation enthalpies or transition energies corresponding to the full (experimental) band gap are obtained by extrapolating over the calculated band gap.

green luminescence center in ZnO [113, 114] could be resolved by performing pressure-dependent experiments.

In general, intrinsic point defects will be abundant in zinc oxide, since their formation enthalpies are very small. The resulting high defect concentrations probably do not only actively influence the electronic and optical, but to some extent also the mechanical properties. This could explain the large spread of experimental data for various material properties.

5.6. Conclusions

An extensive study of intrinsic point defects in zinc oxide has been performed in order to remedy the most significant approximations made in previous studies. To this end, a semi-empirical self-interaction correction scheme (GGA+U) has been applied to correct the position of the Zn-3d states and thereby the overestimation of covalency. As a consequence the band gap opens up significantly although it is still smaller than in experimentals. In order to remove the effects of elastic as well as electrostatic image forces, finite-size scaling has been employed which allowed to derive more precise formation enthalpies.

The present results mostly confirm earlier calculations (see Chapter 4 and Refs. [18, 19, 20, 21]) but predict a larger number of transition levels for intrinsic defects. Transition levels close to the conduction band minimum are identified for both the oxygen vacancy and the zinc interstitial. The zinc vacancy possesses a transition rather close to the VBM and another one roughly in the middle of the band gap. Oxygen interstitials show ambipolar behavior since they display transition levels near the valence band maximum and the conduction band minimum.

Defect formation volumes allow to deduce the pressure dependence of transition levels, which creates the possibility to distinguish experimentally e.g., the oxygen vacancy and zinc interstitial states.

6. Migration mechanisms and diffusion of intrinsic defects*

Density functional theory calculations in conjunction with the climbing image nudged elastic band method were performed in order to study the self-diffusion of oxygen and zinc in zinc oxide. To this end, the complete set of migration paths for vacancies as well as interstitials in wurtzite crystals was derived and expressions were deduced, which provide the link to experimentally accessible tracer diffusion coefficients. The calculated migration barriers are consistent with annealing experiments on irradiated samples. Oxygen and zinc interstitials are mobile down to temperatures of 80 to 110 K accounting for the rapid annihilation of defects observed after electron irradiation. For oxygen self-diffusion vacancy and interstitialcy mechanisms are found to dominate under zinc and oxygen-rich conditions, respectively. This refutes the belief that vacancy mechanisms can be operational in oxygen self-diffusion experiments in oxygen-rich atmosphere. For predominantly oxygen-rich and n-type conducting conditions zinc self-diffusion occurs via a vacancy mechanism. The present results provide the basis for the (re-)interpretation of diffusion experiments, and pave the way towards the development of continuum models for device simulation.

6.1. Introduction

The mobilities of intrinsic point defects determine the annealing behavior of materials. Moreover, diffusion pertains to the degradation of ZnO varistors, which is believed to occur via the migration of interstitials to grain boundary regions [27, 28, 29, 30]. Fur-

*Parts of the present chapter have been published in Refs. [3] and [5].

thermore, the annealing of defects by rapid defect migration is likely to contribute to the remarkable radiation hardness of zinc oxide [31]. Knowledge of diffusivities and diffusion mechanisms is obviously instrumental in order to obtain a fundamental understanding of these processes, to devise strategies for controlling the migration of certain species, and to develop continuum models for device simulation.

Diffusion experiments provide information on atomic migration and in addition allow to gain insights into the defect chemistry in general [115]. The interpretation of diffusion experiments is, however, often difficult and evidence for defect properties is indirect. In the past several experimental studies have been concerned with the determination of self-diffusion coefficients [116, 117, 118, 119, 120, 121], but the data scatter is large and no consensus on activation energies, exponential pre-factors, or migration mechanisms has been achieved. Therefore, a systematic theoretical investigation is highly desirable in order to obtain more fundamental insights on the subject. Hitherto, theoretical investigations based on quantum-mechanical calculations have been conducted to explore static properties of intrinsic as well as extrinsic point defects in zinc oxide (see e.g., Refs. [18, 19, 20, 21, 22, 23, 6, 122]). Recently, migration barriers were calculated for Li in wurtzitic ZnO [122] and for the doubly positively charged zinc interstitial in cubic ZnO (zinc blende structure) [123] but at present there is no comprehensive study on the mobilities of intrinsic point defects in zinc oxide.

In order to determine migration paths and barriers for vacancy and interstitial motion in zinc oxide, density functional theory (DFT) calculations in conjunction with the climbing image nudged elastic band method (CI-NEB) were performed [124, 125]. The complete set of migration paths to first and second nearest neighbors on the respective sublattice has been derived for the wurtzite lattice taking into account the non-ideal axial ratio of ZnO as well as defect induced symmetry breaking. By using the CI-NEB method, a minimal number of constraints was imposed when searching for saddle points. Unlike experiments which provide only a compound value for the diffusivity, the present approach allows to separate unequivocally the various contributions to the diffusivity. Since only isolated intrinsic point defects are considered, association of defects, in particular with impurities [21, 83, 122], is not included in the present study.

In the next section, the equations describing diffusion in terms of attempt frequencies and migration barriers are summarized. Section 6.3 describes the computational framework and

discusses potential sources of errors. The migration paths and the self-diffusion of oxygen and zinc are treated in Sec. 6.4 and Sec. 6.5, respectively.

6.2. Background

The rate at which a single isolated point defect d moves via migration path i can usually be described by an Arrhenius law [115]

$$\Gamma_i^d = \Gamma_{0,i} \exp\left[-\Delta G_i^m / k_B T\right]. \tag{6.1}$$

In principle, the attempt frequency ($\Gamma_{0,i}$) can be obtained within harmonic transition-state theory via the Vineyard equation [126] but it is frequently approximated by a characteristic frequency such as the lowest Raman mode [119], the Einstein or the Debye frequency. The free enthalpy of migration (ΔG_i^m) is given by

$$\Delta G_i^m = \Delta H_i^m + p\Delta V_i^m - T\Delta S_i^m \tag{6.2}$$

where ΔH_i^m is the enthalpy of migration (ΔV_i^m) is the migration volume and ΔS_i^m denotes the migration entropy. For small pressures, the pressure-volume term approaches zero, and can be disregarded. The entropy term enters the pre-factor. Since migration entropies are usually in the range of 1 to $2k_B$, this, however, constitutes merely a minor effect (compare Sec. 4.2.2). Entropic contributions were therefore neglected in the present work. The factor which most crucially affects the jump rate (and eventually the diffusion rate) is the migration enthalpy (ΔH_i^m). Its determination for different defects, migration paths, and charge states is subject of the present chapter.

6.3. Methodology

6.3.1. Saddle point finding

The thermodynamic properties of a system are determined by the distribution and the energy differences between the local minima on the potential energy surface (PES). Similarly, the kinetics are governed by the distribution of the paths connecting the local minima and the respective barrier heights. The relevant quantities are schematically depicted for a one-dimensional PES in Fig. 6.1.

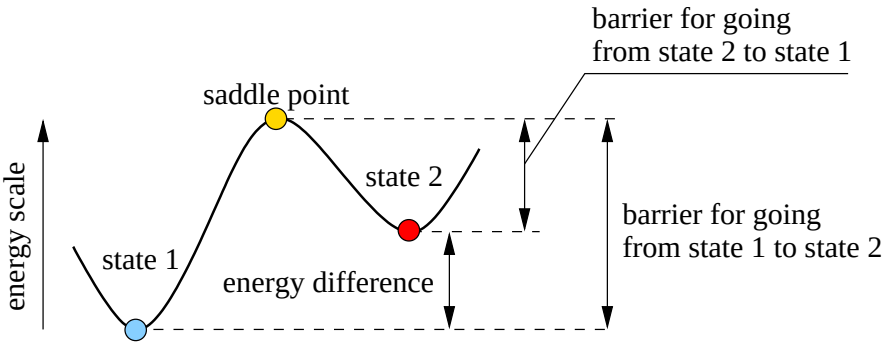

Figure 6.1: *Schematic of a one-dimensional potential energy surface.*

Local minima can usually be found with comparably small computational effort using e.g., conjugated gradients minimization, Monte-Carlo techniques or simulated annealing. The identification of minimum energy paths (MEP) and thus energy barriers constitutes a more difficult task. The problem is equivalent to finding the saddle points of the PES, i.e. two criteria must be satisfied[†] (1) $\nabla_{\boldsymbol{R}} E = 0$ and (2) at least one of the eigenvalues of the Hesse matrix $\Delta_{\boldsymbol{R}} E$ must be negative. Since the evaluation of second derivatives is computationally very demanding, a number of techniques such as the dimer, the nudged elastic band (NEB) method or the Lanczos method have been developed which require evaluation of first derivatives only [124, 127].

In the nudged elastic band (NEB) method [124] a number of images are distributed between the initial (e.g., vacancy on site A) and the final state (e.g., vacancy on site B) of the system. The images are connected via elastic springs. A numerical algorithm (e.g., conjugated gradients or damped molecular dynamics) is used to minimize the forces on the images taking into account the action of the springs. Upon optimization, the chain of images successively moves towards the nearest MEP. The situation is schematically shown for a two-dimensional PES in Fig. 6.2(a). The space, in which the actual minimization is carried out, is $3N$-dimensional where N is the number of atoms in the system. The climbing image NEB (CI-NEB) scheme is an extension of the standard NEB method [124, 125]. Firstly, the image with the highest energy is selected. Then the force along the direction of the two neighboring images is projected out and inverted. Eventually, all forces are minimized. When convergence is achieved, the climbing image is located at the saddle point.

[†]The energy is derived with respect to the vector $\boldsymbol{R} = \{\boldsymbol{r}_1, \boldsymbol{r}_2 \ldots \boldsymbol{r}_N\}$ ($\boldsymbol{R} \in \mathbb{R}^{3N}$) where $\boldsymbol{r}_i$ is the coordinate vector of particle i.

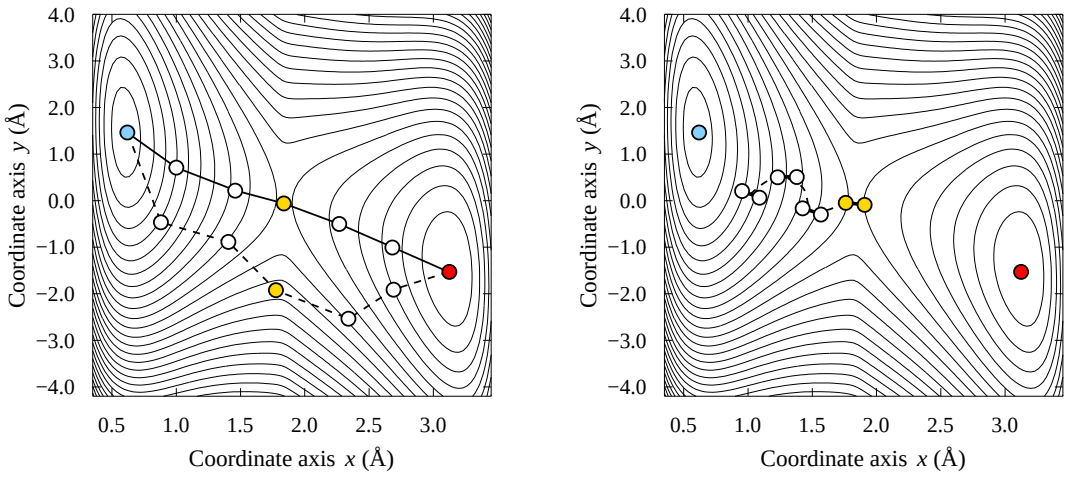

(a) Nudged-elastic band (NEB) method

(b) Dimer method

Figure 6.2.: *Schematic of a two-dimensional potential energy surface illustrating (a) the NEB/CI-NEB and (b) the dimer method. The blue and red circles mark the initial and final state respectively. (a) The dashed and solid lines show the NEB at the beginning and the end of the optimization. The white circles mark intermediate images of the system. The yellow circles indicate the climbing image which is the replica with the highest energy and which eventually is located at the saddle point. (b) The line connects successive configurations along the path connecting the two minima. The final configuration which corresponds to the saddle point is labeled yellow.*

The dimer method [128] is applicable also if the final state of the system is unknown. It employs two replicas of the system which are displaced with respect to each other by some small distance[‡]. In order to find the nearest saddle point the dimer is moved uphill on the PES. Concurrently, it is rotated in order to line up with the lowest curvature mode at the point of the PES where it is currently located. When the drag force on the dimer vanishes, a saddle point has been reached. The search strategy is schematically shown for a two-dimensional PES in Fig. 6.2(b).

6.3.2. Computational method

Calculations within density functional theory (DFT) were carried out with the Vienna ab-initio simulation package (VASP) [103] using the projector-augmented wave (PAW) method [62, 104] and the generalized gradient approximation (GGA) in the parameterization by Perdew and Wang (PW91) [25]. In order to properly account for the position of the Zn-

[‡]Typically, the distance between the two replicas is about $\| \boldsymbol{R}_1 - \boldsymbol{R}_2 \| \approx 0.1\,\text{Å}$.

3*d* levels the GGA+*U* scheme in the formulation by Dudarev *et al.* [54] was adopted as described in detail in the foregoing chapter. Hexagonal 32-atom supercells were employed equivalent to $2 \times 2 \times 2$ primitive unit cells. The plane-wave energy cutoff was set to 500 eV and a Γ-point centered $2 \times 2 \times 2$ k-point grid was used for Brillouin zone sampling. A discussion of the potential sources of errors is given in the appendix.

6.3.3. Determination of diffusion paths

The wurtzite lattice is composed of two interpenetrating hexagonal close packed (hcp) lattices occupied by zinc and oxygen atoms, respectively. It follows that the diffusion paths for oxygen (V_O) and zinc vacancies (V_O) can be deduced from the diffusion paths available on the hcp lattice; similarly this applies for oxygen interstitials (O_i) which adopt dumbbell-like ground state configurations (see chapter 4 and Refs. [21, 6]). The migration paths for the zinc interstitial (Zn_i) are based on the simple hexagonal lattice formed by the ideal octahedral interstitial sites. Since previous studies [18, 19, 20] consistently found that antisites have extremely high formation energies, antisite mediated diffusion mechanisms can be safely ruled out and were not considered.

In order to obtain the energy barriers for the various diffusion paths the climbing image nudged elastic band (CI-NEB) method [124, 125] was employed as implemented for VASP by Henkelman, Jónsson and others [129]. The convergence of the minimum energy path (MEP) and the saddle point was checked by using up to eight images. As the saddle point determination worked already reliably for a small number of images, for most computations only three or four images were used. The images of the NEB were relaxed until the maximum residual force was less than 15 meV/Å. For several configurations the saddle points were confirmed by performing dimer calculations [128] at a higher level of convergence. The differences between the CI-NEB and the dimer saddle point energies amounted to about 1 meV and less, which confirms the reliability of the CI-NEB approach.

Since the defect charge states vary with the electron chemical potential due to the explicit Fermi energy dependence of the formation enthalpies (see equation (4.8)), the migration barriers have to be determined independently for all relevant charge states (V_O: $0 \leq q \leq +2$; O_i: $-2 \leq q \leq +2$; V_{Zn}: $-2 \leq q \leq 0$; Zn_i: $0 \leq q \leq +2$).

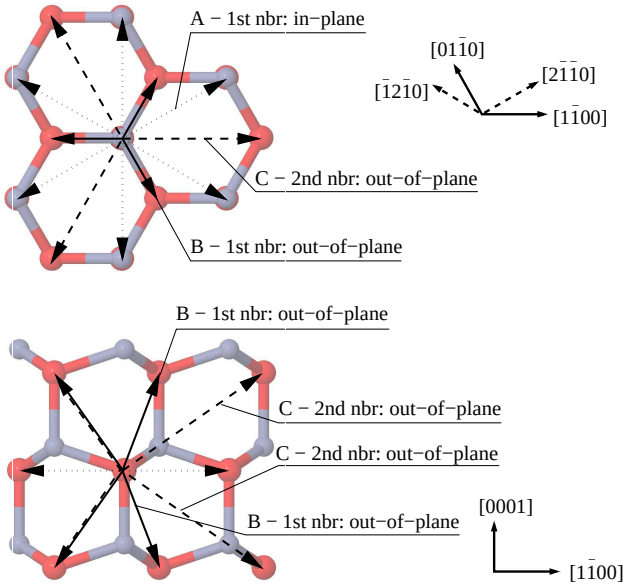

Figure 6.3: *Diffusion paths accessible to oxygen (zinc) vacancies on the wurtzite lattice via jumps to first or second nearest oxygen (zinc) sites. Projections along* [0001] *(top) and* [11$\bar{2}$0] *(bottom).*

6.4. Oxygen

6.4.1. Migration paths

Vacancy diffusion

The possible diffusion paths via first as well as second nearest oxygen neighbors are schematically shown in Fig. 6.3. Among the jumps to first nearest oxygen sites, there are six symmetry equivalent paths in the (0001) plane (A, 1st nbr: in-plane) and six equivalent paths with components parallel to the [0001] axis (B, 1st nbr: out-of-plane). On an ideal hcp-lattice ($c/a = \sqrt{8/3} = 1.633$) these two paths are equivalent. In the present case they are, however, distinct, since the axial ratio of the oxygen hcp-lattice is slightly smaller than ideal ($c/a = 1.611$). Considering jumps to second nearest oxygen sites, another six symmetry equivalent possibilities for upward and downward motion are obtained (C, 2nd nbr: out-of-plane). Both out-of-plane paths also lead to in-plane displacements of the migrating atom.

The calculated diffusion barriers are compiled in Tab. 6.1 and Fig. 6.4 shows a typical energy pathway. The migration enthalpies for first-nearest neighbor migration display a rather diverse behavior. In the neutral charge state the in-plane migration barrier is 0.5 eV lower than its out-of-plane counterpart indicating anisotropic diffusion behavior. On the other hand, since for the 2+ charge state process B possesses the lowest barrier, taking

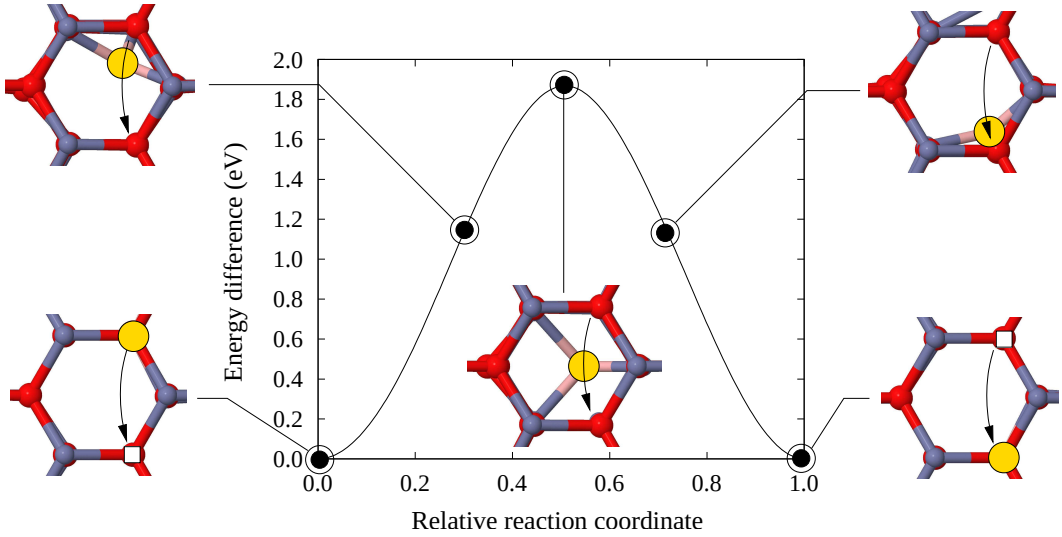

Figure 6.4.: *Energy pathway for oxygen vacancy migration via in-plane path A. The large yellow circles symbolize the moving oxygen atom, the small white squares indicate the initial and final position of the vacancy. Projections along [0001].*

into account the displacements parallel and perpendicular to the [0001] axis the diffusivity should display isotropic behavior (also compare equations (6.7) and (6.8). The charge state 1+ represents an intermediate case.

Interstitial diffusion

There are at least three oxygen interstitial configurations which have been identified as local minima of the energy hypersurface based on DFT calculations (see Chapter 4 and Ref. [6]). In equilibrium oxygen interstitials adopt the dumbbell ($O_{i,db}$) or the rotated dumbbell ($O_{i,rot-db}$) configuration. The highly symmetric octahedral interstitial ($O_{i,oct}$) is energetically unfavorable as a ground state configuration, but it can occur as an intermediate state along the diffusion path as will be discussed below.

The two dumbbell configurations ($O_{i,db}$ and $O_{i,rot-db}$) possess a threefold symmetry axis, i.e. rotations about the [0001]-axis by multiples of 120° generate symmetry equivalent copies of the original defect. Furthermore (ignoring small differences in the atomic relaxations), the $O_{i,db}$ and $O_{i,rot-db}$ can be transformed into each other by application of a sixfold mirror axis (6_m). In the following, this "on-site" transformation is referred to as process X.

Table 6.1.: *Energy barriers for vacancy and interstitial mediated migration of oxygen in units of eV as obtained from CI-NEB calculations. The formation enthalpies of the respective ground state configurations obtained in Chapter 5 are included for reference (zinc-rich conditions, Fermi level at valence band maximum). See Figs. 6.3 and 6.5 for definition of migration paths.*

Migration path			**Charge state**				
			$q=+2$	$q=+1$	$q=0$	$q=-1$	$q=-2$
Oxygen vacancy, V_O							
1st nbr: in-plane	A		1.49	1.37	1.87		
1st nbr: out-of-plane	B		1.09	1.38	2.55		
2nd nbr: out-of-plane	C		3.62	3.79	4.29		
formation enthalpy			−0.73	0.71	1.71		
Oxygen interstitial, O_i							
1st nbr: in-plane	A_1	$O_{i,db} \leftrightarrow O_{i,db}$	1.34	1.25	1.09	–	–
1st nbr: in-plane	A_2	$O_{i,rot-db} \leftrightarrow O_{i,rot-db}$	1.03	0.98	0.95	0.23	0.40
1st nbr: out-of-plane	B_1	$O_{i,db} \leftrightarrow O_{i,rot-db}$	1.23	1.09	0.81	0.43	0.88
1st nbr: out-of-plane	B_2	$O_{i,db} \leftrightarrow O_{i,rot-db}$	1.23	1.09	0.81	0.43	0.88
2nd nbr: out-of-plane	C	$O_{i,db} \leftrightarrow O_{i,rot-db}$	1.98	1.78	1.60	0.60	1.37
ground state (gs)				$O_{i,db}$		$O_{i,rot-db}$	
formation enthalpy			5.08	4.59	4.70	7.08	8.79
energy difference	gs → $O_{i,db}$/$O_{i,rot-db}$		+0.29	+0.25	+0.15	+0.48	+0.78
energy difference	gs → $O_{i,oct}$		+1.44	+1.33	+1.10	+0.14	+0.30

While in neutral and positive charge states the two oxygen atoms are bonded, they adopt a *split-interstitial* configuration in negative charge states (see Sec. 4.3.2 and Ref. [6]). In spite of this difference, the migration paths can be described on a similar basis for all charge states. Invoking the symmetry of the lattice the following mechanisms for oxygen interstitial migration can be distinguished, which are illustrated in detail in Fig. 6.5(a-c).

(a) *in-plane movement* – processes A_1 and A_2

In process A_1 one of the atoms of a dumbbell interstitial ($O_{i,db}$) moves away from its partner and forms a new dumbbell with one of the two nearest oxygen atoms. Because of the threefold symmetry axis of the dumbbell there are three dumbbell orientations per oxygen site with two possible "target" atoms each, such that all of the six nearest in-plane neighbors on the hcp oxygen lattice can be reached. Process A_2 is the equivalent migration path for a rotated dumbbell interstitial.

(b) *out-of-plane movement* – processes B_1 and B_2

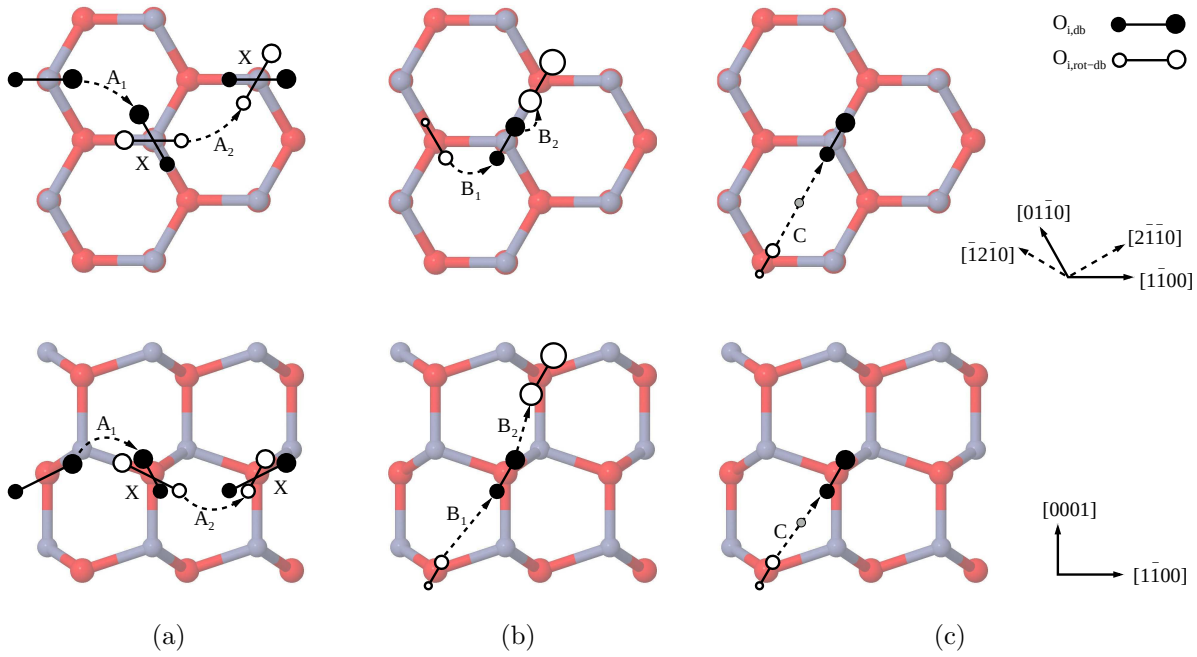

Figure 6.5.: *Diffusion paths accessible to oxygen interstitials on the wurtzite lattice via jumps to first or second nearest neighbor sites. Panels (a) and (b) show in-plane and out-of-plane diffusion paths to first nearest oxygen neighbors, panel (c) illustrates out-of-plane diffusion via second nearest oxygen neighbors. The size of the spheres scales with the position of the atom along the* [0001]*-axis.*

In both processes one of the atoms in the dumbbell (rotated dumbbell) moves to one of the first nearest out-of-plane neighbors forming a rotated dumbbell (dumbbell) interstitial at the new site.

(c) *out-of-plane movement* – process C

This process is similar to processes B_1 and B_2, but the interstitial migrates via jumps to second nearest oxygen neighbors thereby bridging larger distances in the lattice. The moving atom traverses through the octahedral interstitial configuration as indicated in Fig. 6.5(c) by the small grey spheres.

Equivalent to processes B and C for vacancy migration, all of the out-of-plane migration paths (processes B_1, B_2, C) involve in-plane displacements as well. The concatenation of these processes leads to the migration of oxygen via an interstitialcy mechanism.

For the on-site transformation (process X), activation energies smaller than 0.1 eV are obtained (with respect to the configuration which is higher in energy). Since all other energy barriers in the system are at least by a factor of two larger (compare Tab. 6.1), this

process should never be rate-determining and is not considered any further. The energy barriers for the remaining migration processes are compiled in Tab. 6.1. For the (out-of-plane) processes B_1, B_2 and C, which implicitly transform between the two dumbbell states, only the barrier from the respective ground state configuration is given ($O_{i,db}$ for $q = 0, +1, +2$ and $O_{i,rot-db}$ for $q = -1, -2$).

As shown in Fig. 6.6, all processes show comparable trends with charge state. Going from charge state 2+ to charge state 0 the barriers decrease slightly. A sudden drop occurs as the charge state becomes negative but the barriers rise again as yet another electron is added to the system ($q = -2$). For all paths the barriers are minimal for a charge state of 1−.

The significantly lower migration barriers for oxygen interstitial migration in negative charge states can be rationalized based on the analysis of oxygen interstitial configurations given in Chapter 4. In neutral and positive charge states, the ground state configuration is stabilized by the formation of a strong oxygen–oxygen bond. When the system is negatively charged, it is favorable to split this bond and to adopt a configuration in which the oxygen atoms are relatively far apart (compare Sec. 4.3.2). Migration of oxygen interstitials in neutral or positive charge states thus requires breaking the strong oxygen–oxygen bond. On the other hand, for negative charge states motion of oxygen interstitials can be accomplished by breaking and reforming a minimal set of bonds leading to significantly lower migration barriers.

The energy surface for oxygen interstitial migration possesses many local minima ($O_{i,db}$, $O_{i,rot-db}$, $O_{i,oct}$) and saddle points, and is also quite flat in some regions (compare e.g., the "on-site" transformation process X). As a result, the minimum energy paths are rather complex, which is schematically depicted in Fig. 6.7 for the charge states $q = +2$, 0, and -2.

The in-plane migration paths A_1 and A_2 possess simple saddle points. For the neutral and positive charge states, they are almost identical if the energy difference between the dumbbell ($O_{i,db}$) and rotated dumbbell ($O_{i,rot-db}$) is taken into account (compare Fig. 6.6). The saddle point is close in energy to the octahedral interstitial which is plausible considering Fig. 6.5(a). For the negative charge states, the migration barrier A_2 is very low and the saddle point configuration is again very close to the octahedral interstitial configuration. Since the energy barrier for process A_2 is lower than the energy difference between $O_{i,rot-db}$ and $O_{i,db}$, the path A_1 becomes redundant.

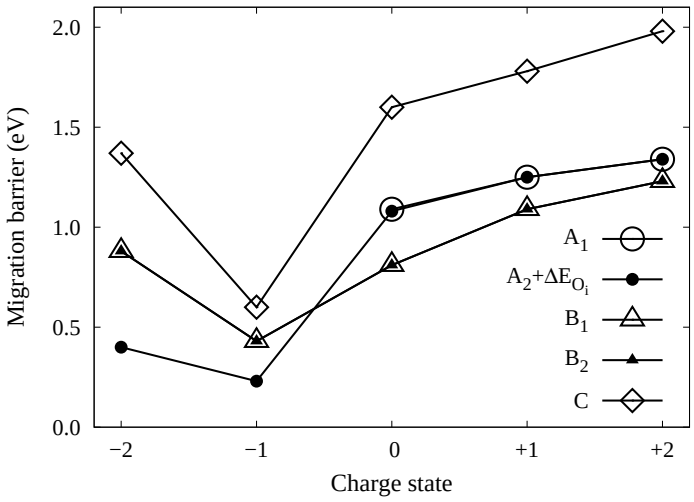

Figure 6.6: *Charge state dependence of oxygen interstitial migration enthalpies. For the in-plane path A_2, the energy difference ($\Delta E_{\mathrm{O_i}}$) between the dumbbell ($\mathrm{O_{i,db}}$) and rotated dumbbell ($\mathrm{O_{i,rot-db}}$) configurations has been included (compare Fig. 6.7).*

The out-of-plane paths B_1 and B_2 yield practically identical saddle points. For the negative charge states the saddle point for the transformation of $\mathrm{O_{i,rot-db}}$ into $\mathrm{O_{i,db}}$ is found to coincide almost exactly with the (regular) dumbbell ($\mathrm{O_{i,db}}$) configuration. Thus, the barrier for the migration of $\mathrm{O_{i,rot-db}}$ is essentially given by the energy difference between $\mathrm{O_{i,rot-db}}$ and $\mathrm{O_{i,db}}$.

The most complex minimum energy path is observed for the migration along path C. For all charge states the octahedral interstitial occurs as an intermediate state as indicated in Fig. 6.5. While the charge state is changing from 2+ to 2− the depth of the local minimum associated with the octahedral interstitial changes from 0.01 eV ($q = +2$) to 0.90 eV ($q = -2$). At the same time the local minimum corresponding to the rotated dumbbell ($q \geq 0$) and dumbbell ($q < 0$) states, respectively, becomes more and more shallow. Actually, in order to deal properly with these features of the energy surface, one would need to describe the migration process C in negative charge states similar to a reaction with pre-equilibrium. Since the barriers for the alternative processes (A_1, A_2, B_1, and B_2), have lower barriers, they will, however, be rate-determining and the additional complexity arising for path C can be safely neglected. Thus, only the maximum barrier heights were compared for the latter case (see Tab. 6.1).

In summary, a migrating oxygen atom can move through a series of single jumps with in-plane as well as out-of-plane components of the displacement vector. Since in neutral and positive charge states the migration enthalpies for in and out-of-plane paths are very similar, a nearly isotropic behavior would be expected. On the other hand, for the negative

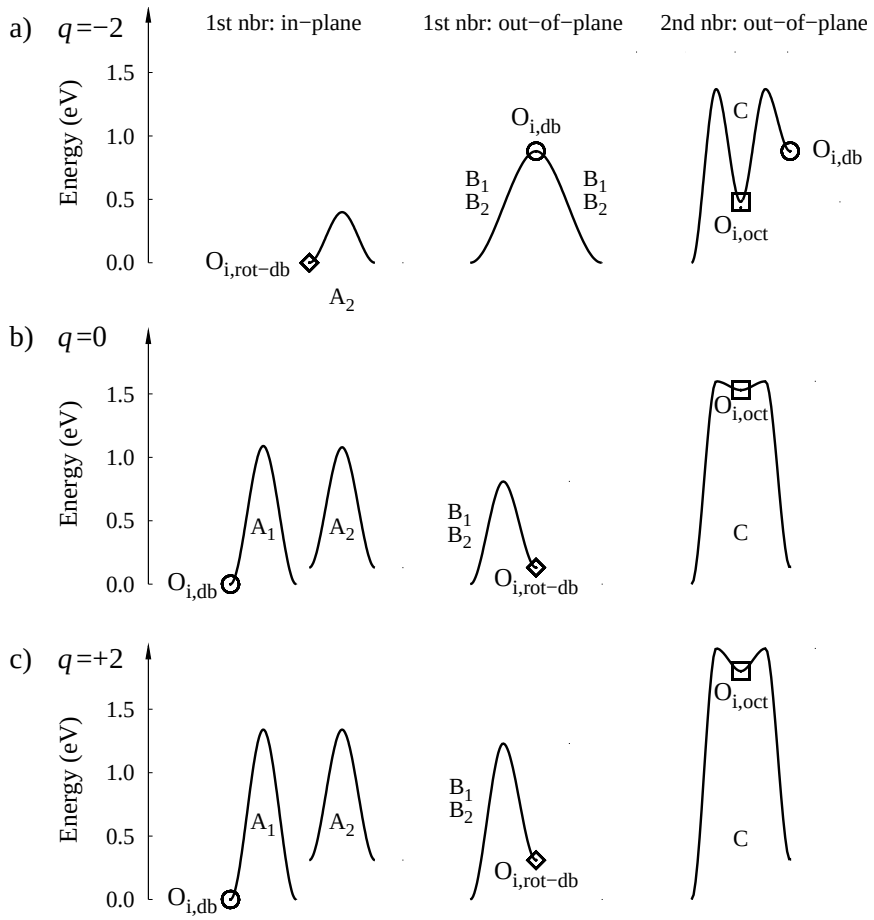

Figure 6.7.: *Schematic of the energy surface for oxygen interstitial migration for charge states $q = -2$ (a), $q = 0$ (b), and $q = +2$ (c). The zero of the energy scale corresponds to the respective ground state ($q \geq 0$: $\mathrm{O_{i,db}}$, $q < 0$: $\mathrm{O_{i,rot-db}}$). The energetically higher-lying states can transform into the ground state via the on-site transformation process X (not shown) which has a very small barrier.*

charge states the in-plane path $\mathrm{A_1}$ is significantly lower in energy than the two lowest out-of-plane paths ($\mathrm{B_1}$, $\mathrm{B_2}$), which should give rise to anisotropic diffusion.

Comparison with experiment

Annealing measurements after electron [130, 31] as well as ion irradiation [131] have shown that the onset of significant recovery occurs between 80 and 130 K which has been taken as evidence for host interstitial migration [130]. In fact, the oxygen interstitial diffusion barriers for charge states $q = -1$ and -2 are small enough to allow defect diffusion at such low temperatures. Assuming a typical annealing time of 10 min, and requiring a mean

square displacement between $(100\,\mathrm{nm})^2$ and $(1000\,\mathrm{nm})^2$, threshold temperatures[§] between 80 and 100 K are obtained for charge state $q = -1$, and between 130 and 160 K for charge state $q = -2$ in good agreement with experiment. The other charge states should not contribute to annealing at temperatures less than 350 K.

Using positron annihilation spectroscopy in combination with electron irradiation of n-type zinc oxide samples, Tuomisto *et al.* were able to deduce an activation energy for the neutral oxygen vacancy of $1.8 \pm 0.1\,\mathrm{eV}$ [132]. Again, the calculations are consistent with this observation giving a minimum barrier of 1.87 eV (process A, Tab. 6.1).

6.4.2. Diffusivities

Derivation of diffusivities

If all migration barriers are known, the defect diffusivity is obtained by a summation over the available paths

$$D^d = \frac{1}{2} \sum_i \zeta_i \Gamma_i^d |\boldsymbol{\lambda}_i|^2 \tag{6.3}$$

where $|\boldsymbol{\lambda}_i|$ is the jump length, ζ_i is the multiplicity (as given in Tab. 6.1), and the jump rate, Γ_i^d, is given by equation (6.1). By projecting the displacement vector ($\boldsymbol{\lambda}_i$) onto special lattice directions the components of the diffusivity tensor can be obtained. Due to the symmetry of the wurtzite lattice, there are only two independent components, which are conventionally denoted $D_\perp$ and $D_\parallel$ for diffusion perpendicular and parallel to the [0001] axis, respectively.

Experimentally, diffusivities are usually obtained by measuring the mobility of tracer atoms. Considering the vacancy and interstitialcy mechanisms, which have been introduced in the foregoing section, a tracer atom can only migrate if a vacancy or interstitial defect is available in its neighborhood. Therefore, the tracer diffusivity (or self-diffusion coefficient), D^*, depends on the diffusivities of vacancies, D^v, and interstitials, D^i, as well as on the respective concentrations, c^v and c^i, according to

$$D^* = f^v Z^v c^v D^v + f^i Z^i c^i D^i \tag{6.4}$$

[§]In order for a defect to anneal it must be able to migrate a certain distance $\sqrt{\langle r^2 \rangle_{min}}$ during the annealing time (τ). Using the Einstein relation, $\langle r^2 \rangle = 6D\tau$, the onset temperature for annealing is established as the temperature for which $6D\tau$ exceeds $\sqrt{\langle r^2 \rangle_{min}}$.

where f^v and f^i are lattice dependent correlation factors typically of order unity, and Z^v and Z^i are the number of possible target sites. The exact determination of the correlation factors is a subject in its own right [115]; in the present context the approximation $f^{v,i} = 1 - 1/Z^{v,i}$ is used. Because the wurtzite lattice is composed of two interpenetrating hexagonal close packed sublattices, the coordination numbers are $Z^v = Z^i = 12$. Since either interstitials or vacancies prevail under oxygen and zinc-rich conditions, respectively, one of the two terms in equation (6.4) is usually dominating. Therefore, it is admissible and instructive to discuss the vacancy and interstitialcy mechanism as well as the charge states separately.

In case of an intrinsic mechanism, the defect concentrations are determined by the thermodynamic equilibrium conditions and follow an Arrhenius law behavior,

$$c^d = c_0^d \exp\left[-\Delta G_d^f / k_B T\right] \tag{6.5}$$

which, if entropic contributions are neglected, can be approximated by

$$c^d \approx c_0^d \exp\left[-\Delta H_d^f / k_B T\right] \tag{6.6}$$

where ΔH_d^f is the defect formation enthalpy. Therefore, in case of an intrinsic mechanism the activation energy measured in a diffusion experiment comprises both the formation (ΔH^f) and the migration enthalpy (ΔH^m). In contrast, in case of an extrinsic mechanism, the defect concentrations (c^v or c^i) are externally controlled e.g., through intentional or unintentional doping and therefore, the activation energy contains only the migration barrier.

It is expedient to discuss the parameters which influence the tracer diffusion coefficient in the presence of an intrinsic diffusion mechanism. Apart from the obvious temperature dependence, D^* is affected by (*i*) the chemical potential (i.e., the partial pressures of Zn and O) and (*ii*) the Fermi level: (*i*) Since the formation enthalpies in equation (6.6) depend linearly on the chemical potential [77], according to equation (6.4) the tracer diffusion coefficient will vary as well. Neither the migration barriers (ΔH_i^m) nor the attempt frequencies ($\Gamma_{0,i}$) are explicit functions of the chemical potential. (*ii*) The formation enthalpies of charged defects also change linearly with the Fermi level (compare equation (4.8)), again affecting the tracer diffusion coefficient through equations (6.4) and (6.6). In addition, the diffusion coefficient depends implicitly on the Fermi level, since it determines which charge state of a given defect is the most stable and thus which migration barrier is relevant.

Table 6.2: *Multiplicities (ζ_i) and displacements (λ; compare equation (6.3)), for vacancy and interstitial migration as they enter the calculation of diffusivities via equation (6.3). $\lambda_\perp$: displacement within (0001) plane in units of a; $\lambda_\parallel$: displacement parallel to [0001] axis in units of c (a and c are the lattice constants of the wurtzite structure).*

Migration path	$\boldsymbol{\zeta_i}$	$\boldsymbol{\lambda_\perp}$	$\boldsymbol{\lambda_\parallel}$
Oxygen vacancy, V_O			
1st nbr: in-plane (A)	6	1	0
1st nbr: out-of-plane (B)	6	$\sqrt{1/3}$	1/2
2nd nbr: out-of-plane (C)	6	$\sqrt{4/3}$	1/2
Oxygen interstitial, O_i**, neutral and positive**			
1st nbr: in-plane (A_1, A_2)	6	1	0
1st nbr: out-of-plane (B_1, B_2)	6	$\sqrt{1/3}$	1/2
2nd nbr: out-of-plane (C)	6	$\sqrt{4/3}$	1/2
Oxygen interstitial, O_i**, negative charge states**			
1st nbr: in-plane (A_2)	6	1	0
1st nbr: out-of-plane (B_1+X, B_2+X)	3	$\sqrt{1/3}$	1/2
1st nbr: in-plane (B_1+B_1)	6	1	0
1st nbr: out-of-plane (B_1+B_2, B_2+B_1)	6	1	1

In summary, in the case of an intrinsic mechanism, the dependence of the self-diffusion coefficient on the chemical potential as well as the Fermi level originates predominantly from the dependence on the defect concentration. In contrast, in the case of an extrinsic mechanism, the dependence on chemical potential and Fermi level should be significantly less pronounced.

Using equations (6.1–6.6) and the parameters given in Tab. 6.2, one arrives at the following expressions for the diffusivity tensor components for the oxygen vacancy ($\beta = 1/k_B T$)

$$D_\perp = \frac{1}{2}\Gamma_0 a^2 \left[3e^{-\beta\Delta E_\mathrm{A}} + e^{-\beta\Delta E_\mathrm{B}} + 4e^{-\beta\Delta E_\mathrm{C}}\right] \tag{6.7}$$

$$D_\parallel = \frac{3}{4}\Gamma_0 c^2 \left[e^{-\beta\Delta E_\mathrm{B}} + e^{-\beta\Delta E_\mathrm{C}}\right]. \tag{6.8}$$

In the case of the oxygen interstitial, positive and negative charge states need to be separated. For neutral and positively charged interstitials, the small energy difference ($\Delta E_{\mathrm{O_i}}$) between the dumbbell ($\mathrm{O_{i,db}}$) and rotated dumbbell ($\mathrm{O_{i,rot-db}}$) configurations allows the assumption that both types contribute to diffusion. The resulting migration paths are shown in Fig. 6.5; the according multiplicities and displacements are given in Tab. 6.2.

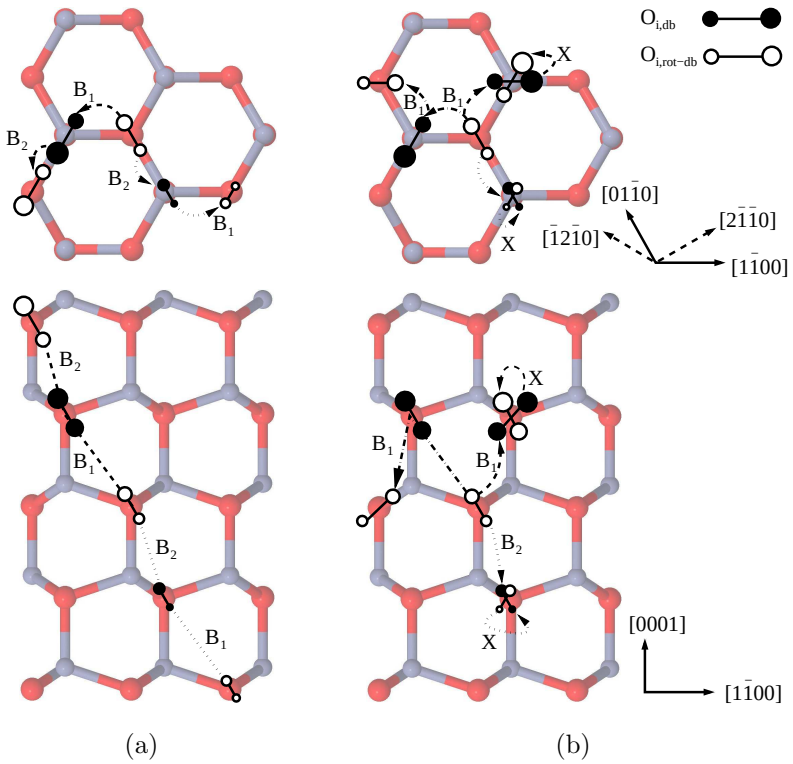

Figure 6.8: *Modified migration paths for diffusion of negatively charged oxygen interstitials obtained by concatenation of the elementary paths shown in Fig. 6.5. (a) B_1+B_2 (dashed) and B_2+B_1 (dotted), (b) B_1+X (dashed), B_2+X (dotted), and B_1+B_1 (dash-dotted).*

Taking furthermore into account the ratio of the population probabilities for the dumbbell ($O_{i,db}$) and rotated dumbbell ($O_{i,rot-db}$) states, one obtains

$$D_\perp = \frac{1}{2}\Gamma_0 a^2 \left[3e^{-\beta\Delta E_{A1}} + 3e^{-\beta(\Delta E_{O_i}+\Delta E_{A2})} + e^{-\beta\Delta E_{B1}} + e^{-\beta\Delta E_{B2}} + 4e^{-\beta\Delta E_C}\right] \tag{6.9}$$

$$D_\parallel = \frac{3}{4}\Gamma_0 c^2 \left[e^{-\beta\Delta E_{B1}} + e^{-\beta\Delta E_{B2}} + e^{-\beta\Delta E_C}\right]. \tag{6.10}$$

On the other hand, for the negative charge states, the calculations have shown the energy difference between the two dumbbell configurations to be larger than some of the barriers in the system. Therefore, only the rotated interstitial ($O_{i,rot-db}$) can contribute to oxygen diffusion. Furthermore, the saddle point configuration along paths B_1 and B_2 is found to be essentially identical with the dumbbell interstitial ($O_{i,db}$). In order to account for these observations, modified first-nearest neighbor migration paths need to be constructed by concatenating the elementary processes B_1, B_2, and X as shown in Fig. 6.8. Using the multiplicities and displacements from Tab. 6.2, the diffusivities are obtained as

$$D_\perp = \Gamma_0 a^2 \left[6e^{-\beta\Delta E_{A2}} + 13e^{-\beta\Delta E_{B1}} + 7e^{-\beta\Delta E_{B2}}\right] \tag{6.11}$$

$$D_\parallel = \frac{27}{8}\Gamma_0 c^2 \left[e^{-\beta\Delta E_{B1}} + e^{-\beta\Delta E_{B2}}\right] \tag{6.12}$$

where process C has been neglected because of its large migration barriers (see Sec. 6.4.1 and Tab. 6.1).

In order to obtain the tracer diffusivities (assuming purely intrinsic behavior), the formation enthalpies derived in the previous chapter are used (for completeness reproduced in Tab. 6.1). The attempt frequency was approximated by the Debye frequency [9] which yields $\Gamma_0 \approx 8\,\mathrm{THz}$.

Comparison with experiment

In the past a number of accounts on the diffusion of oxygen in zinc oxide have been published (see Refs. [116, 117, 118, 119, 120, 121]; also compare literature review in Ref. [119]). The earliest studies relied on gaseous-exchange techniques [116, 117], but later on these data have been deemed as unreliable because of experimental problems related to the use of platinum tubes [118] and the evaporation of zinc oxide [118, 119]. More recent studies employed secondary ion mass spectroscopy (SIMS) to obtain diffusivities from depth profiles [119, 120, 121] and also included intentionally doped samples [120, 121]. Despite these

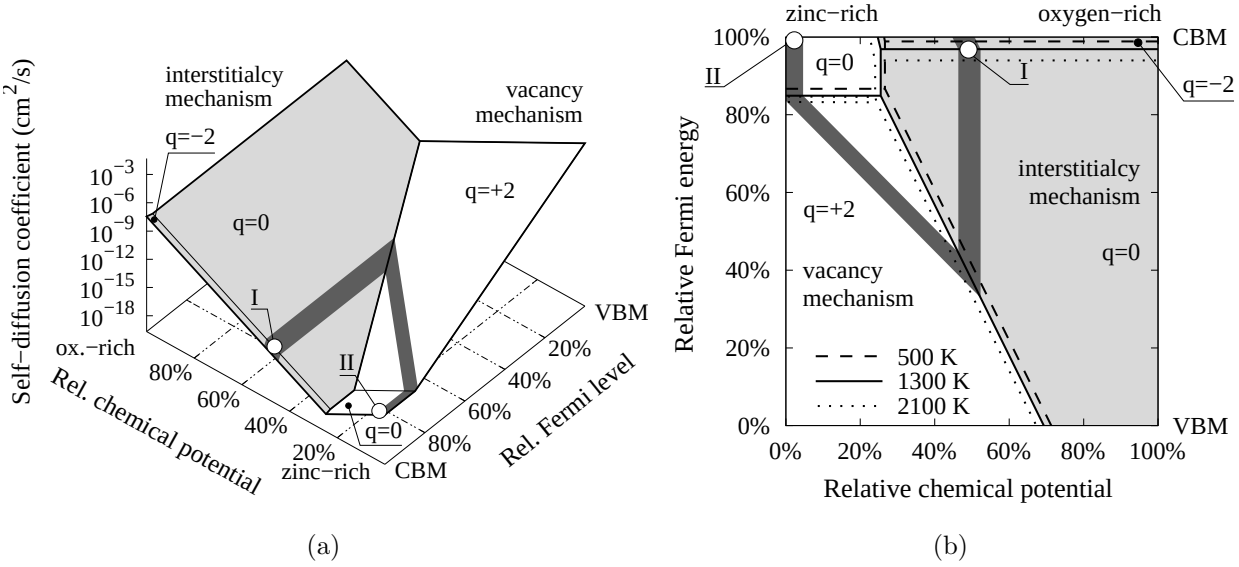

(a) (b)

Figure 6.9.: *Competition between vacancy and interstitialcy mechanisms. (a) Dependence of diffusivity on chemical potential and Fermi level at a temperature of 1300 K. (b) Effect of temperature. The dark grey areas indicate the experimental data range around 1300 K. The Arrhenius plots for regions I (interstitialcy mechanism dominant) and II (vacancy mechanism dominant) are shown in Fig. 6.10.*

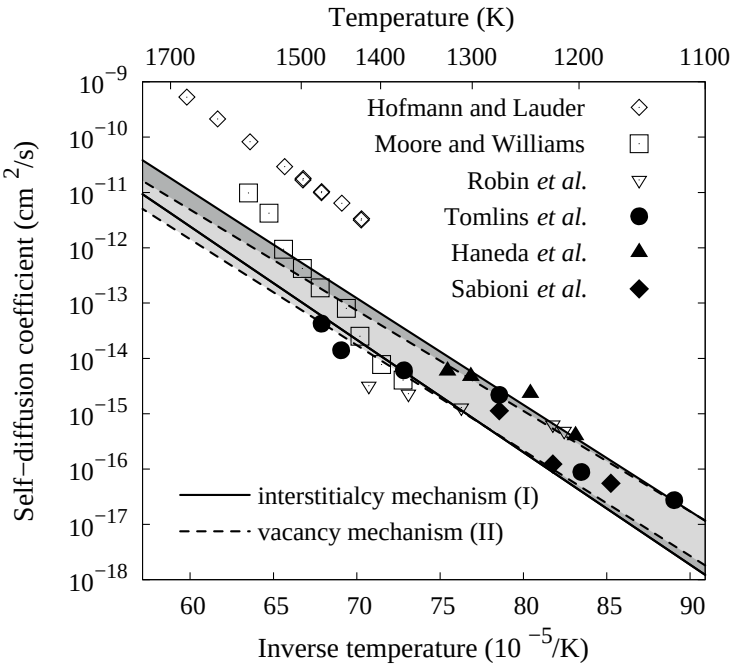

Figure 6.10.: *Oxygen tracer diffusivity in zinc oxide from experiment and calculation. Experimental data from Moore and Williams (Ref. [116]), Hofmann and Lauder (Ref. [117]), Robin et al. (Ref. [118]), Tomlins et al. (Ref. [119], 3M sample), Haneda et al. (Ref. [120]), and Sabioni et al. (Ref. [121]). Solid and dashed lines correspond to regions I (interstitialcy mechanism dominant) and II (vacancy mechanism dominant) in Fig. 6.9, respectively. The reliability of the data from Refs. [116] and [117] has been questioned in the past (see Refs. [118, 119] and text for details) but included in the plot for completeness.*

efforts a consistent picture has not emerged yet. The pre-factors and activation energies reported in the literature are widely spread which according to the analysis by Tomlins *et al.* [119] is probably related to insufficient statistics. Furthermore,direct comparison with the experimental diffusion data is hampered, since there are unknown parameters such as the Fermi level, the chemical potentials of the constituents, or possible impurity induced changes in the intrinsic defect concentrations.

The dependence of the self-diffusion coefficient on chemical potential and Fermi level as well as the resulting complicacies in the comparison with experiment are exemplified in Fig. 6.9. Interstitialcy and vacancy mechanisms dominate under oxygen and zinc-rich conditions, respectively. The larger formation enthalpies (ΔH^f) of oxygen interstitials as compared to vacancies are compensated by lower migration enthalpies (ΔH^m), leading

to a balance between the two mechanisms. (The areas corresponding to vacancy and interstitialcy mechanisms in Fig. 6.9 are nearly equally large). As illustrated in Fig. 6.9(b), the transition between the two regimes is only weakly dependent on temperature showing a slight increase of the interstitialcy mechanism region with rising temperature.

The range of experimental data is shown by the dark grey shaded area, which reveals that both mechanisms can *in principle* explain the experimentally observed diffusivities. Since undoped zinc oxide typically exhibits n-type behavior, Fig. 6.10 compares the temperature dependence of the diffusivity near the bottom of the conduction band for the cases I (interstitialcy mechanism dominates) and II (vacancy mechanism dominates) indicated in Fig. 6.9. Both mechanisms yield similar curves and show good agreement with the experimental data in the temperature region up to about 1450 K. Above this temperature the experimental data is very unreliable and subject to question as discussed before [119].

At this point, one can conclude that both mechanisms can explain the experimentally measured diffusivities. Since all experimental studies were performed in oxygen atmosphere, the conditions are, however, closer to the oxygen-rich side of the phase diagram for which the interstitialcy mechanism dominates. Sabioni suggested that oxygen interstitial diffusion occurs by motion of null or negatively charged species [133] which is supported by the present analysis. Zinc oxide is typically intrinsically n-type conducting and the oxygen interstitial is indeed found to diffuse in charge states $q = 0$ and $q = -2$.

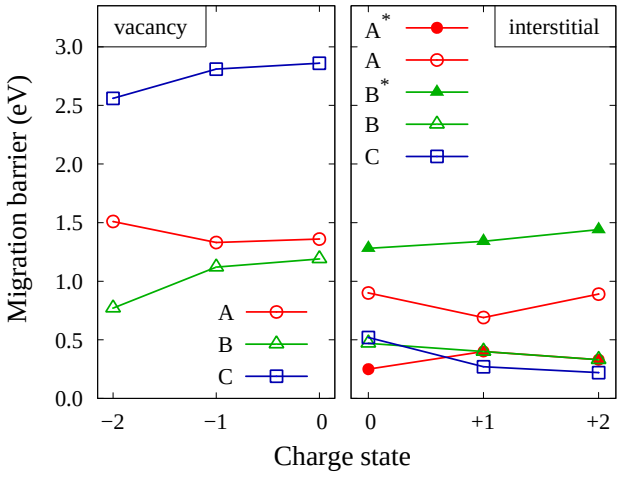

Figure 6.11: *Charge state dependence of migration barriers for zinc vacancy (left) and interstitial (right) diffusion.*

Table 6.3.: *Energy barriers for zinc vacancy and interstitial migration in units of eV as obtained from CI-NEB calculations. Displacements are given with respect to the lattice constants a and c. The formation enthalpies of the respective ground state configurations obtained in Chapter 5 are included for reference (zinc-rich conditions, Fermi level at valence band maximum). ζ_i: multiplicities (compare equation (6.3)); $\lambda_\perp$: displacement within (0001) plane in units of a; $\lambda_\parallel$: displacement parallel to [0001] axis in units of c (a and c are the lattice constants of the wurtzite structure).*

Migration path		$\boldsymbol{\zeta_i}$	$\boldsymbol{\lambda_\parallel}$	$\boldsymbol{\lambda_\perp}$	**Charge state**		
Zinc vacancy, V_{Zn}					$q=0$	$q=-1$	$q=-2$
1st nbr: in-plane	A	6	a	0	1.36	1.33	1.51
1st nbr: out-of-plane	B	6	$a/\sqrt{3}$	$c/2$	1.19	1.12	0.77
2nd nbr: out-of-plane	C	6	$2a/\sqrt{3}$	$c/2$	2.86	2.81	2.56
formation enthalpy					5.60	5.96	7.06
Zinc interstitial, Zn_i					$q=+2$	$q=+1$	$q=0$
1st nbr: in-plane (interstitial)	A*	6	a	0	0.33	0.40	0.25
1st nbr: in-plane (interstitialcy)	A	6	a	0	0.89	0.69	0.90
1st nbr: out-of-plane (interstitial)	B*	2	0	$c/2$	1.44	1.34	1.28
1st nbr: out-of-plane (interstitialcy)	B	2	0	$c/2$	0.33	0.40	0.47
2nd nbr: out-of-plane (interstitialcy)	C	6	a	$c/2$	0.22	0.27	0.52
formation enthalpy					0.02	1.69	4.25

6.5. Zinc

6.5.1. Migration paths

Vacancy diffusion

The mechanisms for zinc and oxygen vacancy migration are completely equivalent and have been discussed in Sec. 6.4.1. The calculated migration barriers are compiled in Tab. 6.3 and shown as a function of charge state in Fig. 6.11. Vacancy migration by out-of-plane jumps to first nearest neighbors (path B) is energetically preferred. The barrier for this path decreases from 1.19 eV to 0.77 eV going from the neutral to the doubly negative charge state. Taking into account the projections of the displacement vector perpendicular and parallel to the [0001] direction, path B leads to nearly isotropic diffusion (also compare equations (6.7) and (6.8)).

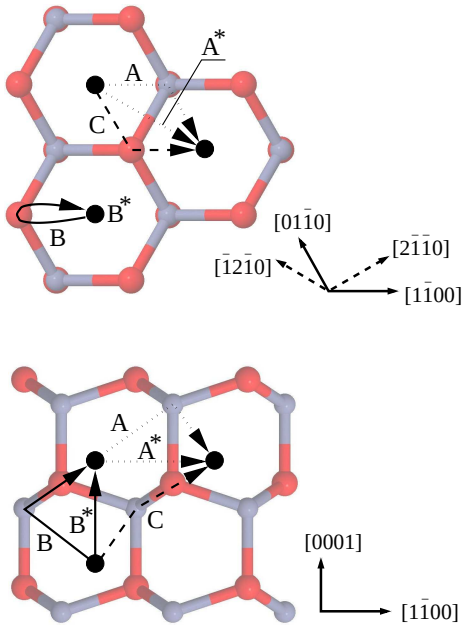

Figure 6.12: *Diffusion paths accessible to zinc interstitials on the wurtzite lattice via jumps to first or second nearest neighbor sites. A: in-plane migration to first nearest neighbors; B and C: out-of-plane migration to first and second nearest neighbors, respectively. Interstitial mechanisms (in contrast to interstitialcy mechanisms) are marked with asterisks.*

Interstitial diffusion

Zinc interstitials occupy the octahedral interstitial sites of the wurtzite lattice located at the centers of the hexagonal $\langle 0001 \rangle$ channels. The interstitial sites span a simple hexagonal lattice with an axial ratio which is half as large as the one of the underlying wurtzite lattice. The resulting migration paths are shown in Fig. 6.12. Ion migration can occur both via pure *interstitial mechanisms*, i.e. via jumps on the simple hexagonal interstitial site lattice, as well as via *interstitialcy mechanisms*. In-plane migration of zinc interstitials can occur via jumps to first-nearest neighbor zinc interstitial sites along $\langle 2\bar{1}\bar{1}0 \rangle$ (process A*). Equivalently, out-of-plane motion is possible by first-neighbor jumps through the $\langle 0001 \rangle$ channels of the wurtzite lattice (process B*). In-plane and out-of-plane motion can also occur via interstitialcy mechanisms involving first-nearest neighbors. The interstitialcy mechanisms A and B shown in Fig. 6.12 and the interstitial mechanisms A* and B* lead to equivalent final configurations. Out-of-plane motion via second-nearest neighbor sites is finally also possible via interstitialcy mechanism C equivalent to an effective displacement of $a/\sqrt{6}\langle 2\bar{1}\bar{1}0 \rangle + c/2\langle 0001 \rangle$.

The calculated migration barriers are compiled in Tab. 6.3 and plotted as a function of charge state in Fig. 6.11. For first neighbor in-plane migration the interstitial mechanism (A*) is energetically favored while for first-neighbor out-of-plane migration the interstitialcy mechanism (B) yields the lowest barriers. For any charge state the smallest (dominant)

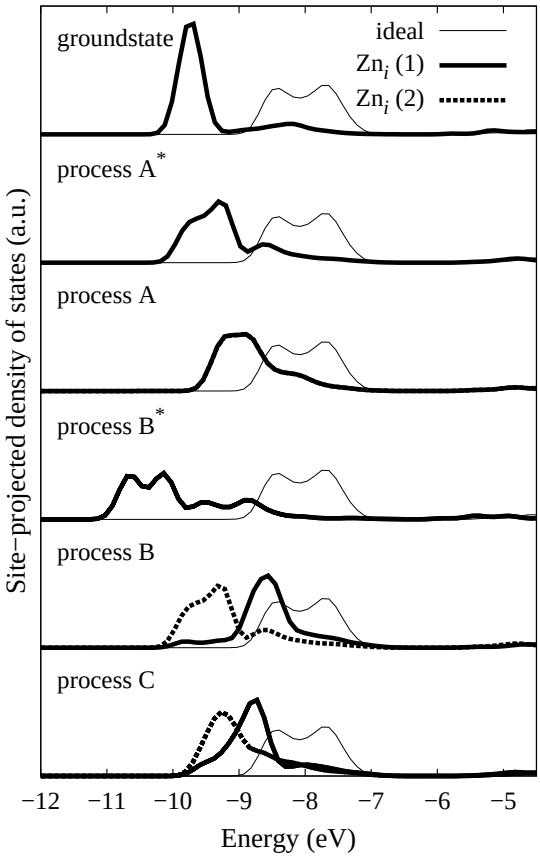

Figure 6.13: *Site-projected electronic density of states of the diffusing zinc atoms in the saddle point configurations of the interstitial mechanisms. For interstitial mechanisms only one atom diffuses (processes A*, B*) while for the interstitialcy mechanisms (processes A, B, C) two zinc atoms are involved.*

migration barrier is just about a few tenths of an eV (Tab. 6.3) which implies that zinc interstitials should be mobile down to very low temperatures. Using the Einstein relation to estimate the onset temperature for annealing as in Sec. 6.4.1, one obtains threshold temperatures for zinc interstitial migration between 90 and 110 K ($q = +2$), 110 and 130 K ($q = +1$), and 100 and 120 K ($q = 0$). This is in excellent agreement with annealing experiments which find mobile intrinsic defects at temperatures as low as 80 to 130 K [130, 31, 131] (also compare Sec. 6.4.1).

Thomas performed conductivity experiments to measure zinc diffusion and interpreted the activation energy of 0.55 eV as the barrier for zinc interstitial migration [134]. This value is, however, not only higher than the ones found in the DFT calculations but also inconsistent with the threshold temperatures obtained in several recent annealing experiments [31, 130, 131]. Since little experimental details are given in Ref. [134], it is, however, difficult to assess possible origins of this discrepancy.

Notably, with the only exception being the neutral charge state, the lowest migration barriers are obtained for the second neighbor mechanism (process C). Similar to the case of path B for vacancy diffusion, process C involves both in-plane and out-of-plane displacements and, therefore, leads to nearly isotropic diffusion characteristics. In contrast, interstitial migration along the ⟨0001⟩ channels of the wurtzite lattice (process B) is energetically rather unfavorable. As demonstrated in Fig. 6.13 analysis of the site-projected electronic density of states for the migrating zinc atoms shows the saddle point configuration along path C to deviate the least from the ideal configuration, providing and explanation for the very small energy difference between the initial and the transition state.

6.5.2. Discussion

Migration barriers for zinc vacancies and interstitials have been previously calculated by Binks and Grimes (see Ref. [135] and Ref. 17 as cited by Tomlins *et al.* [136]) using analytic pair potentials in combination with a shell-model description of the oxygen ions. They considered jumps to first-nearest neighbors only and did not include interstitialcy mechanisms. In the past, these results were frequently used to interpret experiments and, in particular, to discriminate between interstitial and vacancy mechanisms (see Ref. [136] and Ref. 12 therein). With respect to the doubly negative zinc vacancy (V''_{Zn}) there is at least reasonable agreement between the shell-model potential calculations and the DFT data obtained in the present work. According to Ref. [136] the barriers for processes A and B are 1.81 eV and 0.91 eV, respectively, while the present calculations give values of 1.51 eV and 0.77 eV. For the zinc interstitial, there are, however, significant differences: the DFT barriers are in general smaller and in contrast to the analytic potential calculations indicate isotropic diffusion.

As for oxygen (Sec. 6.4.2) the detailed knowledge of all relevant migration paths and related barriers allows to calculate the macroscopic diffusivities. The vacancy diffusivity is given by equations (6.7) and (6.8) derived previously. Using the equations given in Sec. 6.4.2 one obtains for the zinc interstitial

$$D_\perp = \frac{3}{2}\Gamma_0 a^2 \left[e^{-\beta\Delta E_{\mathrm{A}^*}} + e^{-\beta\Delta E_{\mathrm{A}}} + e^{-\beta\Delta E_{\mathrm{C}}}\right] \tag{6.13}$$

$$D_\parallel = \frac{1}{4}\Gamma_0 c^2 \left[e^{-\beta\Delta E_{\mathrm{B}^*}} + e^{-\beta\Delta E_{\mathrm{B}}} + 3e^{-\beta\Delta E_{\mathrm{C}}}\right]. \tag{6.14}$$

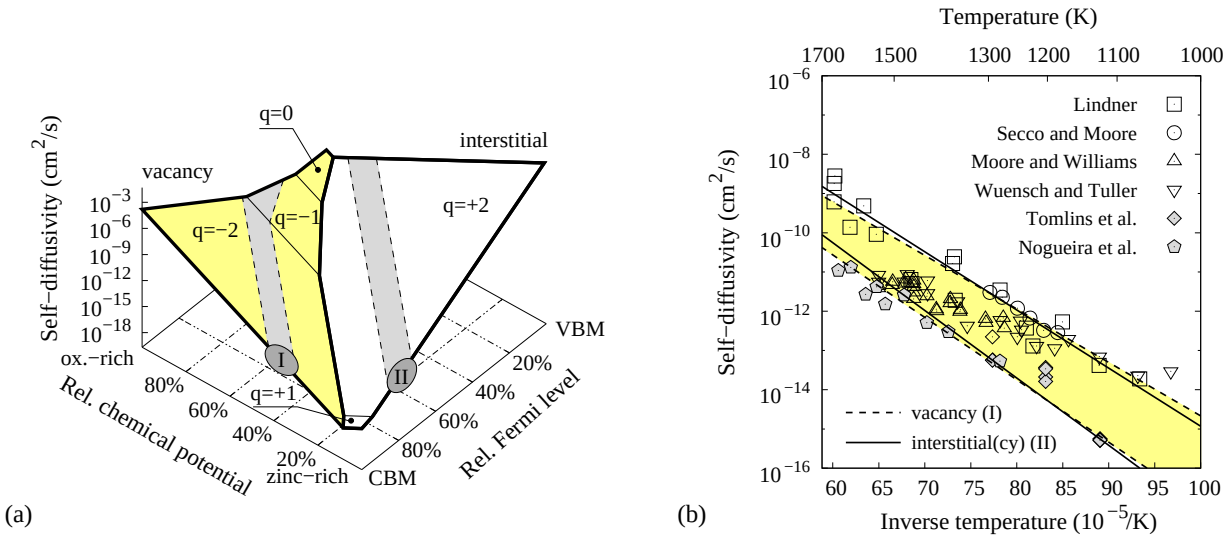

Figure 6.14.: *(a) Dependence of zinc self-diffusion on Fermi level and chemical potential. (b) Temperature dependence for two combinations of chemical potential and Fermi level representative for vacancy (I) and interstitialcy (II) dominated diffusion as indicated by the dark grey ellipsoids in panel (a). Experimental data: Lindner (1952, MTS, Ref. [137]), Secco and Moore (1955/1957, GE, Refs. [138, 139]), Moore and Williams (1959, MTS, Ref. [116]), Wuensch and Tuller (1994, MTS, Ref. [140]), Tomlins et al. (2000, SIMS, Ref. [136]), Nogueira et al. (2003, MTS, Ref. [141]). MTS: method of thin sections, GE: gaseous exchange, SIMS: secondary ion mass spectroscopy.*

The variation of the self-diffusion (tracer) coefficient with the chemical potential and Fermi level as derived from the DFT calculations is shown for a temperature of 1300 K in Fig. 6.14(a). The light grey shaded area indicates the experimental data range at this temperature. Since Fermi level and chemical potential are unknown for these experiments a more direct comparison is not possible. For two exemplifying combinations of Fermi level and chemical potential (dark grey shaded areas I and II in Fig. 6.14(a)) the temperature dependence of the diffusivity is shown in Fig. 6.14(b). Both mechanisms reproduce the experimentally observed dependence. The analysis illustrates that vacancy mediated diffusion can explain the experimental data for Fermi levels close to the conduction band minimum (CBM) and chemical potentials which tend to oxygen-rich conditions. In the opposite case zinc interstitial mediated diffusion should dominate. Since most often ZnO is n-type conducting the diffusion studies in the literature most likely sampled zinc vacancy mediated self-diffusion.

Together with the results for the migration of oxygen it is now possible to establish a hierarchy for the mobilities of intrinsic defects in zinc oxide. The most mobile defects are zinc interstitials followed by oxygen interstitials, zinc vacancies and oxygen vacancies. These data provide further support for the most widely discussed model for degradation of zinc oxide based varistors. This model assumes zinc interstitials to migrate in the vicinity of grain boundaries and oxygen vacancies to be rather immobile (see e.g., Ref. [29, 30]).

6.6. Potential sources of error

In DFT calculations of point defect properties, three major sources of error have to be taken into account (also compare previous chapter): (1) the underestimation of the band gap, (2) elastic, and, if charge defects are considered, (3) electrostatic image interactions.

The underestimation of the band gap is an intrinsic shortcoming of the local density (LDA) or generalized gradient (GGA) approximations. It is crucial to correct for this deficiency if formation enthalpies (ΔH^f) are to be computed for configurations with different electronic properties, for example acceptor and donor-like defects [80, 19]. On the other hand, migration barriers (ΔH^m) are obtained as energy *differences* between *electronically similar* configurations. In addition, unlike formation enthalpies, they do not depend explicitly on the Fermi level. In the present work the GGA+U method is used to correct for the position of the Zn-3d levels which also results in a significantly larger band gap (1.83 eV with GGA+U *vs.* 0.75 eV with GGA). The migration enthalpies for the lowest energy paths obtained with GGA and GGA+U differ by at most 0.3 eV which amounts to a much smaller effect than in the case of formation enthalpies (compare Table 5.1). Therefore, the remaining band gap error should have a small impact on the calculated migration barriers.

Due to the use of periodic boundary conditions, strain and electrostatic interactions are present between defects in neighboring supercells: Strain interactions scale approximately as $\mathcal{O}(V^{-1/3})$ (where V is the supercell volume). If calculations are performed at fixed lattice constants, the $p\Delta V_f$ term (where p is the pressure and ΔV_f is the defect formation volume) is non-zero and leads to an additional contribution to the calculated formation enthalpy. For charged defects image charge interactions are present, which can be corrected based on a multipole expansion of the excess charge distribution [109] (compare Sec. 5.4.2). Again, these effects are crucial if formation enthalpies are computed. In contrast, in the case of

migration barriers, the initial and transition states are structurally as well as electronically similar, and migration volumes are typically just about one tenth of the respective defect formation volumes. Therefore, finite size effects can be expected to play a minor role in the calculation of migration barriers.

From this argumentation it is concluded that the errors in the migration barriers can be expected to be smaller than the errors in the formation enthalpies. Since the typical error in the formation enthalpies is estimated to be smaller than 0.1 eV(see Refs. [18, 19, 20] and the two foregoing chapters), the error in the migration barriers should be some fraction of this value.

If an intrinsic diffusion mechanism is operative (compare Sec. 6.4.2), the activation energy observed in tracer experiments, comprises both the migration as well as the formation enthalpy (see equations (6.4) and (6.6)). The relative error in the tracer diffusivity is, therefore, not governed by the error in ΔH^m but by the error in ΔH^f.

6.7. Conclusions

Density functional theory calculations were employed in conjunction with the climbing image nudged elastic band method to derive migration paths and saddle points for the motion of intrinsic defects in zinc oxide. Where direct comparison is possible the present results agree very well with experiments. The calculations yield very low barriers both for oxygen interstitials migrating in negative charge states and zinc interstitials, which provides an explanation for the low onset temperatures observed in annealing experiments. The high mobilities of intrinsic interstitial defects are likely to contribute to the radiation hardness of zinc oxide [31], since they allow for rapid annealing of Frenkel pairs or defect agglomerates.

Which diffusion mechanism prevails, depends on the chemical potentials of the constituents as well as the Fermi level, i.e. in practice the process conditions and the presence of impurities or dopants. For oxygen, vacancy and interstitial diffusion dominate under zinc and oxygen-rich conditions, respectively. For typical diffusion experiments carried out in oxygen atmospheres, the interstitialcy mechanism is, therefore, the major path for oxygen migration. Zinc self-diffusion occurs via a vacancy mechanism for predominantly oxygen-rich and n-type conducting conditions.

At the time being, a direct comparison between calculation and diffusion experiments is hampered since information on chemical potentials and Fermi level is not available for the experimental data in the literature. The present results will, hopefully, serve as a motivation and support for future experiments and their interpretation. Furthermore, it can be anticipated that the detailed description of migration paths presented in this chapter will aid the development of strategies to systematically enhance or impede the diffusion of oxygen and zinc, will provide the data basis for continuum modeling of zinc oxide structures and devices, and will serve as guidance for studying atomic migration in other wurtzite crystals.

Part III.

Interatomic bond-order potential for zinc oxide

7. Review of potential schemes

In this chapter a review is given of various potential schemes available for modeling bonding in metals and covalent semiconductors as well as compounds. Particular attention is paid to systems which display a mixture of ionic-covalent bonding characteristics as typified by zinc oxide.

7.1. Introduction

Analytic potentials sacrifice the electronic degrees of freedom and are therefore computationally much more efficient than quantum mechanical calculation schemes such as density functional theory. Thereby, they enable static as well as dynamic simulations of ensembles of a few thousand up to a several million atoms extending to the nano or even microsecond time scale.

From the standpoint of quantum mechanics the cohesion of a solid arises from the complex many-body interactions between the valence electrons of the atoms. In general terms, analytic potentials reduce the complexity of this system by averaging out the electronic degrees of freedom and by considering interactions between individual atoms instead. As the electrons are the key ingredients of chemical bonding, by coarse-graining the electronic system necessarily some information is irreversibly lost. A judiciously chosen potential form, however, can deliver very good approximations of the real bonding behavior.

Metal oxides (and zinc oxide in particular) represent an especially difficult case for modeling because of their complex electronic structure and intricate mixture of ionicity and covalency. Therefore, very few potentials for such systems are available in the literature. In order to be useful, a potential scheme should also be capable of describing the elementary phases. The situation is further complicated if the system of interest features such diverse phases as a hexagonal close packed metal (zinc), a gaseous phase (dimeric oxygen), and a

ionic-covalent semiconductor (zinc oxide). In the following, potential schemes are reviewed which have been developed to model metallic or covalent bonding as well as schemes which have been applied to describe compounds with ionic and ionic-covalent bonding characteristics. Only very few potential models actually possess the capability to unify the various bonding types within a single formalism.

7.2. Metallic and covalent bonding

Since the beginning of the 1980ies augmented efforts have been devoted to the development of more realistic potential models for metallic and covalently bonded systems [142, 143, 33] inspired by fundamental observations on the characteristic of the chemical bond [144, 145, 146, 32]. In contrast to pure pair potentials (e.g., Lennard-Jones or Morse potentials) these potentials incorporate either implicitly or explicitly many-body interactions.

The embedded-atom method (EAM) [142] has emerged as the most successful model for metallic bonding and numerous potentials employing this scheme have been developed for elemental metals as well as metallic alloys. The modeling of covalent bonding has turned out to be more challenging which has lead to the development of several competing schemes: Keating type potentials are expansions of the cohesive energy about the ground state in terms of bond lengths and angles. Following Carlsson's classification of analytic potentials this class of potentials is referred to as cluster potentials [147], the most prominent member being the Stillinger-Weber potential scheme [143]. Analytic bond-order potentials [32] are similarly classified as cluster functionals. They are approximations of the moment expansion within the tight-binding scheme [148] and close relatives to the embedded-atom method [149, 150]. The best known representatives are the modified embedded-atom method [151] (MEAM) and analytic bond-order potential [32, 33] (ABOP) schemes. The latter approach has been extended by Brenner and coworkers by including overbinding corrections [152], four-body terms and long-range interactions [153] to model hydrocarbons.

The ABOP formalism was shown to be formally equivalent to the embedded-atom method [149]. In fact, it turns out that the bond-order ansatz is also capable of describing many pure metals (including transition metals) on the same footing as covalent materials [154, 155]. Pettifor and coworkers furthermore showed that bond-order potentials can be rigorously derived within tight-binding theory based on a second moment expansion of the

density of states [148, 156]. They later extended their approach to higher moments and multi-component systems [157].

7.3. Bonding in compounds

For many elemental metals and semiconductors analytic potentials provide very good approximations of the materials behavior and have proven useful in a wide variety of applications. With regard to compounds, the situation is more complex since in most systems cohesion arises from a mixture of covalent, metallic, ionic and van-der-Waals interactions. Formally, the cohesive energy can be written as a sum of these contributions, and if a realistic description of the bonding behavior is pursued, one needs to assess the relative weight and the mathematical representations of each of these terms. In the following, potential schemes from the literature are compared focusing on the treatment of covalency vs ionicity, and, where applicable, charge equilibration.

The alkaline-halides and alkaline earth-oxides are typical example for ionic compounds in which long-range Coulomb interactionsbetween the ions dominate. Simple pair potentials which combine a Coulomb potential with a short ranged, spherically symmetric repulsive potential are usually sufficient in order to obtain a satisfactory description. Shell-model potentials (see e.g., Refs. [158, 159] and [135]) represent a somewhat more refined approach combining short ranged repulsive, longer ranged dispersive, and ionic interactions with a simple harmonic model for atomic polarizability [160]. The ionic charges are kept fixed at their nominal values (and independent of the atomic environment). In the past, shell-model potentials have been applied to a wide range of materials since they offer a very handy formalism with few fitting parameters and yield useful models if only a small section of configuration space is of interest. Since three-body interactions are not explicitly taken into account covalent contributions either have to be neglected or are subsumed in the fitting parameters. The formalism is incapable of describing pure elements which renders it inapt for simulations in which the boundary phases of the material play a role. Furthermore, due to the long-range interaction of the Coulomb potential the treatment of electrostatic contributions in static as well as dynamic simulations is computationally very demanding.

In contrast to ionic interactions, covalent bonding is characterized by strong directional dependence, and therefore angle dependent terms need to be taken into account. By merging Stillinger-Weber type [143] two and three-body potentials with terms describing

Coulomb, monopole-dipole, and van-der-Waals interactions, Vashishta and coworkers arrived at a scheme capable of describing materials such as silicon carbide [161, 162] and gallium arsenide [163]. The ions are assigned fixed, effective charges and the long-range electrostatic interactions are truncated at some intermediate distance reducing the computational effort substantially. The potentials are designed such that the boundary phases can be described on the same basis as the compound. Unfortunately, parameter sets for the SiC and GaAs potentials have not been published. A Vashishta-type potential for zinc oxide was derived and applied to study homoepitaxial growth on (0001)-ZnO faces [164]. Since in fitting and testing only a very limited number of properties was considered, it is, however, difficult to evaluate the transferability and reliability of this potential.

In order to simulate metal/metal-oxide interfaces Streitz and Mintmire devised a scheme (ES+) which merges the EAM scheme with an ionic potential [165]. The model explicitly accounts for charge transfer between anions and cations by equilibrating the ionic charge for each configuration which renders it computationally very demanding. The scheme has been applied with some success for modeling alumina [165] and with modifications to titania [166].

More recently, Duin *et al.* constructed a reactive force field (ReaxFF) which features a combination of many-body, van-der-Waals, and Coulomb terms [167]. Originally, designed for hydrocarbons the scheme is sufficiently flexible to describe also oxidic compounds and metals as demonstrated in the case of alumina [168]. Similarly, to the Vashishta potentials, the Coulomb potential is truncated at some distance. The effective ionic charges are determined via charge equilibration akin the Streitz-Mintmire approach. The full functional form features more than ninety parameters. Many degrees of freedom for fitting can improve the flexibility of the potential scheme but parameter space sampling during fitting becomes increasingly complex and the risk for spurious minima in the potential hypersurface grows.

As outlined in the foregoing section purely covalent bonding exemplified by elemental semiconductors such as carbon, silicon, or germanium, can be well described within the ABOP approach [32, 33, 152]. It turns out the formalism works similarly well for strongly covalent compounds. In fact, the ABOP scheme in its original form as well as in slightly modified versions has been employed with great success to the modeling of a whole variety of materials, including covalently bonded group-III, group-IV and group-V semiconductors

and compounds [150, 169, 170, 171, 172, 173, 174, 175, 176, 177], transition metals and transition metal carbides [154, 178, 155], as well as partially ionic systems [179].

In this dissertation the applicability of the bond-order scheme as described in Refs. [150, 154] to the description of zinc oxide as a prototypical oxide was explored. To begin with, a computer code was developed which is presented in the following chapter.

8. Pontifix/Pinguin: A code for fitting analytic bond-order potentials*

This chapter describes the Pontifix/Pinguin *program package which provides a simple interface for the generation of analytic bond-order potentials for elements as well as compounds. Based on a set of data comprising the cohesive energies and bond lengths for a number of structures and at least one complete set of elastic constants for one of these structures, the potential parameter set(s) are optimized using the Levenberg-Marquardt least-squares minimization algorithm. The program allows to fit several parameter sets simultaneously. Furthermore, it is possible to include an arbitrarily large number of neighbors which allows to develop analytic bond-order potentials which extend to the second or third neighbor shell.*

8.1. Introduction

In the previous chapter, an extensive review of analytic potential schemes has been given. It turned out that the analytic bond-order potential scheme is one of the most flexible models for describing various bonding situations. In the present chapter, the Pontifix/Pinguin program code is introduced which has been developed as part of this work and which allows to fit analytic bond-order potentials for elements as well as compounds.

For pair potentials with a small number of parameters, given a set of properties, fitting parameter sets is usually rather straight forward. For Lennard-Jones and Morse potentials the parameters can be derived by hand while in the case of ionic potentials, codes such as Gulp [180, 181] provide a very simple means to fit parameters. As the dimensionality

*Parts of the present chapter have been published in Ref. [1].

of parameter space increases and the functional form becomes more complex, the effort expended to obtain suitable parameter sets increases enormously [182]. Therefore, fitting such potentials is a very laborious and tedious task [183].

Ideally, a potential should be transferable, accurate and computationally efficient [183] but in practice one needs to find a compromise between these properties. In the past this problem has been approached from different perspectives. One option is to use a large number of parameters and a highly flexible potential form. Thereby, it is possible to obtain good agreement with a large number of properties included in the fitting database [184]. However, the risk for artificial minima in the potential hypersurface typically increases with the dimensionality of parameter space which deteriorates the transferability of the potential [182]. For EAM potentials, Mishin and coworkers have performed a detailed investigation of the interplay between the number of parameters and the root mean square error of the fitting and testing databases [185]. They found that there exists an optimal value for the number of parameters, beyond which no further improvement with respect to the properties contained in the testing database can be achieved.

Another important issue is the compilation of the fitting database itself. Usually, the data which enters the fitting process stems from a variety of experimental as well as theoretical sources. Thus it is of primary importance to ensure the compatibility of the data [182] and care must be taken during the construction of the database, e.g. by means of rescaling or shifting calculated data points [185, 154]. Furthermore, the properties which appear in the fitting database should cover as wide a range of possible configurations as possible and include energy as well as force-dependent quantities. In fact, inclusion of cohesive energies and lattice parameters alone neither leads to a good description of elastic properties nor provides satisfactory potentials [186]. On the other hand, information on forces in near-equilibrium situations can be easily included by considering elastic constants or phonon mode frequencies. A more involved approach is to fit directly forces obtained from first-principles calculations [184, 187].

Finally, there are many possibilities to browse parameter space. The optimum choice of algorithm depends on the dimensionality of the system and the functional form of the potential. The most widely adapted methods are simulated annealing and conjugated gradients minimization although alternatives such as genetic algorithms have been considered as well [188].

The following section introduces the functional form implemented in PONTIFIX/PINGUIN. The underlying fitting methodology is described in detail in Sec. 8.3, and Sec. 8.4 gives an overview of the features of the program package.

8.2. Analytic bond-order potential formalism

The following equations summarize the analytic bond-order potential scheme. A physical motivation based on second moment tight-binding theory and a discussion of the functional form can be found in Refs. [32, 33, 149, 152, 148, 154]. The potential form is functionally equivalent to the scheme used by Brenner in his hydrocarbon potential [152], except that the bond conjugation terms (F and H functions) have been left out. The total energy is written as a sum over individual bond energies

$$E = \sum_{i>j} f_{ij}^c(r_{ij}) \left[V_{ij}^R(r_{ij}) - \underbrace{\frac{b_{ij} + b_{ji}}{2}}_{\overline{b_{ij}}} V_{ij}^A(r_{ij}) \right]. \tag{8.1}$$

where for the pair-like attractive and repulsive terms Morse-like pair potentials are adopted

$$V^R(r) = \frac{D_0}{S-1} \exp\left(-\beta\sqrt{2S}(r - r_0)\right), \tag{8.2}$$

$$V^A(r) = \frac{SD_0}{S-1} \exp\left(-\beta\sqrt{2/S}(r - r_0)\right). \tag{8.3}$$

The parameters in these equations are the dimer bond energy D_0, the dimer bond distance r_0 and the adjustable parameter S. The parameter β can be determined from the ground-state oscillation frequency of the dimer. The cutoff function restricts the range of the interaction to first or second nearest neighbors

$$f^c(r) = \begin{cases} 1 & r \le R - D \\ \frac{1}{2} - \frac{1}{2}\sin\left[\frac{\pi}{2}(r-R)/D\right] & |r - R| \le D, \\ 0 & r \ge R + D \end{cases} \tag{8.4}$$

where D and R are adjustable parameters. Explicit three-body interactions are included via the bond-order parameter

$$b_{ij} = (1 + \chi_{ij})^{-\frac{1}{2}}, \tag{8.5}$$

$$\chi_{ij} = \sum_{k(\neq i,j)} f_{ik}^c(r_{ik})\ g_{ik}(\theta_{ijk})\ \exp[2\mu_{ik}(r_{ij} - r_{ik})]. \tag{8.6}$$

The indices monitor the type-dependence of the parameters, which is of importance for the description of compounds. The angular dependence is described by

$$g(\theta) = \gamma \left(1 + \frac{c^2}{d^2} - \frac{c^2}{d^2 + (h + \cos\theta)^2} \right). \tag{8.7}$$

The three-body interactions are thus controlled by the parameters γ, c, d, h, and 2μ each of which depends on the type of atoms i and k.

8.3. Fitting methodology

The approach implemented in PONTIFIX is based on the experience gained during the development of several analytic bond-order potentials in the past years. The code uses conjugate gradients minimization to optimize the input parameter sets which requires manual intervention as fitting proceeds. It has been found that the benefits of more involved optimization algorithms such as simulated annealing or genetic algorithms are outweighed by the possibilities of user control and interaction available in the present approach.

Equations (8.2) and (8.3) which describe the pairwise interactions are equivalent to the equations originally introduced by Tersoff [33] and the respective parameters can be readily transformed into each other. However, unlike Tersoff's version equations (8.2) and (8.3) have the major benefit that the parameters can be given an immediate physical meaning: D_0 and r_0 are the dimer energy and bond length and β is related to the ground-state oscillation frequency, k, of the dimer according to

$$\beta = k \frac{2\pi c_0}{\sqrt{2D_0/\mu}}, \tag{8.8}$$

where μ is the reduced mass[†] of the dimer and c_0 is the speed of light.

By construction the potential fulfills the Pauling relation which relates the energy per bond, E_b, with the bond length, r_b,

$$E_b = -D_0 \exp\left(-\beta\sqrt{2S}(r_b - r_0) \right). \tag{8.9}$$

If D_0, r_0, and β are fixed, then S determines the slope of the Pauling plot and usually its value is adjusted to obtain a good agreement with the input data. The parameter S can

[†]The reduced mass is defined as $\mu = m_1 m_2/(m_1 + m_2)$ where m_1 and m_2 are the masses of the atoms of the dimer.

also be given a physical interpretation and derived from experimental data as described in Ref. [32].

The two parameters in equation (8.4) which specify position and width of the cutoff range, are typically set manually such that the cutoff range extends between the largest first-nearest neighbor distance to the smallest second-nearest neighbor distance among the structures considered. In some cases it is advisable to include second neighbors as well [155]. In principle, PONTIFIX is able to include yet more neighbors but it should be taken into account that the computational cost increases as more and more neighbors are included. Furthermore, due to the extended range of three-body interactions unforeseen and undesirable (artificial) energy minima might develop.

Thus, six out of eleven parameters can be given a physical interpretation and can be set directly based on available experimental or first-principles data. From the remaining five parameters which describe the three-body interactions the parameter 2μ appearing in equation (8.6) stands apart. For structures for which there is only one type of first neighbors with one unique bond length included in the cutoff sphere, the exponential term in equation (8.6) is always one and thus the value of 2μ is immaterial. In turn this implies 2μ affects only structures which involve asymmetric bond lengths. Typically, fitting involves mostly high-symmetry structures the properties of which (excluding thermal vibrations) are unaffected by the value of 2μ. Therefore, it is often possible to adjust 2μ selectively to certain properties after all of the other parameters have been fixed. Such an approach has been chosen e.g., by Tersoff in fitting surface properties. For the same reason the 2μ has sometimes been found to give rise to artefacts [189], whence in the past it has often been set intentionally to zero.

Once the seven parameters discussed above (D_0, r_0, β, S, R, D, and 2μ) have been fixed or given suitable starting values, the remaining four parameters (γ, c, d, and h) are fit to a set of properties which usually comprises the bond lengths and energies of several structures, as well as elastic constants.

8.4. Features of Pontifix

PONTIFIX implements the fitting methodology described in the foregoing section. For optimizing the initial parameter set(s) it uses conjugated gradients minimization [190]. The code is able to fit several mutually dependent parameter sets simultaneously. PINGUIN

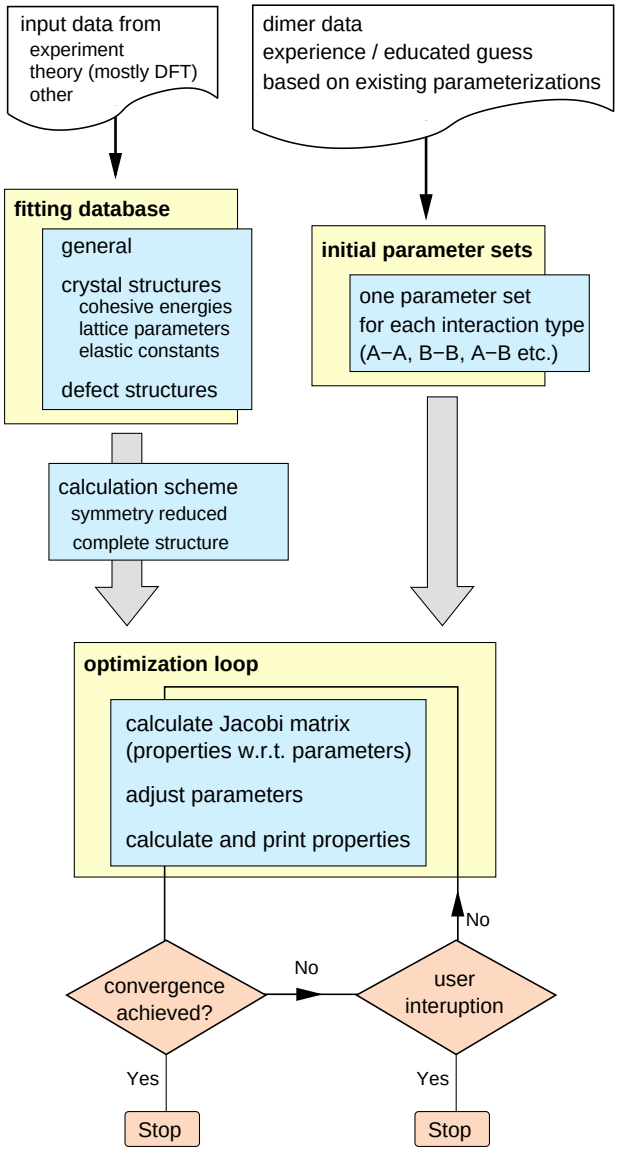

Figure 8.1: *Flow chart of the fitting algorithm implemented in* PONTIFIX. *After construction of the fitting database and begin given initial parameter set(s) the code optimizes the parameter set(s) with respect to the fitting database by conjugated gradients minimization.*

is a graphical user interface programmed using the GIMP Toolkit (`http://www.gtk.org`) which runs under UNIX/LINUX systems. It provides a simple and intuitive tool to create fitting databases, control parameter sets and run PONTIFIX interactively. As input, the user is required to specify a database of properties which is used for fitting the potential and one or more initial set(s) of parameters. An extensive description of the parameters and the syntax of the input files is given in a separate document [191]. A schematic of the fitting process is given in Fig. 8.1.

8.4.1. Parameter sets

The code is able to fit several mutually dependent parameter sets simultaneously. For each of the potential parameters described above an initial value is required. The user can control the fitting process further by fixing individual parameters and by specifying a range within a certain parameter is allowed to vary. The code was run with up to three parameter sets at the same time to fit the binary system W–C [155]. There is no principle limit on the number of parameter sets but it is strongly advised to keep the number of free parameters (or equivalently the dimensionality of parameter space) as small as possible for the sake of computational efficiency and in order to maintain a distinct control over the fitting procedure. This can also be achieved when fitting several parameter sets concurrently by fixing the values of several parameters. For instance for the reasons described above, one can usually leave most of the pair parameters fixed.

8.4.2. Fitting database

General. There are several parameters by which the user controls the output of the program, the break conditions of the fitting routine, and a number of other properties.

Structural properties. When a structure is included in the database of properties, PONTIFIX automatically optimizes the structural parameters such as lattice or internal parameter(s) and calculates the equilibrium cohesive energy. Currently, the following structures are included: dimer, equilateral triangular trimer, linear trimer, graphite, diamond, β-tin, simple cubic, body-centered cubic, simple hexagonal, face-centered cubic, hexagonal closed-packed, rock salt, cesium chloride, zinc blende, CuAu ($L1_0$), Cu_3Au ($L1_2$) and tungsten carbide.

It is possible to calculate the structural properties either by including the first-nearest neighbors only (symmetry reduced) or by considering the complete structure including an in principle arbitrary number of neighbors. In particular, PONTIFIX allows to fit analytic bond-order potentials which include for example the second or third neighbor shell.

For cubic, hexagonal and tetragonal structures it is furthermore possible to calculate elastic properties. The code can calculate the bulk modulus and its pressure derivative as well as the tensor of the second order elastic constants. The code is written in a way to simplify addition of new structures and deformation modes.

Defect structures. Finally PONTIFIX allows to include extended structures in the fitting database such as defect configurations or surfaces. it is possible to take into account volume relaxation for these structures but the atomic positions are not optimized during fitting.

8.5. An illustrative example

In order to illustrate the typical steps during deriving a new parameter set, a silicon potential is discussed, which has been derived as part of a Si–C potential [177]. The dimer energy, bond length and oscillation frequency were taken from experiment to fix the initial values of D_0, r_0, and β. The fitting database furthermore comprised experimental data for the dimer, the diamond and β-tin structures and was complemented by first-principles data for several higher coordinated structures. For the sake of consistency the bond lengths obtained from theory were rescaled and the cohesive energies were shifted such that the adjusted data reproduced the experimental values for the diamond structure. Finally, experimental data on the elastic constants were included for the equilibrium diamond structure. The cutoff parameters were fixed such that the cutoff range fell between the first nearest neighbor distance of the fcc and the second nearest neighbor distance of the bcc structure. An initial value for the parameter S was obtained by fitting the input data to the Pauling relation.

Due to the functional form of $g(\theta)$ in equation (8.7) the h parameter can only assume values between -1 and $+1$. In previous parameterizations for sp^3 coordinated materials values for h ranged from 0 [169] to 1 [152]. Initial values for γ, c, and d are more difficult to find, since they are strongly dependent on each other. Typically, the ratio c/d can be adopted to be on the order of one while γ scales roughly inversely with c^2. Suitable starting values can be taken from previous parameterizations and adjusted by trial and error.

Based on a set of initial values for γ, c, d, and h we then fitted the three-body interaction part using PONTIFIX. In practice, various initial parameter sets were tested until several reasonable combinations were obtained. These initial parameter sets were subsequently improved by selectively varying the values of certain parameters, including or excluding them from the fit and by changing the weights of the properties in the fitting database. During this phase also the values of r_0 and β were released in order to obtain a better fit of the bulk modulus of the diamond structure. This is a simple example of how one can

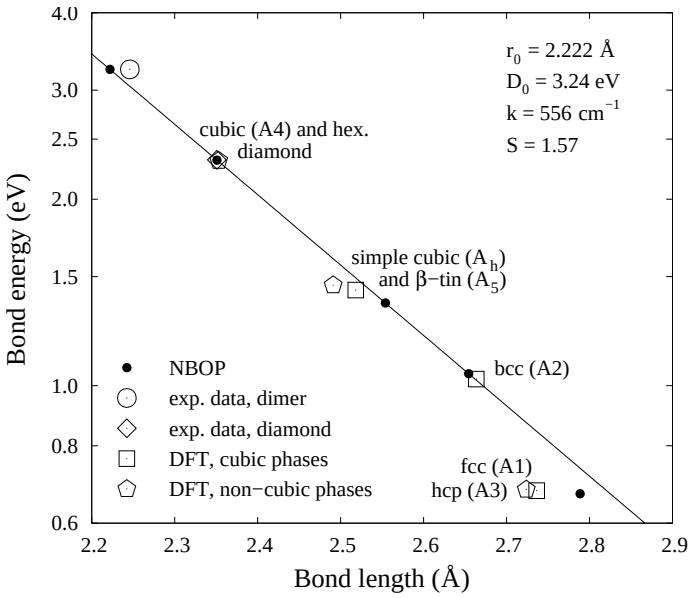

Figure 8.2: *Pauling plot for silicon as obtained from an analytic bond-order potential (Ref. [177]) in comparison with data from experiment and first-principles calculations.*

often link certain parameters (β) and properties (the bulk modulus) in order selectively to optimize the potential.

Fitting the potential further proceeded in a stepwise, iterative manner until a few parameter sets had been isolated which gave a good overall agreement with the fitting database. These parameter sets were then considered for further external testing in simulations of e.g., thermal or defect properties. One or two parameter sets were selected and further optimized again using PONTIFIX. The procedure was repeated until one parameter set gave an overall satisfactory performance. This is exemplified by the Pauling relation shown in Fig. 8.2 which demonstrates the excellent agreement between the analytic bond-order potential and the input data.

8.6. Conclusions

The PONTIFIX/PINGUIN package implements a fitting strategy which has been successfully applied to obtain analytic bond-order potentials for a variety of binary systems. Based on a database of properties provided by the user, PONTIFIX optimizes parameter sets for analytic bond-order potentials of the Abell-Tersoff-Brenner type. In particular, PONTIFIX allows to fit analytic bond-order potentials which include for example the second or third neighbor shell. PINGUIN is a graphical user interface to PONTIFIX allowing to control the fitting procedure interactively in UNIX/Linux environments.

8. Pontifix/Pinguin: *A code for fitting analytic bond-order potentials*

The Pontifix/Pinguin package greatly simplifies the development of analytic bond-order potentials for single as well as multi-component systems and it is hoped to be actively used in the future. The program package is freely accessible for researchers in academic environments.

9. Bond-order potential for zinc oxide*

A short ranged potential for zinc oxide and its elemental constituents is developed using the analytic bond-order formalism introduced in chapters 7 and 8. The potential provides a good description of the bulk properties of zinc oxide over a wide range of coordinations including cohesive energies, lattice parameters, and elastic constants. The zinc and oxygen parts reproduce the energetics and structural parameters of a variety of bulk and in the case of oxygen also molecular structures. The dependence of thermal and point defect properties on the cutoff parameters is discussed. The potential is employed to study the behavior of bulk zinc oxide under ion irradiation.

9.1. Introduction

In this chapter the question is pursued whether a highly ionic compound such as zinc oxide can be treated within a purely covalent model. The neglect of charges avoids the computationally expensive treatment of long-range interactions and, thereby, allows to obtain an atomistic model which is significantly more efficient† than any of the ionic potentials described in Sec. 7.3. From a conceptual point of view, by realizing the counterpart of a purely ionic potential it would become possible to separate ionic and covalent contributions in a given situation by opposing the results obtained with different potentials.

As described in the two foregoing chapters, the ABOP scheme in principle offers the possibility to describe Zn–O, O–O as well as Zn–Zn interactions within a single framework. Although, it turns out that for many situations the neglect of charges is legitimate, it needs

*Parts of the present chapter have been published in Ref. [2].

†For GaN purely covalent as well as partially ionic potentials have been developed [179, 192]. The former is roughly two orders of magnitude more efficient.

Table 9.1: *Parameter sets for describing Zn–Zn, O–O, and Zn–O interactions. R_c^e, D_c^e: cutoff parameters derived for the pure elements; R_c, D_c: default cutoff parameters for simulations of ZnO (see Sec. 9.6 for details).*

Parameter	**Zn–Zn**	**O–O**	**Zn–O**
D_0 (eV)	0.6470	5.166	3.60
r_0 (Å)	2.4388	1.2075	1.7240
S	1.8154	1.3864	1.0455
β (Å^{-1})	1.7116	2.3090	1.8174
γ	4.3909×10^{-5}	0.82595	0.019335
c	77.916	0.035608	0.014108
d	0.91344	0.046496	0.084028
h (θ_c)	1.0	0.45056	0.30545
	(180°)	(116.8°)	(107.8°)
2μ (Å^{-1})	0.0	0.0	0.0
R_c^e (Å)	3.00	2.10	
D_c^e (Å)	0.20	0.20	
R_c (Å)	2.85	2.45	2.60
D_c (Å)	0.20	0.20	0.20

to be acknowledged that the applicability of the ABOP is limited if internal or external electric fields become important as in the case of interfaces or surfaces. The restriction to first-nearest neighbors also implies that the energy difference between the zinc blende and the wurtzite structures vanishes since their local environments are indistinguishable if only first nearest neighbors are included. As will be shown below, within these restrictions the ABOP performs very well in reproducing a variety of bulk properties including cohesive energies, structures, and elastic properties.

In order to demonstrate the usefulness of the present approach and the transferability of the potential, the analytic bond-order potential is employed to simulate the irradiation of bulk zinc oxide.

9.2. Methodology

The functional form of the potential and the fitting methodology used in the present chapter are described in Sects. 8.2 and 8.3. The Pontifix code introduced in Chapter 8 was employed for fitting the parameter sets for Zn–Zn, O–O, and Zn–O which are compiled

	Expt.	Theory	ABOP
EBE	1.61 ± 0.04	1.20 – 1.63	
IBE	3.58	3.31, 3.60	3.60
r_0		1.679 – 1.771	1.724
ω_0	805 ± 40	646 – 913	708

Table 9.2: *Summary of properties of the ZnO dimer. Experimental data from Refs. [194], data from quantum mechanical calculations from Refs. [34, 35]; EBE: extrinsic bond energy (eV); IBE: intrinsic bond energy (eV); r_0: bond length (Å); ω_0: ground state oscillation frequency (cm^{-1}); IBE, r_0 and ω_0 are given for the dissociation of the dimer ground state into higher energy atomic states (T1: $ZnO(X^1\Sigma) \rightarrow Zn(^1S) + O(^1D)$).*

in Tab. 9.1. Cutoff parameters derived for the pure elements are denoted R_c^e and D_c^e, while the parameters appropriate for simulations of the compound ZnO are given in rows R_c and D_c.

9.3. Zinc oxide

The fitting methodology requires data on cohesive energies, lattice constants, and elastic constants of a variety of structures in order to cover a range of coordinations as wide as possible. For zinc oxide a plethora of data from experiment and quantum mechanical calculations is available which could be used for fitting and benchmarking the potential. Therefore, no additional reference calculations were necessary. In order to simplify fitting the experimentally measured hexagonal (wurtzite) elastic constants were transformed to the cubic system (zinc blende) by means of Martin's transformation method [193]. The latter values were then included in the fitting database. The final parameter set is given in Tab. 9.1.

9.3.1. Dimer properties

As the pair parameters of the ABOP are usually adjusted to dimer data, the properties of the ZnO molecule have to be discussed first. The dimer behaves peculiarly in the way that its ground state dissociates into excited atomic states (T1: $ZnO(X^1\Sigma) \rightarrow Zn(^1S) + O(^1D)$) while the dissociation into the atomic ground states occurs from an excited state of the dimer (T2: $ZnO(a^3\Pi) \rightarrow Zn(^1S) + O(^3P)$). This implies that the lowest experimentally

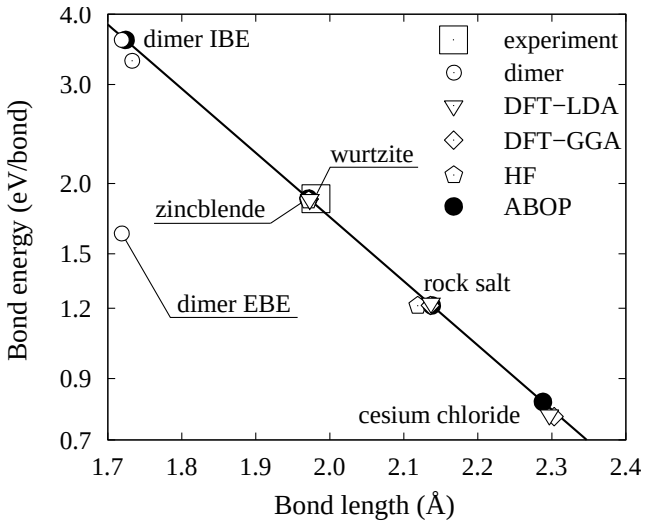

Figure 9.1: *Pauling plot for zinc oxide comparing the analytic bond-order potential (ABOP) with data from experiment, Hartree-Fock (HF) and density functional theory (DFT) calculations.*

determined dimer energy (associated with the extrinsic bond energy, EBE) cannot be described by a single pair potential but corresponds to a crossing-over of the potentials describing the transitions T1 and T2, respectively [194, 35]. For consistency only the dimer energy, bond length and oscillation frequency are considered, which belong to transition T1, that is the decomposition of the dimer ground state into the excited atomic states (intrinsic bond energy, IBE). The parameter set given in Tab. 9.1 yields very good agreement with both the experimental as well as the quantum mechanically computed data for this transition as show in Tab. 9.2.

9.3.2. Bulk Properties

The performance of the ABOP with respect to bulk properties is compared to experiment and DFT calculations in Tab. 9.3. The energy difference between the wurtzite and zinc blende structures is zero due to the neglect of long-range interactions. For the same reason the axial ratio ($c/a = \sqrt{8/3}$) as well as the internal relaxation parameter ($u = 3/8$) of the wurtzite structure are restricted to their ideal values. Otherwise, the agreement with respect to cohesive energies, volumes and bulk moduli is excellent. In particular, the elastic constants of the wurtzite phase compare very well with experiment. Tab. 9.3 also compares the elastic constants of wurtzite calculated directly with the values obtained by Martin's transformation method showing very good agreement throughout.

The Pauling plot in Fig. 9.1 reveals an almost perfect agreement with the Pauling relation (equation (8.9)). Applying the common tangent construction to the energy-volume

Table 9.3.: *Summary of bulk properties of zinc oxide as obtained from the analytic bond-order potential (ABOP) in comparison with experiment and quantum mechanical calculations as well as the shell-model potential due to Lewis and Catlow (LC) [158, 159]. Experimental data from Refs. [71, 195, 73, 196, 197], Hartree-Fock (HF) data from Refs. [14, 198], DFT data from Refs. [16, 14, 15, 198, 199, 200]. Elastic constants obtained by Martin's transformation method [193] are given in brackets. E_c: cohesive energy (eV/f.u.); ΔE: energy difference with respect to ground-state structure (eV/f.u.); V_0: equilibrium volume (Å^3/f.u.); a: lattice constant (Å); c/a: axial ratio; u: internal parameter of wurtzite structure; B, B': bulk modulus (GPa) and its pressure derivative. c_{ij}: elastic constants (GPa); c_{44}^0: unrelaxed shear modulus of zinc blende structure (GPa); ζ: Kleinman parameter [201].*

	Expt.	**ABOP**	**Quantum-mechanical calculations**			**LC**
			LDA-DFT	GGA-DFT	HF	
zinc blende ($F\bar{4}3m$), no. 216, B3						
ΔE		0.0[a]	0.015	0.013	0.052	0.097
a		4.552	4.509	4.633	4.614	4.547
B	145[b]	144	162	135	157	144
B'		4.4	4.0	3.7	3.6	3.6
c_{11}	193[b]	192				175
c_{12}	121[b]	122				129
c'[c]	36[b]	36				23
c_{44}	54[b]	56				106
c_{44}^0		149				
ζ		0.72				
wurtzite ($P6_3mc$), no. 186, B4						
E_c	−7.52	−7.52	−9.769	−7.692	−5.658	−39.92
V_0	23.61[d]	23.59	22.874	24.834	24.570	23.46
a	3.242[c]	3.219	3.199	3.292	3.290	3.268
c/a	1.6003[c]	1.6330	1.6138, 1.604	1.6076	1.593	1.553
u	0.3819[c]	0.3750	0.3790	0.3802, 0.381	0.3856	0.3920
B	136 – 183	146[e] (144[b])	162, 138, 160	134, 125	154	143
B'	3.6 – 4	4.4	4.1, 4.4	3.8	3.6	3.3
c_{11}	207, 210	212[e] (210[b])	209	230		236
c_{12}	121	116[e] (117[b])	85	82		112
c_{13}	106, 105	109[e] (108[b])	95	64		105
c_{33}	210, 211	219[e] (220[b])	270	247		188
c_{44}	43, 45	43[e] (41[b])	46	75		74
c_{66}[c]	45, 44	48[e] (47[b])	62	74		62

[a] due to restriction to first neighbors.
[b] calculated from the hexagonal/cubic elastic constants using Martin's transformation method (Reference [193]).
[c] cubic: $c' = (c_{11} - c_{12})/2$; hexagonal: $c_{66} = (c_{11} - c_{12})/2$.
[d] measured at 20 K, Reference [71].
[e] calculated directly.

Table 9.3.: *Summary of bulk properties of zinc oxide – continued from previous page.*

	Expt.	ABOP	Theory			LC
			LDA-DFT	GGA-DFT	HF	
rock salt ($Fm\bar{3}m$), no. 225, B1						
ΔE		0.237	0.158	0.237	0.242	0.095
a	4.271 – 4.283	4.275	4.229	4.345	4.225, 4.294	4.267
B	170 – 228	200	206, 205	173	203, 132	192
B'	3.5 – 4	4.7	3.9, 4.9	3.7	3.6, 3.8	3.7
cesium chloride ($Pm\bar{3}m$), no. 221, B2						
ΔE		0.976	1.307	1.358		1.555
a		2.642	2.624	2.705		2.605
B		218	194	157		216
B'		5.0	4.0	3.8		3.8

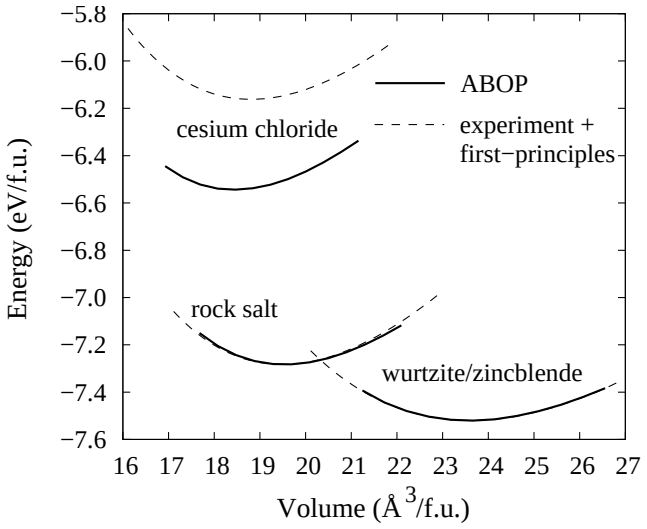

Figure 9.2: *Energy-volume curves for bulk structures of zinc oxide illustrating the good agreement between the analytic bond-order potential (ABOP) and the reference curves which were obtained by combining data from experiment and first-principles calculations. The transition pressure can be obtained from this plot by means of the common tangent construction which is equivalent to finding the crossing point of the enthalpy curves.*

curves shown in Fig. 9.2 one obtains the transition pressure for the wurtzite-rock salt transformation as 10 GPa in good agreement with experimental values in the range of 8.6 to 10 GPa as well as first-principles calculations predicting transition pressures between 8.6 and 14.5 GPa (see Ref. [199] and references therein).

The comparison also includes the shell-model potential by Lewis and Catlow (LC) [158, 159] which due to the incorporation of electrostatic interactions is computationally much more expensive than the ABOP. For the LC potential calculations the GULP code [181] was employed. The LC potential yields elastic constants in good agreement with experiment but reveals some deficiencies in the description of the equilibrium volumes and energies of the rock salt and zinc blende phases.

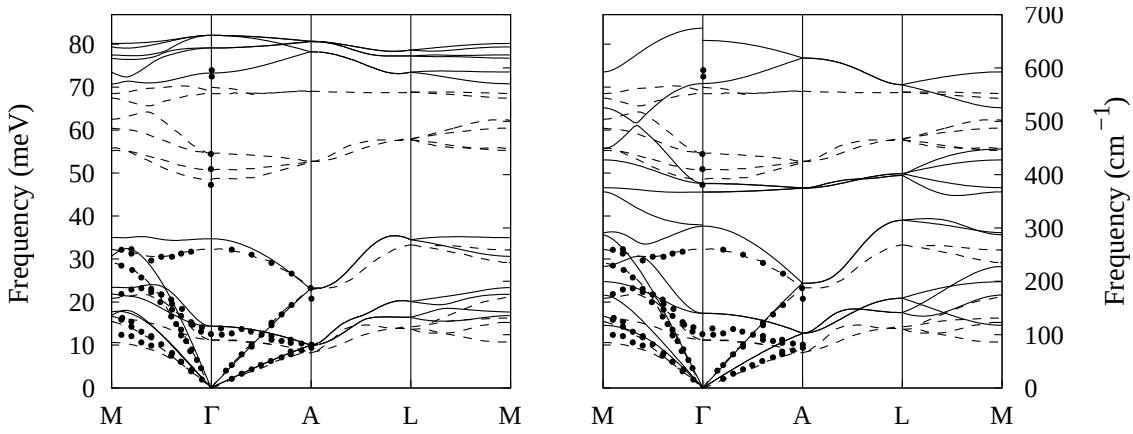

(a) analytic bond−order potential (b) Lewis−Catlow

Figure 9.3.: *Phonon dispersion relations for (a) the analytic bond-order potential (——) developed in the present work and (b) the shell-model potential by Lewis and Catlow. Dashed lines (- - - -) and black circles (•) show data from density functional theory calculations and experiment, respectively (Ref. [17] and references therein).*

As a final test, the phonon dispersion for wurtzite was evaluated (see Sec. A.2 for computational details) and compared with experiment and quantum mechanical calculations as shown in Fig. 9.3 (Ref. [17] and references therein). The ABOP shows a very good agreement with the experimental and first-principles data for the lower six branches of the dispersion relation. The deviations are somewhat larger for the LC potential but the overall agreement is still reasonable. On the other hand, the differences are more significant for the upper six (optical) branches. The LC potential yields qualitatively the correct shapes of these bands but fails to predict the phononic band gap and largely overestimates the splittings. In contrast, the ABOP underestimates the splitting of the bands but successfully predicts the existence of a phononic band gap. The shortcomings of both potentials in the description of the higher lying branches are related to an overestimation (LC) or respectively an underestimation (ABOP) of the ionicity of the bond and the atomic polarizabilities. In particular the very good description of the lower branches is encouraging with respect to the applicability of the ABOP.

9.4. Zinc

Since Zn–Zn interactions are practically absent in the compound, they have to be fitted independently of the Zn–O parameter set. Although the role of *d*-electrons is *per-se* not taken into account in the ABOP scheme (compare Chapter 7), it has turned out that the transition metals platinum [154] and tungsten [155] can be very well described within the ABOP framework. While this experience is encouraging with respect to fitting a similar potential for zinc, it must be acknowledged that the 3*d*-electrons in zinc have a much more pronounced effect on the bonding behavior than in platinum or tungsten most prominently embodied by the unusually large axial ratio of hcp-Zn. Keeping these considerations in mind, the aim is to obtain a physically meaningful parameterization to be used in conjunction with the Zn–O parameter set but not primarily intended to be employed for simulations of pure zinc. It should also be recalled that in the past attempts to model zinc using EAM and MEAM schemes have essentially failed [202, 203].

Within the ABOP scheme it turns out to be impossible to reproduce all properties equally well with a single parameter set. In particular due to the short range of the potential it is very difficult to reproduce the fcc-hcp energy difference (and thus the stacking fault energy) realistically. Therefore, a reasonable fit to the energies and equilibrium volumes of various structures was pursued accepting larger deviations in the elastic constants and the hcp axial ratio.

The fitting database comprised data from experiment and calculations. As information on low-coordinated structures is not available in the literature, additional density functional theory (DFT) calculations were performed on existing and hypothetical bulk phases as described in Sec. 9.9.1.

9.4.1. Dimer properties

The Zn_2 molecule is a van-der-Waals dimer with a very low binding energy on one side and a very large bond length on the other side. Since dispersion interactions are not taken into account in the ABOP scheme (compare equations (8.1), (8.3), and (8.2)), no attempt was made to fit the dimer properties; instead D_0 and r_0 were treated as adjustable parameters. The final values of $D_0 = 0.647\,\mathrm{eV}$ and $r_0 = 2.439\,\text{Å}$ are, however, comparable in magnitude to the Morse parameters describing the second excited state [204] $(4p)^1\Sigma_u^+$ (the first excited state is also of the van-der-Waals type). For this state *ab-initio* calculations yield bond

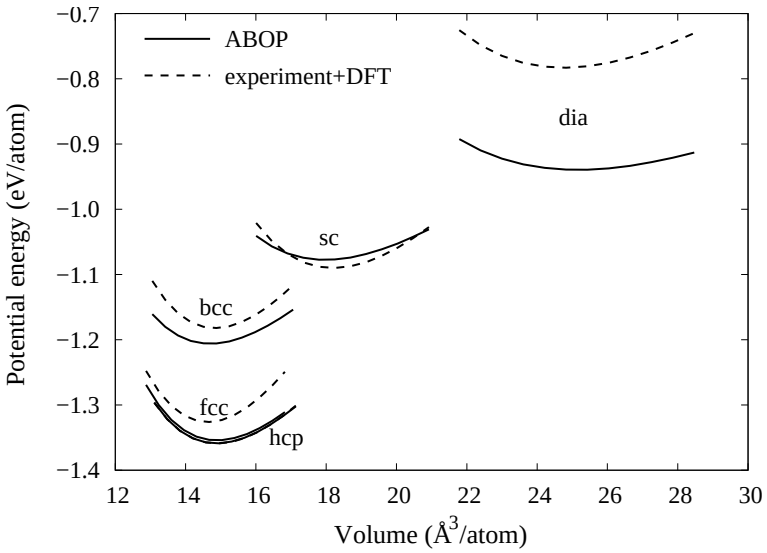

Figure 9.4: *Energy-volume curves for bulk structures of zinc as obtained from the analytic bond-order potential (ABOP) in comparison with reference curves which were obtained by combining data from experiment and density functional theory (DFT) calculations.*

energies between 1.00 and 1.13 eV (bond lengths between 2.65 and 2.97 Å), while values of 1.12 and 1.30 eV have been derived from experiment (bond length 3.30 Å, Ref. [204] and references therein).

9.4.2. Bulk properties

Table 9.4 provides an overview of the performance of the ABOP with respect to bulk properties in comparison with experiment and DFT calculations. The potential reproduces the energetics very well; the largest deviation from the DFT calculations occurs for the low coordinated diamond structure. The equilibrium volumina and bulk moduli are also in good overall agreement with the reference data as illustrated in Fig. 9.4.

The vacancy formation enthalpy and volume have been determined as 0.4 eV and $-0.3\,\Omega_0$ (Ω_0: atomic volume) which is in reasonable agreement with the experimental values of 0.5 eV and $-0.6\,\Omega_0$ [106]. For the interstitial a formation enthalpy of 2.7 eV and a formation volume of $1.7\,\Omega_0$ have been calculated. Experimentally, a formation volume of $3.5\,\Omega_0$ has been determined but the formation enthalpy is unknown.

9.4.3. Melting behavior

The melting behavior of elemental zinc has been investigated by means of molecular dynamics simulations of a solid-liquid interface [208]. The simulation cell contained 768 atoms. The system was equilibrated at zero pressure at temperatures between 0 and 1000 K for

Table 9.4.: *Summary of bulk properties of zinc as calculated using the analytic bond-order potential (ABOP) in comparison with experiment and density functional theory (DFT) calculations. Symbols as in Tab. 9.3 but energies and volumes are given in units per atom.*

	Expt.	**DFT**		**ABOP**
	Refs. [72, 205, 73, 206]	Ref. [207]	This work[a]	
hexagonal-close packed ($P6_3/mmc$, no. 194, A3)				
E_c	−1.359			−1.359
V_0	14.90[b]	14.53	14.90	14.88
a	2.660[a]	2.607	2.581	2.764
c	4.863[a]	4.937	4.791	4.498
c/a	1.8282[a]	1.8937	1.8563	1.627
B	73	78	(100[c])	73
B'	4.8		5.4	5.6
face-centered cubic ($Fm\bar{3}m$, no. 225, A1)				
ΔE		0.033	0.032	0.005
a		3.85	3.90	3.91
B		95	95	72
B'		4.2	5.1	5.6
body-centered cubic ($Im\bar{3}m$, no. 229, A2)				
ΔE		0.177	0.106	0.149
a		3.07	3.11	3.07
B		84	89	67
B'		5.1	5.2	5.5
diamond ($Fd\bar{3}m$, no. 227, A4)				
ΔE			0.576	0.419
a			5.72	5.86
B			40	25
B'			5.1	5.2
simple cubic ($Pm\bar{3}m$, no. 221, A_h)				
ΔE			0.270	0.281
a			2.54	2.62
B			65	43
B'			5.1	5.4

[a] see Sec. 9.9.1 for details.
[b] at 0 K as cited in Ref. [207].
[c] energy-volume curve obtained at fixed axial ratio, $c/a = 1.8563$.

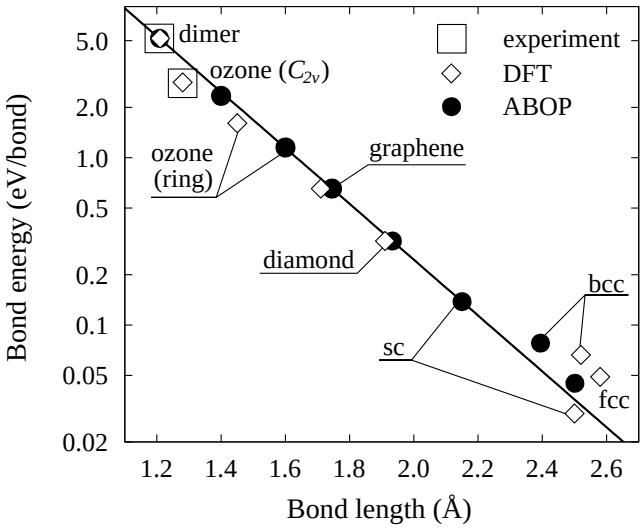

Figure 9.5: *Pauling plot for oxygen. The solid line illustrates the the Pauling relation while the symbols correspond to data from experiment, density functional theory (DFT) and the analytic bond-order potential (ABOP) calculations. The deviation of the ABOP data points from the Pauling plot for larger bond lengths is due to the penetration of the cutoff range ($R_c = 2.60\,Å$).*

at least 0.5 ns. Temperature and pressure were controlled using the Berendsen temperature and pressure controls [209] with coupling constants of 100 and 200 fs, respectively. For temperatures below 650 K and above 685 K either complete solidification or complete melting was observed while for intermediate temperatures the interface was stable for at least 2 ns. This observation agrees very well with the experimental melting point of 693 K.

9.5. Oxygen[‡]

In order to reproduce the O_2 molecule a simple pair potential would be sufficient but then the thermodynamically most stable phase would be a close-packed structure (either hexagonal or cubic). Here, a more general description of the bonding behavior of oxygen is pursued.

The fitting database comprised exeperimental data on the dimer and ozone molecules complemented by data from first-principles calculations (Sec. 9.9.2). The bond energy, bond length and oscillation frequency of the dimer fix the parameters D_0, r_0 and β. The bond angle of the ozone molecule determines h. Thus there are four parameter left to be fitted. The parameter set which gave the best overall agreement with the input data is given in Tab. 9.1. The properties calculated with the ABOP are compared in Tab. 9.5 to experiment and quantum mechanical calculations. Data sets are given for two different choices of

[‡]This section is based on a collaboration with N. Juslin and Prof. K. Nordlund at the University of Helsinki, Finland.

Table 9.5.: *Summary of properties of oxygen molecules and bulk phases calculated with the analytic bond-order potential (ABOP) in comparison with experimental data (Refs. [72]) and quantum mechanical (QM) calculations (Refs. [210, 211, 212, 213, 214]). E_c: cohesive energy (eV/atom), ΔE: energy difference with respect to oxygen dimer (eV/atom); r_b: bond length (Å); θ: bond angle of ozone molecule (deg); a: lattice constant (Å).*

	Expt.	**QM**		**ABOP**	
		Literature	This work[a]	$R_c = 2.1$ Å	$R_c = 2.6$ Å
Dimer					
r_b	1.21	1.22 – 1.25	1.21	1.21	
E_c	−2.58	−2.24 – −3.07	−2.85	−2.58	
Ozone, ground-state, C_{2v}					
r_b	1.28	1.27 – 1.39	1.28	1.35	1.40
θ	116.8	116.0		116.8	178.7
ΔE	0.49	0.48 – 0.67	0.47	0.50	0.83
Ozone, equilateral triangle (ring)					
r_b		1.45	1.45	1.60	
ΔE		0.90 – 1.13	0.98	1.43	
O_4 molecule					
r_b			1.80	1.81	
ΔE			2.26	1.81	
graphene sheet					
r_b			1.71	1.75	
ΔE			1.60	1.60	
diamond ($Fd\bar{3}m$, no. 227, A4)					
a			4.40	4.46	
ΔE			1.95	1.95	
simple cubic ($Pm\bar{3}m$, no. 221, A_h)					
a			2.50	2.07	2.15
ΔE			2.49	2.08	2.17
body-centered cubic ($Im\bar{3}m$, no. 229, A2)					
a			2.91	2.43	2.76
ΔE			2.32	2.12	2.27
face-centered cubic ($Fm\bar{3}m$, no. 225, A1)					
a			3.65	3.03	3.54
ΔE			2.29	2.14	2.31

[a] see Sec. 9.9.2 for details.

the cutoff parameter R_c. The first value ($R_c = 2.10\,\text{Å}$) reproduces the experimental data for the bond angle as well as the cohesive energy of the ozone molecule but the cohesive energies of the higher coordinated structures are systematically overestimated. The longer cutoff ($R_c = 2.60\,\text{Å}$) yields a superior description of the higher coordinated phases but sacrifices the ozone molecule. The good overall agreement of the oxygen-oxygen parameter set with the reference data is further illustrated by the Pauling plot shown for $R_c = 2.60\,\text{Å}$ in Fig. 9.5.

9.6. Point defects, thermal properties, and cutoff parameters

In chapters 4 and 5 it was shown that the geometries and the energetics of point defects in zinc oxide result from an intricate interplay of electronic effects leading to rather complicated configurations such as the oxygen dumbbell interstitials. The existence of many different stable charge states furthermore leads to a strong dependence of the formation enthalpies on the Fermi level. Obviously, these complications are impossible to capture in any analytic potential scheme, which owes its efficiency to the neglect of the electronic structure. For modeling of an ensemble of several hundred or thousand atoms, it is, however, usually sufficient to have a reasonable description of the energetics, while defect geometries play a minor role. Therefore, no attempt has been made to reproduce the defect structures obtained from quantum mechanical calculations with the analytic bond-order potential.

The analytic bond-order potential scheme used in the present work employs a cutoff function in order to scale the interaction to zero between the first and second nearest neighbor shells. Therefore, the cutoff parameters can be varied within a certain range without affecting the ground state properties considered during fitting (cohesive energies, lattice parameters, elastic constants). On the other hand, the cutoff parameters do affect other properties such as point defect formation enthalpies, melting behavior, or migration barriers. In the past the cutoff parameters of existing potentials have been occasionally modified in order to optimize them for certain applications, e.g., in the context of point defect properties [215, 177] or in the study of large volumetric deformations [216].

The ABOP developed in the foregoing sections was, therefore, tested with respect to variations of the cutoff parameters. The impact on point defect formation enthalpies can be rationalized as follows:

- The vacancy formation enthalpies are unaffected by the cutoff distances. The extent of relaxation around the vacant site is obviously insufficient for any of the participating atoms to enter the cutoff region and/or for atoms of the same type to interact.
- The introduction of surplus zinc atoms leads to direct Zn–Zn interactions whence the formation enthalpies of zinc interstitials and antisites are strongly dependent on the zinc cutoff distance. The dependence is typically monotonic but discontinuous. On the other hand their dependence on the oxygen cutoff distance is comparably small but usually continuous. The formation enthalpies of oxygen interstitials and antisites which involve oxygen surplus display the inverse behavior of their zinc-surplus counterparts.
- The formation enthalpies for oxygen-surplus defects are virtually independent of the Zn–O cutoff distance. On the other hand, the zinc-surplus defects display some variation which can, however, not be easily rationalized as the *dependence* on $R_c^{\mathrm{Zn-O}}$ itself is sensitive to the choice of $R_c^{\mathrm{Zn-Zn}}$ and $R_c^{\mathrm{O-O}}$.

These observations show that the formation enthalpies of zinc and oxygen-surplus point defects (in high-symmetry positions) to some extent can be controlled independently. Vacancies are, however, exempt from this possibility as their formation enthalpies are independent of the cutoff distances. Note that since the ABOP is an atomistic model, it cannot capture the Fermi level dependence of the formation enthalpies of charged defects (see Sec. 4.2.2, Chapter 4, and Chapter 5).

Zinc oxide does not melt congruently but dissociates into liquid zinc and gaseous oxygen. Therefore, the melting point cannot be obtained from simulations of a liquid-solid interface (compare Sec. 9.4.3 and Ref. [208]). Simulations of single-crystalline ZnO cells, however, show qualitatively an increase of thermal stability with increasing Zn–O cutoff distance.

In Tab. 9.1 a set of cutoff parameters is given suitable for simulations of compound systems, which has been tested in a variety of simulations and which has also been used for the applications presented below. Before the present potential is used in any simulation, it is nonetheless advisable to consider the effect of the cutoff parameters explicitly with respect to the application in mind.

9.7. Irradiation of bulk zinc oxide[§]

The behavior of materials under irradiation with energetic particles has been studied for many decades [217, 218]. It is of major technological and fundamental importance: For instance, in the semiconductor industry ion beams are beneficially used for dopant implantation, surface structuring and to assist film deposition. In nuclear engineering, on the other hand, it is essential to understand the detrimental effects of intense ion bombardment on the performance of reactor components. In physics and materials research energetic particles are used as analytic probes and exploited as a powerful tool to investigate the fundamental aspects of defects in solids (see discussion in Chapter 6 and Refs. [111, 132, 219]). Since irradition with energetic particles is an efficient and controllable method to drive system far from equilibrium, it also allows to study for instance the formation and the properties of metastable materials.

Since the kinetic energy of a particle impacting on a target is deposited in a small volume (some ten nm^3) during a very short period of time (some picoseconds), very large energy densities are obtained. Such extreme conditions can induce defect concentrations, which exceed the equilibrium concentration by orders of magnitude, and eventually can lead to local melting or amorphization. As indicated above, particle irradiation can have both advantageous and detrimental effects. It is, therefore, crucial to obtain a detailed understanding of the processes during ion bombardment. Molecular dynamics (MD) simulations (see Sec. A.1) in conjunction with analytic potentials have proven to be a very effificient and powerful tool in this field of research [217, 218]. Simulations of ion irradition are also a stringent test for the applicability and transferability of a potential, since they sample far-from-equilibrium configurations, which cannot be easily included in the fitting process, and can furthermore reveal artificial minima of the potential function.

The threshold displacement energy measures which kinetic energy given to a lattice atom in a certain direction is required in order to produce at least one stable lattice defect [218, 220]. It is a fundamental quantity in irradiation physics, and the first step towards understanding the extent and kind of damage produced by any kind of energetic particle irradiation of a lattice [217]. The definition of this quantity is, however, not unique since the probability to produce a defect does not always rise steeply from zero to one at a certain energy [220]. For a more profound understanding one needs to analyze the integrated

[§]This section is based on a collaboration with Prof. K. Nordlund at the University of Helsinki, Finland.

displacement probability function [221], i.e. the probability to form a defect at a given energy. In order to determine this function for zinc oxide, molecular dynamics simulations were carried out employing the analytic bond-order potential derived in this chapter (see also Ref. [219]).

Firstly, a cell with 2280 atoms was equilibrated at 5 K and zero pressure. Then a randomly chosen atom near the center of the cell was assigned a velocity in a randomly chosen direction equivalent to the recoil energy. The evolution of the system was followed for 6 ps. For each recoil atom and direction the energy was successively raised starting from 4 eV in steps of 4 eV until a defect was found. About one thousand O and Zn (atom type and direction) combinations were simulated. Since some threshold experiments were carried out with electron irradiation on single crystal samples in the *c*-axis direction, another set of simulations was carried out with recoils directed along the positive ("Zn face") *c*-axis direction, assuming an electron beam angular spread of 15 degrees about the [0001] direction. Due to the 4 eV step size all threshold values reported below have an uncertainty of ±2 eV.

Voronoy polyhedron defect analysis centered on the perfect atom sites was used to determine whether a defect had formed at the end of the simulation [222]. Both Voronoy interstitials and vacancies as well as antisites were counted as defects. In addition, if the final energy of the cell was at least 3.7 eV (the minimum energy to form a Frenkel pair) higher than the initial one, a defect was assumed to have formed as well. Fig. 9.6 shows the integrated displacement probability function [221], i.e. the probability to form a defect at a given energy considering all (atom and direction) combinations which were simulated. The figure shows that although the minimum threshold energy is about the same for both Zn and O recoils, the defect production efficiency increases much more slowly for O recoils. The defect production probabilities for Zn recoils along arbitrary directions and for recoils along the *c*-axis are similar.

Threshold values for Zn recoils of 57 eV at 313 K [223] and 56 eV at 5 K [224] have been determined from electron irradiation experiments. These studies were carried out on ZnO single crystals in the *c*-axis direction. More recently using ion irradiation an effective upper limit threshold for Zn recoils of 65 eV was determined [131]. In electron irradiation experiments the high energy data is fit to a linear function and the threshold energy is obtained as the intersection with the energy axis. Since at energies clearly above the threshold, the overall damage production is determined by the average threshold

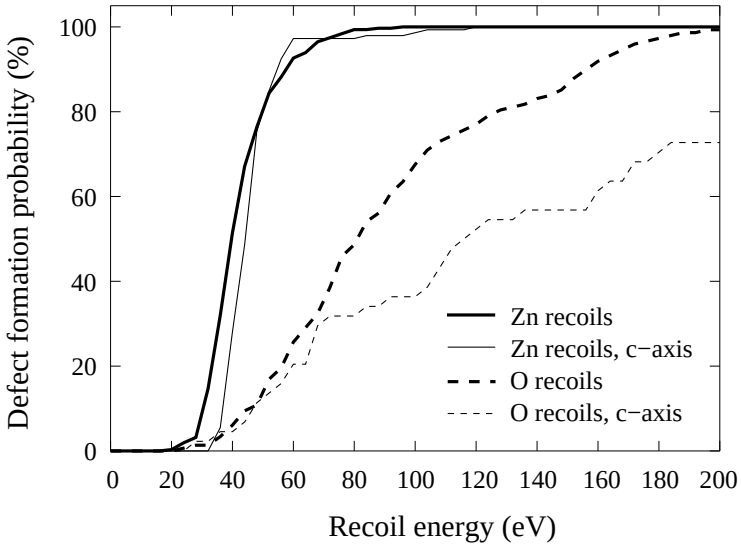

Figure 9.6: *Probability to form a defect during a recoil event in ZnO as a function of energy. Note that the data illustrates specifically the probability to form at least one defect; of course at higher energies in many cases more than one defect is formed.*

displacement energy, the electron irradiation threshold is most appropriately compared to the average threshold energy. Note that in Ref. [224] the actual defect production data is clearly higher than the linear fit to the lowest data points, which can be regarded as an indication for a small defect production probability even below the average threshold, consistent with the observations in the simulations. The present simulations give an average threshold energy of 42 eV for all directions, and 45 eV along the c-axis direction. These values are thus in reasonable agreement with the experimental values of <65 eV [131] and 56–57 eV [223, 224], respectively.

For oxygen recoils the experimental data is more difficult to interpret. Optical absorption methods have not detected any defects which can be attributed to the oxygen threshold [224] (the threshold energy interpretations reported in [225] were later disputed [223]). Electron paramagnetic resonance and electrical measurements have detected an onset of damage at 310 keV electron energy, corresponding to an oxygen recoil energy of 55 eV [223]. It should be noted, however, that the maximum electron irradiation energy in this experiment was only about 680 keV, corresponding to an O recoil energy of 155 eV. This signal may thus be related to the low fractional defect production probabilities observed in the simulations for oxygen recoils in the energy range 20–155 eV.

9.8. Conclusions

An analytic bond-order potential for zinc oxide was derived which describes ZnO as a predominantly covalently bonded system. It, thereby, represents the counterpart to earlier potentials for this material which focused on the ionic character of the Zn–O bond. Since the interatomic potential developed in this work is short-ranged it is computationally more efficient than ionic potentials which require the evaluation of long-ranged Coulombic interactions. The neglect of charges has some drawbacks in the sense that explicit electrostatic effects which play a role for example at surfaces due to unscreened charges cannot be captured. Otherwise the ABOP provides a very good description of many properties of zinc oxide.

The Zn–O parameterization is complemented by parameter sets for the elemental phases of zinc and oxygen. The zinc potential yields a good description of the coordination dependence of the cohesive energies. Structural and elastic properties are somewhat less well described. The oxygen potential is capable of describing oxygen molecules as well as several hypothetical bulk phases. Thereby, the present potential is applicable in simulations which require a thermodynamic model for the entire Zn–O system. The transferability of the potential has been demonstrated in one exemplary case, namely the determination of threshold displacement energies. The potential is suitable for simulating a variety of processes and phenomena including e.g., the growth of thin films, the properties of nanocrystalline zinc oxide, or the mechanical behavior of zinc oxide nanostructures such as rings, wires, and belts.

9.9. Appendix: Total energy calculations

In order to apply the fitting strategy outlined previously (Chapter 8), the energy differences and bond lengths of various bulk structures with different coordinations have to be included in the fitting database. For zinc oxide a broad data basis is available but for zinc and oxygen, further input was required.

9.9.1. Zinc

Singh and Papaconstantopoulos [207] calculated cohesive energies and lattice parameters of the face-centered cubic (fcc), body-centered cubic (bcc) and hexagonal-close packed (hcp)

structures based on DFT calculations using the linearized-augmented plane waves (LAPW) method. These data were complemented with plane wave pseudopotential (PWPP) calculations on the lower coordinated simple cubic (sc) and diamond (dia) structures.

The calculations were carried out within the local-density approximation (LDA) in the Teter-Pade parameterization [68] using the PWPP code ABINIT [69, 70]. The norm-conserving pseudopotentials due to Troullier and Martins [60] were employed including the 3*d*-electrons as part of the valence. A plane wave cutoff energy of 70 Hartree was used. Brillouin zone sampling was performed employing 572 (hcp), 570 (fcc), 240 (bcc), 570 (dia) and 220 (sc) k-points distributed on shifted Monkhorst-Pack meshes which yields a convergence better than 1 meV/atom. The calculated energy-volume curves shown in Fig. 9.4 were fitted to the Birch-Murnaghan equation of state [108]. The results are summarized in Tab. 9.4. The agreement with experimental data and previous theoretical work is very good. The systematic underestimation of the lattice constants as compared to experiment is a well know deficiency of the LDA.

9.9.2. Oxygen[¶]

A wealth of experimental as well as theoretical data is available for the O_2 and O_3 molecules (see e.g., Refs. [72, 210, 211, 212, 213, 214]). Additional calculations were performed on higher coordinated molecules and bulk structures. The CASTEP code [226, 227] was used to perform DFT calculations within the spin polarized generalized gradient approximation (GGSA) based on the Perdew-Wang parameterization [25] (PW91), and the Gaussian94 code [228] for DFT calculations using the BLYP [52] and B3LYP [53] functionals as well as for Hartree-Fock calculations. Preliminary tests proved the GGSA-PW91 DFT method to be reliable whence it was selected for the further computations.

For the calculations ultrasoft pseudopotentials were used employing a plane wave cutoff energy of 380 eV (norm-conserving pseudopotentials were also considered and gave basically identical results); finite basis set corrections were included to compensate for imperfect Brillouin zone sampling. The number of k-points was chosen to obtain convergence of the total energy better than 15 meV/atom. Using these parameters the relaxed structures and cohesive energies of several molecules and bulk structures were computed. In the case of the

[¶]This section is based on a collaboration with N. Juslin and Prof. K. Nordlund at the University of Helsinki, Finland.

O_3 molecule the ground state as well as the equilateral triangle geometry, which is known to be a local minimum on the potential energy surface (see e.g., Ref. [214]), were considered. For the O_4 molecule the tetrahedron geometry was considered. The higher-coordinated structures comprised graphene as well as diamond, sc, bcc, and fcc. The data is shown in Tab. 9.5. Where comparison is possible the DFT data computed in the present work is in very good agreement with experiment and previous quantum mechanical calculations.

Conclusions

The present dissertation combines quantum mechanical and atomistic simulation techniques with thermodynamic concepts to elucidate both static and dynamic properties of intrinsic point defects in zinc oxide.

In the first part, by using quantum mechanical calculations based on density functional theory, it has been shown that in the ground state oxygen interstitials assume dumbbell configurations and can occur both in negative as well as positive charge states depending on the Fermi level. This extends considerably the established picture, which presumes oxygen interstitials to be acceptors occupying highly symmetric octahedral interstitial sites. The oxygen vacancy displays significant geometric relaxation as the charge state varies, compatible with a deep-level character.

The shortcomings due to an insufficient treatment of the Zn-3d levels within the local density (LDA) and generalized gradients (GGA) approximations as well as the limitations of the supercell approach have been remedied by applying semi-empirical self-interaction corrections (GGA+U scheme) and extensive finite-size scaling. In comparison to earlier works, the reliability of the calculated formation enthalpies and transition levels is significantly improved. In addition, point defect formation volumes are derived, which have not been considered in zinc oxide so far.

In the past, experimental studies on the self-diffusion in zinc oxide provided very scattered data and did not succeed in resolving the character of the diffusing species. In the present work, by combining density functional theory calculations with thermodynamic principles this long standing issue has been resolved. For oxygen, vacancy and interstitialcy mechanisms dominate under zinc and oxygen-rich conditions, respectively. This finding refutes the belief that oxygen vacancy mechanisms can be operational in experiments in oxygen-rich atmosphere under equilibrium conditions. With regard to the diffusion of zinc

it has been demonstrated that zinc interstitials are mobile down to very low temperatures. In contradiction to intuition, they do not migrate via an interstitial mechanism along the hexagonal channels of the wurtzite lattice but through an interstitialcy mechanism involving second nearest neighbors.

The PONTIFIX computer code, which has been developed in this work, provides a flexible and powerful method to derive parameter sets for the analytic bond-order potential scheme due to Abell, Tersoff, and Brenner. The code supports a variety of structures with cubic, hexagonal and tetragonal symmetry, allows to include an arbitrary number of neighbor shells, and can handle several parameter sets simultaneously. Thanks, to its generality it has also been applied to develop analytic bond-order potentials for other systems such as Si–C, W–C–H, and Fe–Pt. In the present work, PONTIFIX has been used to develop interatomic potentials for the Zn–O system, which are capable of describing the changes in the bonding characteristics with variable coordination. This demonstrates that even a non-ionic model can provide a remarkable good description of the properties of a partially ionic compound such as zinc oxide, which has been exemplified by simulations on the defect production by ion irradiation. Since the analytic bond-order potential has been validated with respect to a broad range of properties, it is well-suited to study a variety of phenomena including e.g., thin film growth, mechanical deformation of single and polycrystalline material mechanical behavior of nano-sized structures such as wires, belts or pillars.

In summary, the present study contributes to the understanding of the structural, electronic, thermodynamic, and kinetic properties of intrinsic point defects in zinc oxide. The results provide the basis for the interpretation and reinterpretation of experiments, and pave the way towards the development of reliable continuum models for device simulation.

Outlook

It has been demonstrated that density functional theory provides a robust framework which does not only allow to study the geometrical and electronic structure but also to derive thermodynamic or even kinetic quantities. The approach which has been pursued in the present study, is, therefore, currently being applied to other oxide materials such as barium titanate and tin-doped indium oxide.

With respect to zinc oxide, there are still many aspects which deserve further investigation: In the present study of point defects entropic effects were entirely neglected based on the argument that – compared to the energy – the entropy term represents a secondary contribution to the free enthalpy (see Sec. 4.2.2 and Sec. 6.2). It would be interesting to determine the entropies of formation and migration in order to validate this presumption and to improve the quantitative reliability of the first-principles data. To this end, one would need to compute the spectrum of vibration frequencies using e.g., the dynamical matrix approach (see Sec. A.2 and Ref. [78]). If the eigenfrequency spectra for both the ground and the transition state are known, it is furthermore straight-forward to calculate the attempt frequency (Γ_0 in equation (6.7)) by means of the Vineyard equation [126].

While the ideal surfaces of zinc oxide have already been explored theoretically in some detail [12, 229, 230, 231, 232, 233], little is known about the interaction between surfaces and defects and in particular the mechanisms by which defects are incorporated or removed. In this respect, it is also of interest to investigate the interaction of various atomic and molecular species with surfaces. Since zinc oxide possesses both polar and non-polar surfaces with different terminations, intriguing interactions between surface dipoles and defect induced multipoles can be expected.

Already several first-principles studies addressed the role of extrinsic defects in zinc oxide (e.g., H [63, 234, 235], N [21, 83, 84], Li [122], Mn, Co [236]), predominantly with the in-

tention to provide explanations and solutions for the difficulties to grow p-type zinc oxide. Still many open questions remain, in particular it would be instructive to study the formation of defect complexes, also taking into account the oxygen interstitial configurations discussed in Chapter 4, and to include a larger variety of dopants – most importantly Al, Ga, and As. One would need to characterize the electronic structure of these impurities as well as the defect induced transition levels. It has been demonstrated for the case of Li that different sites are preferred depending on the charge state and thus on the Fermi level. In this context the role of the *d*-electrons of both Zn and the dopant species deserves special attention. The next step would be to derive the mobilities of the individual defects and elucidate the effect of complex formation.

It is also worthwhile to consider the interfaces in zinc oxide. Starting from high-symmetry grain boundaries it would be desirable to develop a profound understanding of the structure and the distribution of grain boundaries, which would have implications especially with respect to the understanding of nanocrystalline zinc oxide. In this respect, the analytic bond-order potential developed in this work would be helpful. By opposing the results obtained with the purely covalent analytic bond-order model with purely ionic potentials [237, 135], one could furthermore obtain insights into the competition between covalent and ionic bonding. Similarly, analytic interatomic potentials could be used to study various nanostructures of zinc oxide. The first studies in this direction have been published recently [238, 239].

For most of the problems outlined above experiments can provide only very indirect if any insight. One possible route has been demonstrated for hydrogen in ZnO: First-principles calculations [235] have shown that the vibrational modes of different configurations for the hydrogen interstitial are differentiated by their pressure dependence. By monitoring the pressure dependence of vibrational modes by means of Raman spectroscopy it was, thereby, possible to reveal the actual position of hydrogen in ZnO. For intrinsic defects such an approach is impractical because the vibrational modes of intrinsic defects can practically not be isolated from the regular modes. On the other hand, it might be possible a similar strategy for dopants with small atomic mass.

As described in Chapter 5, knowledge of the formation volumes and energies allows to derive the pressure dependence of the transition levels and the defect concentrations. Based on the calculations, different trends for the pressure dependence of the transition levels of the oxygen vacancy and the zinc interstitial were obtained. It would be very interesting

to test this prediction experimentally. Furthermore, it could be fruitful to explore the possibilities for controlling defect concentrations via application of stress.

A. Appendix: Methods

This chapter gives a concise description of the molecular dynamics simulation technique and the determination of phonon dispersion relations using dynamical matrices and the harmonic approximation. Finally, the external codes utilized in this work are summarized.

A.1. Molecular dynamics simulations

Studying the dynamics of an ensemble of atoms (or more general point-like particles) is equivalent to finding solutions of Newton's equation $\boldsymbol{F} = m\boldsymbol{a}$. The mutual dependence of the atomic trajectories is described by a set of coupled differential equations

$$m_i \frac{\partial^2 \boldsymbol{r}_i}{\partial t^2} = \boldsymbol{F}_i \left(\{\boldsymbol{r}_j\} \right), \qquad i = 1 \ldots N, \tag{A.1}$$

where m_i and $\boldsymbol{r}_i$ are the mass and position of particle i and $\boldsymbol{F}_i$ is the force acting on it. For more than three atoms ($N > 3$) analytical solutions do not exist and one must resort to a numerical method. The scheme, which, for historical reasons, is known as molecular dynamics [240] (MD), discretize the set of equations (A.1) and solves them iteratively using a small finite increment Δt (the timestep). The principle steps in a MD simulation are shown in the flow chart of Fig. A.1.

The most important input to any MD simulation is the force field which is obtained as the gradient of the scalar potential

$$\boldsymbol{F}_i \left(\{\boldsymbol{r}_j\} \right) = -\nabla_{\boldsymbol{r}_i} V \left(\{\boldsymbol{r}_j\} \right). \tag{A.2}$$

Density functional theory (DFT, Chapter 3) or tight-binding (TB) schemes provide the most accurate and reliable energies but they are computationally very expensive. Therefore, analytic potentials, which are computationally much more efficient, are employed the most often. A detailed review of analytic potential schemes is given in Chapter 7.

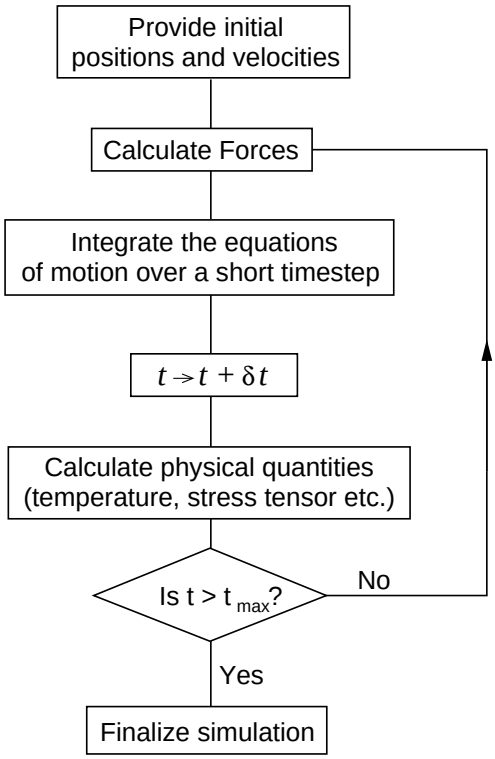

Figure A.1: *Flow chart showing the most important steps during a molecular dynamics simulation.*

A.2. Phonon dispersion relations

The phonon dispersion describes the distribution of phonon frequencies over the phonon wave vectors in the irreducible wedge of the Brillouin zone. Experimentally, phonon dispersion relations are typically measured by Raman and infrared (IR) spectroscopy as well as neutron scattering. Theoretically, the most common methods are the frozen phonon and the dynamical matrix [241] approach. In the present work, the latter method was employed.

Essentially, the calculation of phonon dispersion relations from dynamical matrices can be split into three parts: (1) At first, the force constant matrix is evaluated. It is defined as the mixed derivative of the energy with respect to atomic displacements, $u_{i\alpha}$

$$\Phi_{\Pi i\alpha,\Phi j\beta} = \frac{\partial^2 E}{\partial u_{i\alpha} \partial u_{j\beta}} \tag{A.3}$$

where Π and Φ denote the cell index, i and j denote atoms in the primitive unit cell, and α and β label the Cartesian directions. (2) Then, the dynamical matrix $\mathbf{D}_{i\alpha,j\beta}$ at the wave

vector $\boldsymbol{q}$ is obtained by summation over all unit cells and Fourier transformation of the force constant matrix according to [241]

$$\mathbf{D}_{i\alpha,j\beta} = \sum_{\Pi} \sum_{\Phi} \Phi_{\Pi i\alpha,\Phi j\beta} \exp[i\boldsymbol{q}(\boldsymbol{r}_{\Pi i\alpha} - \boldsymbol{r}_{\Phi j\beta})]. \tag{A.4}$$

(3) Finally, the dynamical matrix is diagonalized. The eigenvalues are the desired phonon frequencies at the respective wave vector.

As part of the present work a code was developed which implements this scheme for several analytic potential schemes including analytic bond-order and embedded atom method potentials.

A.3. Overview of external codes

A.3.1. Abinit

Abinit implements the plane wave-pseudopotential (PWPP) approach to density functional theory (DFT). It relies on an efficient Fast Fourier Transform algorithm [242] for the conversion of wavefunctions between real and reciprocal space, on the adaptation to a fixed potential of the band-by-band conjugate gradient method [57] and on a potential-based conjugate-gradient algorithm for the determination of the self-consistent potential [243]. The Abinit code was used in generating the results presented in Sec. 9.9 and Chapter 4. The Abinit code is a common project of the Université Catholique de Louvain, Corning Incorporated, and other contributors (`http://www.abinit.org`).

A.3.2. Vasp

The Vienna ab-initio simulation package (Vasp) [103] is another implementation of the PWPP approach to DFT. It features ultrasoft pseudopotentials [61] and the projector augmented plane wave (PAW) method [62, 104]. G. Henkelman, H. Jónsson, and coworkers [129] implemented a number of additional algorithms into Vasp which permit to employ e.g., the nudged elastic band [124, 125] (NEB) or the dimer [128] method. Results obtained using the Vasp code are shown in Chapter 5 and Chapter 6. Vasp was coded by G. Kresse and J. Furthmüller at the University of Vienna and is commercially distributed.

A.3.3. Gulp

The general utility lattice program (GULP) implements various analytic force fields and potentials. It provides capabilities for performing structure optimization as well as molecular dynamics simulations. GULP was used to perform benchmark calculations with the shell-model potential by Lewis and Catlow [159] as reported in Sec. 9.3.2. GULP was developed by J. Gale at the Imperial College, London. The code is available free of charge for researchers in academic environments.

Danksagung – Acknowledgments

Ohne die Hilfe einer ganzen Reihe von Menschen wäre mir die Erstellung der vorliegenden Arbeit nicht möglich gewesen.

Insbesondere möchte ich mich bei Professor Karsten Albe für das Thema und den Titel dieser Arbeit, sein Vertrauen und seine kontinuierliche Unterstützung während der letzten Jahre bedanken.

Bei Professor von Seggern bedanke ich mich für die Übernahme des Koreferats.

Meinen Eltern gilt ebenso mein Dank wie meiner Schwester Lisa. Min flickvän Petra Träskelin tackar jag för hennes förtrösta, stöd och motivation.

Dr. Andreas Klein schulde ich Dank ich für wichtige Anregungen und zahlreiche hilfreichen Diskussionen.

Kai Nordlund and Niklas Juslin contributed to sections 6.4 and 9.7 of this work and have warmthly hosted me at the University of Helsinki.

I am very grateful to Eduardo Bringa, Babak Sadigh and Vasily Bulatov at Lawrence Livermore National Laboratory for their continuous interest and support throughout the last four years.

Bei Michael Müller sowie die Mitgliedern des Gemeinschaftslabors Nanomaterialien und der ehemaligen Arbeitsgruppe „Dünne Schichten" Thorsten Enz, Jens Ellrich, Hermann Sieger, Holger Schmitt, Sebastian Gottschalk, Johannes Seydel und Renate Hernichel bedanke ich mich für viele Mittagessen, Kaffeepausen, Diskussionen und gemeinsame Abende. Ebenso gilt Nina Balke, Johannes Luschitz, Verena Liebau-Kunzmann, Ralf Theissmann und Jean-Christophe Jaud mein Dank für verschiedene Gelegenheiten, die Arbeit in den richtigen Zusammenhang zu stellen.

I also would like to thank G. Henkelman, H. Jónsson, and coworkers for kindly providing their VASP extensions (`http://theory.cm.utexas.edu/henkelman`).

This work was funded by the *Sonderforschungsbereich 595* "Fatigue in functional materials" of the *Deutsche Forschungsgemeinschaft*. The project was partially supported through a bilateral travel program funded by the German foreign exchange server (DAAD). Generous grants of computer time by the Center for Scientific Computing at the Johann Wolfgang Goethe-University, Frankfurt/Main are gratefully acknowledged.

Erklärung – Disclaimer

Die vorliegende Arbeit wurde im Zeitraum von August 2003 bis Mai 2006 im Fachgebiet Materialmodellierung am Institut für Materialwissenschaft der Technischen Universität Darmstadt bei Herrn Prof. Dr. rer. nat. Karsten Albe angefertigt.

Hiermit versichere ich an Eides statt, daß ich die vorliegende Arbeit selbstständig und nur unter Verwendung der angegebenen Hilfsmittel angefertigt habe. Von mir wurde weder an der Technischen Universität Darmstadt noch an einer anderen Hochschule ein Promotionsversuch unternommen.

Darmstadt, den 18. Mai 2006

Paul Erhart

Curriculum Vitae

Education

High School Graduation (*Abitur*),
Heinrich-Mann-Schule, Dietzenbach, Germany, May 1997

Academic year,
University of Illinois, Urbana-Champaign, USA, August 2001–June 2002

Diploma in Materials Science and Engineering (*Dipl.-Ing.*),
Technische Universität Darmstadt, Germany, June 2003

Research experience

Research assistant (20 months),
Technische Universität Darmstadt, Germany, 2000–2003

Research assistant (10 months),
University of Illinois, Urbana-Champaign, 2001–2002

Scholar of Computational Materials Science and Chemistry Summer Institute,
Lawrence Livermore National Laboratory, USA, June 2002–August 2002

Visiting scientist (3 months),
Lawrence Livermore National Laboratory, July 2003–August 2003, April 2004

Visiting scientist (4 months),
University of Helsinki, several visits since October 2002

Research scientist, PhD student,
Technische Universität Darmstadt, Germany, since August 2003

Publications based on the present dissertation

1. P. Erhart and K. Albe, *Pontifix/Pinguin: A program package for fitting interatomic potentials of the bond-order type*, submitted to Comp. Mater. Sci.
2. P. Erhart, N. Juslin, O. Goy, K. Nordlund, R. Müller and K. Albe, *Analytic bond-order potential for atomistic simulations of zinc oxide*, J. Phys. Condens. Matter. **18**, 6585 (2006).
3. P. Erhart and K. Albe, *Diffusion of zinc vacancies and interstitials in zinc oxide*, Appl. Phys. Lett. **88**, 201918 (2006).
4. P. Erhart, K. Albe and A. Klein, *First-principles study of intrinsic point defects in ZnO: Role of band structure, volume relaxation and finite size effects*, Phys. Rev. B **73**, 205203 (2006).
5. P. Erhart and K. Albe, *First-principles study of migration mechanisms and diffusion of oxygen in zinc oxide*, Phys. Rev. B, **73**, 115207 (2006).
6. P. Erhart, A. Klein, and K. Albe, *First-principles study of the structure and stability of oxygen defects in zinc oxide*, Phys. Rev. B **72**, 085213 (2005).

Other publications

1. P. Träskelin, N. Juslin, P. Erhart, and K. Nordlund, *Hydrogen bombardment simulations of tungsten-carbide surfaces*, submitted to Phys. Rev. B.
2. N. Juslin, P. Erhart, P. Träskelin, J. Nord, K. Henriksson, E. Salonen, K. Nordlund, and K. Albe, *Analytical interatomic potential for modeling nonequilibrium processes in the W–C–H system*, J. Appl. Phys. **98**, 123520 (2005).
3. P. Erhart and K. Albe, *Molecular dynamics simulations of gas phase condensation of silicon carbide nanoparticles*, Adv. Eng. Mater. **10**, 937 (2005).
4. L. P. Davila, P. Erhart, E. M. Bringa, M. A. Meyers, V. A. Lubarda, M. S. Schneider, R. Becker, and M. Kumar, *Atomistic modeling of shock-induced void collapse in copper*, Appl. Phys. Lett. **86**, 161902 (2005).
5. P. Erhart, E. Bringa, M. Kumar, and K. Albe, *Atomistic mechanism of shock-induced void collapse in nanoporous metals*, Phys. Rev. B **72**, 052104 (2005).
6. P. Erhart and K. Albe, *Analytical potential for atomistic simulations of silicon, carbon and silicon carbide*, Phys. Rev. B **71**, 035211 (2005).

7. E. Bringa, J. U. Cazamias, P. Erhart, J. Stölken, N. Tanushev, B. D. Wirth, R. E. Rudd, and M. J. Caturla, *Atomistic shock Hugoniot simulation of single-crystal copper*, J. Appl. Phys., **96**, 3793 (2004).

8. P. Erhart and K. Albe, *The role of thermostats in modeling vapor phase condensation of silicon nanoparticles*, Appl. Surf. Sci. **226**, 12 (2004).

9. J. Nord, K. Albe, P. Erhart and K. Nordlund, *Modelling of compound semiconductors: Analytical bond-order potential for gallium, nitrogen and gallium nitride*, J. Phys.: Condens. Matter **15**, 5649 (2003).

Bibliography

[1] P. Erhart and K. Albe, *Pontifix/Pinguin: A program package for fitting interatomic potentials of the bond-order type*, submitted to Comp. Mater. Sci., `http://www.mm.mw.tu-darmstadt.de/`.

[2] P. Erhart, N. Juslin, O. Goy, K. Nordlund, R. Müller and K. Albe, *Analytic bond-order potential for atomistic simulations of zinc oxide*, J. Phys.: Condens. Matter **18**, 6585 (2006).

[3] P. Erhart and K. Albe, *Diffusion of zinc vacancies and interstitials in zinc oxide*, Appl. Phys. Lett. **88**, 201918 (2006).

[4] P. Erhart, K. Albe and A. Klein, *First-principles study of intrinsic point defects in ZnO: role of band structure, volume relaxation and finite size effects*, Phys. Rev. B **73**, 205203 (2006).

[5] P. Erhart and K. Albe, *First-principles study of migration mechanisms and diffusion of oxygen in zinc oxide*, Phys. Rev. B **73**, 115207 (2006).

[6] P. Erhart, A. Klein and K. Albe, *First-principles study of the structure and stability of oxygen defects in zinc oxide*, Phys. Rev. B **72**, 085213 (2005).

[7] K. Ellmer, *Magnetron sputtering of transparent conductive zinc oxide: relation between the sputtering parameters and the electronic properties*, J. Phys. D **33**, R17 (2000).

[8] D. C. Look, B. Claflin, Y. I. Alivov and S. J. Park, *The future of ZnO light emitters*, Phys. Status Solidi A **201**, 2203 (2004).

[9] U. Özgür, Y. I. Alivov, C. Liu, A. Teke, M. Reshchikov, S. Doğan, V. Avrutin, S. J. Cho and H. Morkoç, *A comprehensive review of ZnO and related devices*, J. Appl. Phys. **98**, 041301 (2005).

[10] Z. W. Pan, Z. R. Dai and Z. L. Wang, *Nanobelts of Semiconducting Oxides*, Science **291**, 1947 (2001).

[11] M. H. Huang, S. Mao, H. Feick, H. Yan, Y. Wu, H. Kind, E. Weber, R. Russo and P. Yang, *Room-Temperature Ultraviolet Nanowire Nanolasers*, Science **292**, 1897 (2001).

[12] J. E. Jaffe, N. M. Harrison and A. C. Hess, *Ab-initio study of ZnO* $(10\bar{1}0)$ *surface relaxation*, Phys. Rev. B **49**, 11153 (1994).

[13] G. Kresse, O. Dulub and U. Diebold, *Competing stabilization mechanism for the polar ZnO(0001)-Zn surface*, Phys. Rev. B **68**, 245409 (2003).

[14] J. E. Jaffe and A. C. Hess, *Hartree-Fock study of phase changes in ZnO at high pressure*, Phys. Rev. B **48**, 7903 (1993).

[15] J. E. Jaffe, J. A. Snyder, Z. Lin and A. C. Hess, *LDA and GGA calculations for high-pressure phase transitions in ZnO and MgO*, Phys. Rev. B **62**, 1660 (2000).

[16] R. Ahuja, L. Fast, O. Eriksson, J. M. Wills and B. Johansson, *Elastic and high pressure properties of ZnO*, J. Appl. Phys. **83**, 8065 (1998).

[17] J. Serrano, A. H. Romero, F. J. Manjón, R. Lauck, M. Cardona and A. Rubio, *Pressure dependence of the lattice dynamics of ZnO: An ab initio approach*, Phys. Rev. B **69**, 094306 (2004).

[18] A. F. Kohan, G. Ceder, D. Morgan and C. G. Van de Walle, *First-principles study of native point defects in ZnO*, Phys. Rev. B **61**, 15019 (2000).

[19] S. B. Zhang, S. H. Wei and A. Zunger, *Intrinsic n-type versus p-type doping asymmetry and the defect physics of ZnO*, Phys. Rev. B **63**, 075205 (2001).

[20] F. Oba, S. R. Nishitani, S. Isotani, H. Adachi and I. Tanaka, *Energetics of native defects in ZnO*, J. Appl. Phys. **90**, 824 (2001).

[21] E.-C. Lee, Y.-S. Kim, Y.-G. Jin and K. J. Chang, *Compensation mechanism for N acceptors in ZnO*, Phys. Rev. B **64**, 085120 (2001).

[22] S. Lany and A. Zunger, *Anion vacancies as a source of persistent photoconductivity in II-VI and chalcopyrite semiconductors*, Phys. Rev. B **72**, 035215 (2005).

[23] A. Janotti and C. G. Van de Walle, *Oxygen vacancies in ZnO*, Appl. Phys. Lett. **87**, 122102 (2005).

[24] R. O. Jones and O. Gunnarsson, *The density functional formalism, its applications and prospects*, Rev. Mod. Phys. **61**, 689 (1989).

[25] J. P. Perdew, in *Electronic structure of solids*, edited by P. Ziesche and H. Eschrig (Akademie Verlag, Berlin, 1991), Vol. 11.

[26] V. I. Anisimov, J. Zaanen and O. K. Andersen, *Band theory and Mott insulators: Hubbard U instead of Stoner I*, Phys. Rev. B **44**, 943 (1991).

[27] K. Eda, A. Iga and M. Matsuoka, *Degradation mechanism of non-Ohmic zinc oxide ceramics*, J. Appl. Phys. **51**, 2678 (1980).

[28] T. K. Gupta, W. G. Carlson and P. L. Hower, *Current instability phenomena in ZnO varistors under a continuous ac stress*, J. Appl. Phys. **52**, 4104 (1981).

[29] T. K. Gupta and W. Carlson, *A grain-boundary defect model for instability of a ZnO varistor*, J. Mater. Sci. **20**, 3487 (1985).

[30] M. Ramanachalam, A. Rohatgi, J. Schaffer and T. K. Gupta, *Characterization of ZnO varistor degradation using lifetime positron-annihilation spectroscopy*, J. Appl. Phys. **69**, 8380 (1991).

[31] C. Coskun, D. C. Look, G. C. Farlow and J. R. Sizelove, *Radiation hardness of ZnO at low temperatures*, Semicond. Sci. Technol. **19**, 752 (2004).

[32] G. C. Abell, *Empirical chemical pseudopotential theory of molecular and metallic bonding*, Phys. Rev. B **31**, 6184 (1985).

[33] J. Tersoff, *New empirical approach for the structure and energy of covalent systems*, Phys. Rev. B **37**, 6991 (1988).

[34] A. I. Boldyrev and J. Simons, *Ab initio study of the bonding of zinc atoms to first- and second-row main group atoms*, Mol. Phys. **92**, 365 (1997).

[35] C. W. Bauschlicher, Jr. and H. Partridge, *A comparison of ZnO and ZnO^-*, J. Chem. Phys. **109**, 8430 (1998).

[36] D. M. Ceperley and B. J. Alder, *Ground State of the Electron Gas by a Stochastic Method*, Phys. Rev. Lett. **45**, 566 (1980).

[37] J. C. Grossman and L. Mitáš, *Family of low-energy elongated Si_n ($n \leq 50$) clusters*, Phys. Rev. B **52**, 16735 (1995).

[38] L. Mitáš, J. C. Grossman, I. Stich and J. Tobik, *Silicon clusters of intermediate size: energetics, dynamics, and thermal effects*, Phys. Rev. Lett. **84**, 1479 (2000).

[39] W.-K. Leung, R. J. Needs, G. Rajagopal, S. Itoh and S. Ihara, *Calculations of Silicon Self-Interstitial Defects*, Phys. Rev. Lett. **83**, 2351 (1999).

[40] R. Q. Hood, P. R. C. Kent, R. J. Needs and P. R. Briddon, *Quantum Monte Carlo Study of the Optical and Diffusive Properties of the Vacancy Defect in Diamond*, Phys. Rev. Lett. **91**, 076403 (2003).

[41] R. G. Parr and W. Yang, *Density-Functional Theory of Atoms and Molecules* (Oxford University Press, New York, 1989).

[42] C. M. Goringe, D. R. Bowler and E. Hernández, *Tight-binding modelling of materials*, Rep. Prog. Phys. **60**, 1447 (1997).

[43] J. Jacobsen, B. H. Cooper and J. P. Sethna, *Simulations of energetic beam deposition: from picoseconds to seconds*, Phys. Rev. B **58**, 15847 (1998).

[44] M. R. Sørensen and A. F. Voter, *Temperature-accelerated dynamics for simulation of infrequent events*, J. Chem. Phys. **112**, 9599 (2000).

[45] A. F. Voter, F. Montalenti and T. C. Germann, *Extending the Time Scale in Atomistic Simulation of Materials*, Annu. Rev. Mat. Sci. **32**, 321 (2002).

[46] E. B. Tadmor, M. Ortiz and R. Phillips, *Quasicontinuum analysis of defects in solids*, Phil. Mag. A **73**, 1529 (1996).

[47] E. B. Tadmor, R. Phillips and M. Ortiz, *Mixed Atomistic and Continuum Models of Deformation in Solids*, Langmuir **12**, 4529 (1996).

[48] J. Knap and M. Ortiz, *An analysis of the quasicontinuum method*, J. Mech. Phys. Solids **49**, 1899 (2001).

[49] G. Csanyi, T. Albaret, M. C. Payne and A. De Vita, *"Learn on the fly": A Hybrid Classical and Quantum Mechanical Molecular Dynamics Simulation*, Phys. Rev. Lett. **93**, 175503 (2004).

[50] P. Hohenberg and W. Kohn, *Inhomogeneous Electron Gas*, Phys. Rev. **136**, B864 (1964).

[51] W. Kohn and L. J. Sham, *Self-Consistent Equations Including Exchange and Correlation Effects*, Phys. Rev. **140**, A1133 (1965).

[52] C. Lee, W. Yang and R. G. Parr, *Development of the Colle-Salvetti correlation-energy formula into a functional of the electron density*, Phys. Rev. B **37**, 785 (1988).

[53] A. D. Becke, *Density-functional thermochemistry. III. The role of exact exchange*, J. Chem. Phys. **98**, 5648 (1993).

[54] S. L. Dudarev, G. A. Botton, S. Y. Savrasov, C. J. Humphreys and A. P. Sutton, *Electron-energy-loss spectra and the structural stability of nickel oxide: An LSDA+U study*, Phys. Rev. B **57**, 1505 (1998).

[55] I. V. Solovyev, P. H. Dederichs and V. I. Anisimov, *Corrected atomic limit in the local-density approximation and the electronic structure of d impurities in Rb*, Phys. Rev. B **50**, 16861 (1994).

[56] A. I. Liechtenstein, V. I. Anisimov and J. Zaanen, *Density-functional theory and strong interactions: Orbital ordering in Mott-Hubbard insulators*, Phys. Rev. B **52**, R5467 (1995).

[57] M. C. Payne, M. P. Teter, D. C. Allan, T. A. Arias and J. D. Joannopoulos, *Iterative minimization techniques for ab initio total-energy calculations: molecular dynamics and conjugate gradients*, Rev. Mod. Phys. **64**, 1045 (1992).

[58] N. W. Ashcroft and N. D. Mermin, *Solid State Physics* (Saunders College, Fort Worth, 1976).

[59] H. J. Monkhorst and J. D. Pack, *Special points for Brillouin-zone integrations*, Phys. Rev. B **13**, 5188 (1976).

[60] N. Troullier and J. L. Martins, *Efficient pseudopotentials for plane-wave calculations*, Phys. Rev. B **43**, 1993 (1991).

[61] D. Vanderbilt, *Soft self-consistent pseudopotentials in a generalized eigenvalue formalism*, Phys. Rev. B **41**, 7892 (1990).

[62] P. E. Blöchl, *Projector augmented-wave method*, Phys. Rev. B **50**, 17953 (1994).

[63] C. G. Van de Walle, *Defect analysis and engineering in ZnO*, Physica B **308–310**, 899 (2001).

[64] S. B. Zhang, S.-H. Wei and A. Zunger, *A phenomenological model for systemization and prediction of doping limits in II-VI and I-III-VI2 compounds*, J. Appl. Phys. **83**, 3192 (1998).

[65] H. Moormann, D. Kohl and G. Heiland, *Work function and band bending on clean cleaved zinc oxide surfaces*, Surf. Sci. **80**, 261 (1979).

[66] S. Trasatti, *The "absolute" electrode potential: The end of the story*, Electrochimica Acta **35**, 269 (1990).

[67] S. Limpijumnong, S. B. Zhang, S.-H. Wei and C. H. Park, *Doping by Large-Size-Mismatched Impurities: The Microscopic Origin of Arsenic- or Antimony-Doped p-Type Zinc Oxide*, Phys. Rev. Lett. **92**, 155504 (2004).

[68] S. Goedecker, M. Teter and J. Hutter, *Separable dual-space Gaussian pseudopotentials*, Phys. Rev. B **54**, 1703 (1996).

[69] X. Gonze *et al.*, *First-principles computation of material properties: the ABINIT software project*, Comp. Mater. Sci. **25**, 478 (2002).

[70] The ABINIT code is a common project of the Université Catholique de Louvain, Corning Incorporated, and other contributors (URL http://www.abinit.org).

[71] J. Albertsson, S. C. Abrahams and A. Kvick, *Atomic displacement, anharmonic thermal vibration, expansivity and pyroelectric coefficient thermal dependences in ZnO*, Acta Cryst. B **45**, 34 (1989).

[72] *Handbook of Chemistry and Physics*, 85th Ed., edited by D. R. Lide (CRC Press, Boca Raton, 2004).

[73] A. Every and A. McCurdy, in *Landolt-Börnstein: numerical data and functional relationships in science and technology, New Series*, edited by H. Ullmaier (Springer, Heidelberg, 1992), Vol. III/29A.

[74] C. Kittel, *Introduction to Solid State Physics*, 8th Ed. (Wiley, New York, 2004).

[75] Huber K. P. and G. Herzberg, *Constants of Diatomic Molecules* (Van Nostrand, New York, 1979).

[76] G.-X. Qian, R. M. Martin and D. J. Chadi, *First-principles study of the atomic reconstructions and energies of Ga- and As-stabilized GaAs(100) surfaces*, Phys. Rev. B **38**, 7649 (1988).

[77] S. B. Zhang and J. E. Northrup, *Chemical potential dependence of defect formation energies in GaAs: Application to Ga self-diffusion*, Phys. Rev. Lett. **67**, 2339 (1991).

[78] E. Rauls and T. Frauenheim, *Entropy of point defects calculated within periodic boundary conditions*, Phys. Rev. B **69**, 155213 (2004).

[79] R. F. W. Bader, *Atoms in Molecules – A Quantum Theory* (Oxford University Press, Oxford, 1990).

[80] S. B. Zhang, S.-H. Wei and A. Zunger, *Microscopic Origin of the Phenomenological Equilibrium "Doping Limit Rule" in n-Type III-V Semiconductors*, Phys. Rev. Lett. **84**, 1232 (2000).

[81] L. Colombo, *Tight-binding theory of native point defects in silicon*, Annu. Rev. Mat. Sci. **32**, 271 (2002).

[82] S. Limpijumnong and C. G. Van de Walle, *Diffusivity of native defects in GaN*, Phys. Rev. B **69**, 035207 (2004).

[83] Y. Yan, S. B. Zhang, S. J. Pennycook and S. T. Pantelides, *A Theoretical Study of p-Type Doping of ZnO: Problems and Solutions*, Mat. Res. Soc. Symp. Proc. **666**, F2.6 (2001).

[84] Y. Yan, S. B. Zhang and S. T. Pantelides, *Control of Doping by Impurity Chemical Potentials: Predictions for p-Type ZnO*, Phys. Rev. Lett. **86**, 5723 (2001).

[85] B. Arnaud and M. Alouani, *All-electron projector-augmented-wave GW approximation: Application to the electronic properties of semiconductors*, Phys. Rev. B **62**, 4464 (2000).

[86] M. S. Hybertsen and S. G. Louie, *First-Principles Theory of Quasiparticles: Calculation of Band Gaps in Semiconductors and Insulators*, Phys. Rev. Lett. **55**, 1418 (1985).

[87] Y.-J. Zhao, C. Persson, S. Lany and A. Zunger, *Why can $CuInSe_2$ be readily equilibrium-doped n-type but the wider-gap $CuGaSe_2$ cannot?*, Appl. Phys. Lett. **85**, 5860 (2004).

[88] M. J. Puska, S. Pöykkö, M. Pesola and R. M. Nieminen, *Convergence of supercell calculations for point defects in semiconductors: Vacancy in silicon*, Phys. Rev. B **58**, 1318 (1998).

[89] J. Lento, J.-L. Mozos and R. M. Nieminen, *Charged point defects in semiconductors and the supercell approximation*, J. Phys.: Condens. Matter **14**, 2637 (2002).

[90] R. Blachnik, J. Chu, R. R. Galazka, J. Geurts, J. Gutowski, B. Hönerlage, D. Hofmann, J. Kossut, R. Lévy, P. Michler, U. Neukirch, T. Story, D. Strauch and A. Waag, in *Landolt-Börnstein: numerical data and functional relationships in science and technology, New Series*, edited by U. Rössler (Springer, Heidelberg, 1999), Vol. III/41B.

[91] W. Ranke, *Separation of partial s-densities and p-densities of valence states of ZnO from UPS-measurements*, Sol. State. Comm. **19**, 685 (1976).

[92] M. Usuda, N. Hamada, T. Kotani and M. van Schilfgaarde, *All-electron GW calculation based on the LAPW method: Application to wurtzite ZnO*, Phys. Rev. B **66**, 125101 (2002).

[93] S. A. Leontiev, S. V. Koshtcheev, V. G. Devyatov, A. E. Cherkashin and E. P. Mikheeva, *Detailed XPS and UPS studies of the band structure of zinc oxide*, J. Struct. Chem. **38**, 725 (1997).

[94] G. Zwicker and K. Jacobi, *Experimental band structure of ZnO*, Solid State Comm. **54**, 701 (1985).

[95] R. T. Girard, O. Tjernberg, G. Chiaia, S. Söderholm, U. O. Karlsson, C. Wigren, H. Nylén and I. Lindau, *Electronic structure of ZnO(0001) studied by angle-resolved photoelectron spectroscopy*, Surf. Sci. **373**, 409 (1997).

[96] *General Discussion*, Faraday Discuss. **124**, 275 (2003).

[97] P. Schröer, P. Krüger and J. Pollmann, *First-principles calculation of the electronic structure of the wurtzite semiconductors ZnO and ZnS*, Phys. Rev. B **47**, 6971 (1993).

[98] D. Vogel, P. Krüger and J. Pollmann, *Self-interaction and relaxation-corrected pseudopotentials for II-VI semiconductors*, Phys. Rev. B **54**, 5495 (1996).

[99] S. Massidda, R. Resta, M. Posternak and A. Baldereschi, *Polarization and dynamical charge of ZnO within different one-particle schemes*, Phys. Rev. B **52**, R16977 (1995).

[100] J. P. Perdew and A. Zunger, *Self-interaction correction to density-functional approximations for many-electron systems*, Phys. Rev. B **23**, 5048 (1981).

[101] M. S. Park and B. I. Min, *Ferromagnetism in ZnO codoped with transition metals: $Zn_{1-x}(FeCo)_xO$ and $Zn_{1-x}(FeCu)_xO$*, Phys. Rev. B **68**, 224436 (2003).

[102] C. L. Dong, C. Persson, L. Vayssieres, A. Augustsson, T. Schmitt, M. Mattesini, R. Ahuja, C. L. Chang and J.-H. Guo, *Electronic structure of nanostructured ZnO from X-ray absorption and emission spectroscopy and the local density approximation*, Phys. Rev. B **70**, 195325 (2004).

[103] G. Kresse and J. Furthmüller, *Efficient iterative schemes for ab initio total-energy calculations using a plane-wave basis set*, Phys. Rev. B **54**, 11169 (1996).

[104] G. Kresse and D. Joubert, *From ultrasoft pseudopotentials to the projector augmented-wave method*, Phys. Rev. B **59**, 1758 (1999).

[105] C. P. Flynn, *Point Defects and Diffusion* (Oxford University Press, Oxford, 1972).

[106] P. Ehrhart, P. Jung, H. Schultz and H. Ullmaier, in *Landolt-Börnstein: Numerical Data and Functional Relationships in Science and Technology, New Series*, edited by H. Ullmaier (Springer, Heidelberg, 1991), Vol. III/25.

[107] S. A. Centoni, B. Sadigh, G. H. Gilmer, T. J. Lenosky, T. Diaz de la Rubia and C. B. Musgrave, *First-principles calculation of intrinsic defect formation volumes in silicon*, Phys. Rev. B **72**, 195206 (2005).

[108] F. Birch, *Finite strain isotherm and velocities for single-crystal and polycrystalline NaCl at high pressures and 300 degrees K*, J. Geophys. Res. **83**, 1257 (1978).

[109] G. Makov and M. C. Payne, *Periodic boundary conditions in ab initio calculations*, Phys. Rev. B **51**, 4014 (1995).

[110] D. C. Look, J. W. Hemsky and J. R. Sizelove, *Residual Native Shallow Donor in ZnO*, Phys. Rev. Lett. **82**, 2552 (1999).

[111] F. Tuomisto, V. Ranki, K. Saarinen and D. C. Look, *Evidence of the Zn Vacancy Acting as the Dominant Acceptor in n-Type ZnO*, Phys. Rev. Lett. **91**, 205502 (2003).

[112] C. Persson, Y.-J. Zhao, S. Lany and A. Zunger, *n-type doping of CuInSe2 and CuGaSe2*, Phys. Rev. B **72**, 035211 (2005).

[113] M. Liu, A. H. Kitai and P. Mascher, *Point-defects and luminescence-centers in zinc-oxide and zinc-oxide doped with manganese*, J. Lumin. **54**, 35 (1992).

[114] L. Bixia, F. Zhuxi and J. Yunbo, *Green luminescent center in undoped zinc oxide films deposited on silicon substrates.*, Appl. Phys. Lett. **79**, 943 (2001).

[115] A. R. Allnatt and A. B. Lidiard, *Atomic Transport in Solids* (Cambridge University Press, Cambridge, 2003).

[116] W. J. Moore and E. L. Williams, *Diffusion of zinc and oxygen in zinc oxide*, Discuss. Faraday Soc. **28**, 86 (1959).

[117] J. W. Hoffman and I. Lauder, *Diffusion of oxygen in single crystal zinc oxide*, Trans. Faraday Soc. **66**, 2346 (1970).

[118] R. Robin, A. R. Cooper and A. H. Heuer, *Application of a nondestructive single-spectrum proton activation technique to study oxygen diffusion in zinc oxide*, J. Appl. Phys. **44**, 3770 (1973).

[119] G. W. Tomlins, J. L. Routbort and T. O. Mason, *Oxygen diffusion in single-crystal zinc oxide*, J. Amer. Ceram. Soc. **81**, 869 (1998).

[120] H. Haneda, I. Sakaguchi, A. Watanabe, T. Ishigaki and J. Tanaka, *Oxygen Diffusion in Single- and Poly-Crystalline Zinc Oxides*, J. Electroceramics **4**, 41 (1999).

[121] A. C. S. Sabioni, M. J. F. Ramos and W. B. Ferraz, *Oxygen diffusion in pure and doped ZnO*, Mat. Res. **6**, 173 (2003).

[122] M. G. Wardle, J. P. Goss and P. R. Briddon, *Theory of Li in ZnO: A limitation for Li-based p-type doping*, Phys. Rev. B **71**, 155205 (2005).

[123] G. M. Dalpian and S.-H. Wei, *Photoinduced cation interstitial diffusion in II-VI semiconductors*, Phys. Rev. B **72**, 075208 (2005).

[124] G. Henkelman, G. Jóhannesson and H. Jónsson, in *Methods for finding saddlepoints and minimum energy paths* in *Progress on theoretical chemistry and physics,* p. 269, edited by S. D. Schwartz (Kluwer Academic, Dordrecht, 2000).

[125] G. Henkelman, B. P. Uberuaga and H. Jónsson, *A climbing image nudged elastic band method for finding saddle points and minimum energy paths*, J. Chem. Phys. **113**, 9901 (2000).

[126] G. H. Vineyard, *Frequency factors and isotope effects in solid state rate processes*, J. Phys. Chem. Solids **3**, 121 (1957).

[127] R. Olsen, G. J. Kroes, G. Henkelman, A. Arnaldsson and H. Jonsson, *Comparison of methods for finding saddle points without knowledge of the final states.*, J. Chem. Phys. **121**, 9776 (2004).

[128] G. Henkelman and H. Jónsson, *A method for finding saddle points on high dimensional potential surfaces using only first derivatives*, J. Chem. Phys. **111**, 7010 (1999).

[129] The implementations of the climbing image nudged elastic band and the dimer method for VASP were obtained from `http://theory.cm.utexas.edu/henkelman` .

[130] Y. V. Gorelkinskii and G. D. Watkins, *Defects produced in ZnO by 2.5-MeV electron irradiation at 4.2 K: study by optical detection of electron paramagnetic resonance*, Phys. Rev. B **69**, 115212 (2004).

[131] K. Lorenz, E. Alves, E. Wendler, O. Bilani, W. Wesch and M. Hayes, *Damage formation and annealing at low temperatures in ion implanted ZnO*, Appl. Phys. Lett. **87**, 191904 (2005).

[132] F. Tuomisto, K. Saarinen, D. C. Look and G. C. Farlow, *Introduction and recovery of point defects in electron-irradiated ZnO*, Phys. Rev. B **72**, 085206 (2005).

[133] A. C. S. Sabioni, *About the oxygen diffusion mechanism in ZnO*, Solid State Ionics **170**, 145 (2004).

[134] D. G. Thomas, *Interstitial zinc in zinc oxide*, J. Phys. Chem. Solids **3**, 229 (1957).

[135] D. J. Binks and R. W. Grimes, *Incorporation of Monovalent ions in ZnO and their influence on varistor degradation*, J. Am. Ceram. Soc. **76**, 2370 (1993).

[136] G. W. Tomlins, J. L. Routbort and T. O. Mason, *Zinc self-diffusion, electrical properties, and defect structure of undoped, single crystal zinc oxide*, J. Appl. Phys. **87**, 117 (2000).

[137] R. Lindner, *Die Diffusion von radioaktivem Zink in Zink-Eisen-Spinell und Zinkoxyd*, Acta Chem. Scand. **6**, 457 (1952).

[138] E. A. Secco and W. J. Moore, *Diffusion of zinc in crystalline zinc oxide*, J. Chem. Phys. **23**, 1170 (1955).

[139] E. A. Secco and W. J. Moore, *Diffusion and exchange of zinc in crystalline zinc oxide*, J. Chem. Phys. **26**, 942 (1957).

[140] B. J. Wuensch and H. L. Tuller, *Lattice diffusion, grain-boundary diffusion and defect structure of ZnO*, J. Phys. Chem. Solids **55**, 975 (1994).

[141] M. A. d. N. Nogueira, W. B. Ferraz and A. C. S. Sabioni, *Diffusion of the* $^{6}5Zn$ *radiotracer in ZnO polycrystalline ceramics*, Mater. Res. **6**, 167 (2003).

[142] M. S. Daw and M. I. Baskes, *Embedded-atom method: Derivation and application to impurities, surfaces and other defects in metals*, Phys. Rev. B **29**, 6443 (1984).

[143] F. H. Stillinger and T. A. Weber, *Computer simulation of local order in condensed phases of silicon*, Phys. Rev. B **31**, 5262 (1985).

[144] M. J. Stott and E. Zaremba, *Quasiatoms: An approach to atoms in nonuniform electronic systems*, Phys. Rev. B **22**, 1564 (1980).

[145] M. J. Puska, R. M. Nieminen and M. Manninen, *Atoms embedded in an electron gas: Immersion energies*, Phys. Rev. B **24**, 3037 (1981).

[146] J. K. Norskov, *Covalent effects in the effective-medium theory of chemical binding: Hydrogen heats of solution in the 3d metals*, Phys. Rev. B **26**, 2875 (1982).

[147] A. E. Carlsson, *Solid State Physics: Advances in Research and Applications*, edited by H. Ehrenreich and D. Turnbull (Academic, New York, 1990), Vol. 43.

[148] A. P. Horsfield, A. M. Bratkovsky, M. Fearn, D. G. Pettifor and M. Aoki, *Bond-order potentials: Theory and implementation*, Phys. Rev. B **53**, 12694 (1996).

[149] D. W. Brenner, *Relationship between the Embedded-Atom Method and Tersoff Potentials*, Phys. Rev. Lett. **63**, 1022 (1989).

[150] K. Albe, K. Nordlund, J. Nord and A. Kuronen, *Modeling of compound semiconductors: Analytical bond-order potential for Ga, As, and GaAs*, Phys. Rev. B **66**, 035205 (2002).

[151] M. I. Baskes, *Modified embedded-atom potentials for cubic materials and impurities*, Phys. Rev. B **46**, 2727 (1992).

[152] D. W. Brenner, *Empirical potential for hydrocarbons for use in simulating the chemical vapor deposition of diamond films*, Phys. Rev. B **42**, 9458 (1990).

[153] D. W. Brenner, O. A. Shenderova, J. A. Harrison, S. J. Stuart, B. Ni and S. B. Sinnott, *A second-generation reactive empirical bond order (REBO) potential energy expression for hydrocarbons*, J. Phys.: Condens. Matter **14**, 783 (2002).

[154] K. A. Albe, K. Nordlund and R. S. Averback, *Modeling the metal-semiconductor interaction: Analytical bond-order potential for platinum-carbon*, Phys. Rev. B **65**, 195124 (2002).

[155] N. Juslin, P. Erhart, P. Träskelin, J. Nord, K. Henriksson, E. Salonen, K. Nordlund and K. Albe, *Analytical interatomic potential for modeling nonequilibrium processes in the W–C–H system*, J. Appl. Phys. **98**, 123520 (2005).

[156] D. Pettifor and I. Oleinik, *Analytic bond-order potentials beyond Tersoff-Brenner. I. Theory*, Phys. Rev. B **59**, 8487 (1999).

[157] D. G. Pettifor, M. W. Finnis, D. Nguyen-Manh, D. A. Murdick, X. W. Zhou and H. N. G. Wadley, *Analytic bond-order potentials for multicomponent systems*, Mater. Sci. Eng. A **365**, 2 (2004).

[158] C. R. A. Catlow, *Point Defect and Electronic Properties of Uranium Dioxide*, Proc. Roy. Soc. A **353**, 533 (1977).

[159] G. V. Lewis and C. R. A. Catlow, *Potential models for ionic oxides*, J. Phys. C: Solid State Phys. **18**, 1149 (1985).

[160] B. G. Dick, Jr. and A. W. Overhauser, *Theory of the Dielectric Constants of Alkali Halide Crystals*, Phys. Rev. **112**, 90 (1958).

[161] F. Shimojo, I. Ebbsjö, R. K. Kalia, A. Nakano, J. P. Rino and P. Vashishta, *Molecular Dynamics Simulation of Structural Transformation in Silicon Carbide under Pressure*, Phys. Rev. Lett. **84**, 3338 (2000).

[162] A. Chatterjee, R. Kalia, A. Nakano, A. Omeltchenko, K. Tsuruta, P. Vashishta, C.-K. Loong, M. Winterer and S. Klein, *Sintering, structure, and mechanical properties of nanophase SiC: A molecular-dynamics and neutron scattering study*, Appl. Phys. Lett. **77**, 1132 (2000).

[163] J. P. Rino, A. Chatterjee, I. Ebbsjö, R. K. Kalia, A. Nakano, F. Ebbsjö and P. Vashishta, *Pressure-induced structural transformation in GaAs: A molecular-dynamics study*, Phys. Rev. B **65**, 195206 (2002).

[164] M. Kubo, Y. Oumi, H. Takaba, A. Chatterjee, A. Miyamoto, M. Kawasaki, M. Yoshimoto and H. Koinuma, *Homoepitaxial growth mechanism of ZnO(0001): Molecular-dynamics simulations*, Phys. Rev. B **61**, 16187 (2000).

[165] F. H. Streitz and J. W. Mintmire, *Electrostatic potentials for metal-oxide surfaces and interfaces*, Phys. Rev. B **50**, 11996 (1994).

[166] S. Ogata, H. Iyetomi, K. Tsuruta, F. Shimojo, R. K. Kalia, A. Nakano and P. Vashishta, *Variable-charge interatomic potentials for molecular-dynamics simulations of TiO_2*, J. Appl. Phys. **86**, 3036 (1999).

[167] A. C. T. van Duin, S. Dasgupta, F. Lorant and W. A. Goddard, III, *ReaxFF: a reactive force field for hydrocarbons*, J. Phys. Chem. A **105**, 9396 (2001).

[168] Q. Zhang, T. Çagin, A. van Duin, W. A. Goddard, III, Y. Qi and L. G. Hector, Jr., *Adhesion and nonwetting-wetting transition in the Al/alpha-Al_2O_3 interface*, Phys. Rev. B **69**, 045423 (2004).

[169] J. Tersoff, *Empirical interatomic potential for silicon with improved elastic properties*, Phys. Rev. B **38**, 9902 (1988).

[170] J. Tersoff, *Empirical Interatomic Potential for Carbon, with Applications to Amorphous Carbon*, Phys. Rev. Lett. **61**, 2879 (1988).

[171] J. Tersoff, *Modeling solid-state chemistry: Interatomic potentials for multicomponent systems*, Phys. Rev. B **39**, 5566 (1989).

[172] M. V. R. Murty and H. A. Atwater, *Empirical interatomic potential for Si–H interactions*, Phys. Rev. B **51**, 4889 (1995).

[173] K. Beardmore and R. Smith, *Empirical potentials for C–Si–H systems with application to C_{60} interactions with Si surfaces*, Phil. Mag. A **74**, 1439 (1996).

[174] A. J. Dyson and P. V. Smith, *Extension of the Brenner empirical interatomic potential to C–Si–H systems*, Surf. Sci. **355**, 140 (1996).

[175] A. J. Dyson and P. V. Smith, *Improved empirical interatomic potential for C–Si–H systems*, Mol. Phys. **96**, 1491 (1999).

[176] F. Gao and W. J. Weber, *Empirical potential approach for defect properties in 3C-SiC*, Nucl. Instr. Meth. Phys. Res. B **191**, 504 (2002).

[177] P. Erhart and K. Albe, *Analytical Potential for Atomistic Simulations of Silicon and Silicon Carbide*, Phys. Rev. B **71**, 035211 (2005).

[178] K. Albe and R. S. Averback, *Modeling of metal-carbides: Analytical bond-order potential for nickel and nickel-carbide*, to be published.

[179] J. Nord, K. Albe, P. Erhart and K. Nordlund, *Modelling of compound semiconductors: Analytical bond-order potential for gallium, nitrogen and gallium nitride*, J. Phys.: Condens. Matter **15**, 5649 (2003).

[180] J. Gale, *GULP: A computer program for the symmetry-adapted simulation of solids*, JCS Faraday Trans. **93**, 629 (1997).

[181] J. D. Gale and A. L. Rohl, *The General Utility Lattice Program (GULP)*, Mol. Simul. **29**, 291 (2003).

[182] H. Balamane, T. Halicioglu and W. A. Tiller, *Comparative study of silicon empirical interatomic potentials*, Phys. Rev. B **46**, 2250 (1992).

[183] D. W. Brenner, *The Art and Science of an Analytical Potential*, Phys. Stat. Sol. B **217**, 23 (2000).

[184] T. J. Lenosky, B. Sadigh, E. Alonso, V. V. Bulatov, T. Diaz de la Rubia, J. Kim, A. F. Voter and J. D. Kress, *Highly optimized empirical potential model of silicon*, Modelling Simul. Mater. Sci. Eng. **8**, 825 (2000).

[185] Y. Mishin, D. Farkas, M. J. Mehl and D. A. Papaconstantopoulos, *Interatomic potentials for monoatomic metals from experimental data and ab initio calculations*, Phys. Rev. B **59**, 3393 (1999).

[186] B. J. Thijsse, *Silicon potentials under (ion) attack: towards a new MEAM model*, Nucl. Instr. Meth. Phys. Res. B **228**, 198 (2005).

[187] F. Ercolessi and J. B. Adams, *Interatomic potentials from first-principles calculations: the force-matching method.*, Europhys. Lett. **26**, 583 (1994).

[188] Y. Saito, N. Sasaki, H. Moriya, A. Kagatsume and S. Noro, *Parameter optimization of Tersoff interatomic potentials using a genetic algorithm*, JSME Int. J. Ser. A **44**, 207 (2001).

[189] K. Nordlund and A. Kuronen, *Non-equilibrium properties of GaAs interatomic potentials*, Nucl. Instr. Meth. Phys. Res. B **159**, 183 (1999).

[190] W. H. Press, S. A. Teukolsky, W. T. Vetterling and B. P. Flannery, in *Numerical Recipes in Fortran 77: The Art of Scientific Computing*, 2nd Ed. (Cambridge University Press, New York, 1995), Chap. 11.

[191] P. Erhart, PONTIFIX/PINGUIN*: User Manual*.

[192] K. Albe, J. Nord and K. Nordlund, *Analytical bond-order potential for gallium nitride with environment dependent valence charges*, to be published.

[193] R. M. Martin, *Relation between Elastic Tensors of Wurtzite and Zinc-Blende Structure Materials*, Phys. Rev. B **6**, 4546 (1972), *ibid.* **20**, 818 (1979), erratum.

[194] C. A. Fancher, H. L. de Clercq, O. C. Thomas, D. W. Robinson and K. H. Bowen, *Zinc oxide and its anion: A negative ion photoelectron spectroscopic study*, J. Chem. Phys. **109**, 8426 (1998).

[195] E. H. Kisi and M. M. Elcombe, *u parameters for the wurtzite structure of ZnS and ZnO using powder neutron diffraction*, Acta Cryst. C **45**, 1867 (1989).

[196] T. B. Bateman, *Elastic moduli of single-crystal zinc oxide*, J. Appl. Phys. **33**, 3309 (1962).

[197] I. B. Kobiakov, *Elastic, piezoelectric and dielectric-properties of ZnO and CdS single-crystals in ad wide-range of temperatures*, Solid State Comm. **35**, 305 (1980).

[198] J. M. Recio, R. Pandey and V. Luaña, *Quantum-mechanical modeling of the high-pressure state equations of ZnO and ZnS*, Phys. Rev. B **47**, 3401 (1993).

[199] S. Desgreniers, *High-density phases of ZnO: Structural and compressive parameters*, Phys. Rev. B **58**, 14102 (1998).

[200] H. Karzel, W. Potzel, M. Köfferlein, W. Schiessl, M. Steiner, U. Hiller, G. M. Kalvius, D. W. Mitchell, T. P. Das, P. Blaha, K. Schwarz and M. P. Pasternak, *Lattice dynamics and hyperfine interactions in ZnO and ZnSe at high external pressures*, Phys. Rev. B **53**, 11425 (1996).

[201] L. Kleinman, *Deformation Potentials in Silicon. I. Uniaxial Strain*, Phys. Rev. **128**, 2614 (1962).

[202] F. Cleri and V. Rosato, *Tight-binding potentials for transition metals and alloys*, Phys. Rev. B **48**, 22 (1993).

[203] M. I. Baskes and R. A. Johnson, *Modified embedded atom potentials for HCP metals*, Modelling Simul. Mater. Sci. Eng. **2**, 147 (1994).

[204] M. A. Czajkowski, R. Bobkowski and L. Krause, $O_u^+(^3\Pi_u) \leftarrow XO_g^+(^1\Sigma_g^+)$ *transitions in* Zn_2 *excited in crossed molecular and laser beams*, Phys. Rev. A **41**, 277 (1990).

[205] B. Eisenmann and H. Schäfer, in *Landolt-Börnstein: numerical data and functional relationships in science and technology, New Series*, edited by H. Ullmaier (Springer, Heidelberg, 1988), Vol. III/14 A.

[206] H. M. Ledbetter, *The elastic constants of zinc – compilation and a review*, J. Phys. Chem. Ref. Data **6**, 1181 (1977).

[207] D. Singh and D. A. Papaconstantopoulos, *Equilibrium properties of zinc*, Phys. Rev. B **41**, 8885 (1990).

[208] F. Ercolessi, O. Tomagnini, S. Iarlori and E. Tosatti, in *Nanosources and Manipulation of Atoms Under High Fields and Temperatures: Applications*, edited by V. T. Binh (Kluwer, Dordrecht, 1993), S. 185–205.

[209] H. J. C. Berendsen, J. P. M. Postma, W. F. Gunsteren, A. D. Nola and J. R. Haak, *Molecular dynamics with coupling to an external bath*, J. Chem. Phys. **81**, 3684 (1984).

[210] P. J. Hay and T. H. Dunning, Jr., *Geometries and energies of the excited states of* O_3 *from ab initio potential energy surfaces*, J. Chem. Phys. **67**, 2290 (1977).

[211] L. A. Curtiss, K. Raghavachari, G. W. Trucks and J. A. Pople, *Gaussian-2 theory for molecular energies of first- and second-row compounds*, J. Chem. Phys. **94**, 7221 (1991).

[212] J. M. Seminario, *A study of small systems containing H-atoms and O-atoms using nonlocal functionals - comparisons with ab-initio and experiment*, Int. J. Quant. Chem. **52**, 655 (1994), suppl. 28.

[213] P. Politzer and P. Lane, *Kohn-Sham studies of oxygen systems*, Int. J. Quant. Chem. **77**, 336 (2000).

[214] A. F. Jalbout, *DFT/B3-LYP and ab initio analysis of the ozone potential energy surface*, J. Mol. Struct.: THEOCHEM **617**, 5 (2002).

[215] H. U. Jäger and K. Albe, *Molecular-dynamics simulations of steady-state growth of ion-deposited tetrahedral amorphous carbon films.*, J. Appl. Phys. **88**, 1129 (2000).

[216] M. Tang and S. Yip, *Atomistic simulation of thermomechanical properties of β-SiC*, Phys. Rev. B **52**, 15150 (1995).

[217] R. Smith (ed.), *Atomic & ion collisions in solids and at surfaces: theory, simulation and applications* (Cambridge University Prss, Cambridge, UK, 1997).

[218] R. S. Averback and T. Diaz de la Rubia, *Displacement Damage in Irradiated Metals and Semiconductors*, Solid State Physics **51**, 281 (1998).

[219] D. C. Look, G. C. Farlow, P. Reunchan, S. Limpijumnong, S. B. Zhang and K. Nordlund, *Evidence for native-defect donors in n-type ZnO*, Phys. Rev. Lett. **95**, 225502 (2005).

[220] K. Nordlund, J. Wallenius and L. Malerba, accepted for publication in Nucl. Instr. Meth. B .

[221] C. Erginsoy, G. H. Vineyard and A. Englert, *Dynamics of Radiation Damage in a Body-Centered Cubic Lattice*, Phys. Rev. **133**, 595 (1964).

[222] K. Nordlund, M. Ghaly, R. S. Averback, M. Caturla, T. Diaz de la Rubia and J. Tarus, *Defect production in collision cascades in elemental semiconductors and FCC metals*, Phys. Rev. B **57**, 7556 (1998).

[223] J. M. Meese and D. R. Locker, *Oxygen displacement energy in ZnO*, Solid State Comm. **11**, 1547 (1972).

[224] G. Pazionis and H.-J. Schulz, *Radiation damage experiments with ZnO at low temperatures*, Mater. Sci. Forum **10-12**, 839 (1986).

[225] W. E. Vehse, W. A. Sibley, F. J. Keller and Y. Chen, *Radiation damage in ZnO single crystals*, Phys. Rev. **167**, 828 (1968).

[226] Accelrys Inc., *CASTEP Users Guide* (Accelrys Inc., San Diego, 2001).

[227] V. Milman, J. A. White, C. J. Pickard, M. C. Payne, E. V. Akhmatskaya and R. H. Nobes, *Electronic structure, properties, and phase stability of inorganic crystals: A pseudopotential plane-wave study*, Int. J. Quant. Chem. **77**, 895 (2000).

[228] M. J. Frisch and G. W. Trucks, *Gaussian 94, rev. E.2* (Gaussian Inc., Pittsburgh, 1995).

[229] A. Beltrán, J. Andrés, M. Calatayud and J. B. L. Martins, *Theoretical study of ZnO* $(10\bar{1}0)$ *and Cu/ZnO* $(10\bar{1}0)$ *surfaces*, Chem. Phys. Lett. **338**, 224 (2001).

[230] U. Diebold, L. Koplitz and O. Dulub, *Atomic-scale properties of low-index ZnO surfaces*, Appl. Surf. Sci. **237**, 336 (2004).

[231] B. Meyer and D. Marx, *Density-functional study of the structure and stability of ZnO surfaces*, Phys. Rev. B **67**, 035403 (2003).

[232] B. Meyer, *First-principles study of the polar O-terminated ZnO surface in thermodynamic equilibrium with oxygen and hydrogen*, Phys. Rev. B **69**, 045416 (2004).

[233] F. Claeyssens, C. L. Freeman, N. L. Allan, Y. Sun, M. N. R. Ashfold and J. H. Harding, *Growth of ZnO thin films - experiment and theory*, J. Mater. Chem. **15**, 139 (2005).

[234] C. G. Van de Walle, *Hydrogen as a Cause of Doping in Zinc Oxide*, Phys. Rev. Lett. **85**, 1012 (2000).

[235] S. Limpijumnong and S. B. Zhang, *Resolving hydrogen binding sites by pressure - A first-principles prediction for ZnO*, Appl. Phys. Lett. **86**, 151910 (2005).

[236] L. Petit, T. C. Schulthess, A. Svane, Z. Szotek, W. M. Temmerman and A. Janotti, *Electronic structure of transition-metal impurities in p-type ZnO*, Phys. Rev. B **73**, 045107 (2006).

[237] G. V. Lewis and C. R. A. Catlow, *Defect studies of doped and undoped barium titanate using computer simulation techniques*, J. Phys. Chem. Solids **47**, 89 (1986).

[238] A. J. Kulkarni, M. Zhou and F. J. Ke, *Orientation and size dependence of the elastic properties of zinc oxide nanobelts*, Nanotechnology **16**, 2749 (2005).

[239] A. J. Kulkarni and M. Zhou, *Size-dependent thermal conductivity of zinc oxide nanobelts*, Appl. Phys. Lett. **88**, 141921 (2006).

[240] M. P. Allen and D. J. Tildesley, *Computer Simulation of Liquids* (Oxford University Press, Oxford, 1987).

[241] D. C. Wallace, *Thermodynamics of Crystals* (Dover, Mineola, New York, 1998).

[242] S. Goedecker, *Fast radix 2, 3, 4 and 5 kernels for Fast Fourier Transformations on computers with overlapping multiply-add instructions*, SIAM J. on Scientific Computing **18**, 1605 (1997).

[243] X. Gonze, *Towards a potential-based conjugate gradient algorithm for order-N self-consistent total energy calculations*, Phys. Rev. B **54**, 4383 (1996).